Indian Institute of Technology Guwahati
Doctoral Thesis

Augmentation of ray-pencil model to calculate optical trapping force for arbitrary beam profiles and its experimental validation

Karuna Sindhu Malik
Roll No: 156121025

Thesis submitted in partial fulfilment of the requirements for the degree of Doctor of Philosophy of the Indian Institute of Technology Guwahati.

Supervisor: **Prof. Bosanta R. Boruah**

Optical Imaging Lab
Department of Physics
Indian Institute of Technology Guwahati
Guwahati (Assam), India, Pin- 781039

November 2021

... dedicated to my beloved family

Declaration

Karuna Sindhu Malik
Roll No: 156121025
Optical Imaging Lab
Department of Physics
Indian Institute of Technology Guwahati
Guwahati (Assam), India, Pin- 781039
Email: karuna.malik@iitg.ac.in

I hereby declare that the results embodied in this thesis is the results of theory and experiment carried out by me at the Department of Physics, Indian Institute of Technology Guwahati, Guwahati, India, under the supervision of **Prof. Bosanta R. Boruah**. This thesis has not been submitted to any university / institute or elsewhere for the award of any degree, diploma or associateship.

Karuna Sindhu Malik
November 2021


भारतीय प्रौद्योगिकी संस्थान गुवाहाटी
Indian Institute of Technology Guwahati

Certificate

Prof. Bosanta R. Boruah
Department of Physics
Indian Institute of Technology Guwahati
Guwahati (Assam), India, Pin- 781039
Email: brboruah@iitg.ac.in

This is to certify that the work contained in the thesis entitled **‘Augmentation of ray-pencil model to calculate optical trapping force for arbitrary beam profiles and its experimental validation’** by **Karuna Sindhu Malik** (Roll No. 156121025), a student of Department of Physics, Indian Institute of Technology Guwahati, for the award of degree of Doctor of Philosophy, has been carried out under my supervision.

The present thesis or any part thereof has not been submitted elsewhere for award of any other degree, diploma or associateship.

Prof. Bosanta R. Boruah
November 2021

Acknowledgements

I feel immensely happy and grateful to convey my gratitude to all of you who have contributed to this thesis in their unique way. I must say it has been a great learning period of my life, not only in academic way, but also to grow up as a responsible person.

First and foremost, my sincere gratitude goes to my PhD supervisor, Prof. Bosanta Ranjan Boruah for his excellent and inspiring guidance over the span of my PhD life. His punctual way of supervision, constructive criticism and insightful comments have helped me to complete the thesis work. It is needless to say that his constant guidance and advice inspire me to work hard even after several failures during my PhD work.

I would like to convey my sincere gratitude towards my PhD thesis Doctoral Committee members: Prof. Alika Khare, Dr. Kanhaiya Pandey and Dr. Tamarapalli Venkatesh for their valuable comments, suggestions and support during the progress seminars and presentations which helped me to improve my research work.

I extend my sincere gratitude to the present and the past Heads of the Department, Prof. Poulose Poulose, Prof. Subhradip Ghosh, and Prof. Perumal Alagarsamy for their full support in different kinds of facilities of the department. I express my cordial thanks and gratefulness to all the Faculty members of the department for their care and support during my PhD life. I would also like to thank all the staff members of the department for their help and cooperation during official work.

I would like to sincerely acknowledge the financial support by the Ministry of Human Resource and Development (MHRD) of India.

I am grateful to my fellow group-mates Dr.Biswajit Pathak, Dr.Santanu Konwar, Dr.Ranjan Kalita, Dr.SS Goutam Buddha, Nagendra Kumar, Akanshu Chauhan, Nedup Sherpa, Anupam Bharadwaj, Pranjal Choudhury and Shilpa Singh for their encouragement, support, informal discussions and quality time that we had spent together.

I would like to thank the SPIE IITG Student chapter members for involving me in organizing various events at school and colleges of Assam. It was a great time that I spend with all the SPIE members during organization of the various events.

I am very fortunate to have a huge friend circle with whom I spend wonderful times in the IITG campus. I am thankful to all my friends, batchmates, juniors and seniors at IIT Guwahati with whom I shared a comfortable time that helped me to overcome the stressful situations during PhD. I want to thank specially to the entire football group of IITG with whom I spent a fantastic and memorable football life. I am also very glad to express my love to all my badminton friends, seniors and faculty members of IITG. I would also like to thank my school friends, B.Sc friends, M.Sc friends for their love and constant encouragements in ups and downs of my life.

Last but not the least, I pay my whole-hearted respect and gratitude towards my parents M.C. Malik and Santi Malik for their unconditional support and continuous encouragement to take up a career in the field of science. Their love and support always inspired me in pursuing my dream. My wonderful brothers Pritam, Nilanjan and Rishi and sister Camellia, many many thanks to all of you for your love and support. Their unwavering faith and belief in me has motivated me to go forward in the midst of all kinds of situations.

Abstract

Single beam optical trap comprises a tightly focused laser beam that exerts a pico-Newton level force on suspended microscopic particles. Since last couple of decades optical traps have become an important tool in areas such as biological and biomedical sciences. For proper design and efficient working of the optical traps it is important to know the various forces acting on a trapped particle using an appropriate force calculation model. Since majority of the recent applications involve trapping and manipulation of large biological particles hence for such particles force calculation model in the ray optics regime such as the ray-pencil model is more appropriate. However existing form of the ray-pencil model can compute optical forces due to plane wavefronts with cylindrically symmetric beam profiles only. On the other hand there are optical traps that use complex beams such as vortex beams. Moreover, often the light beam used in an optical trap does not have a plane wavefront due to aberrations present. For all such cases the present form of the ray-pencil model is not sufficient. In this thesis we propose an augmentation in the ray-pencil model to be able to compute optical forces due to an arbitrary beam profile. We develop a dynamic holographic optical trap to experimentally measure the various optical forces acting on a spherical bead. We validate the proposed augmented force calculation model by comparing the numerical results with the experimental results. We also compute the optical forces on a trapped bead due to a number of vortex beams using the proposed model. We then use our holographic trap to perform trapping experiments using the vortex beams. We again find that the experimental results agree well with the theoretical predictions.

Table of contents


भारतीय प्रौद्योगिकी संस्थान गुवाहाटी
Indian Institute of Technology Guwahati

List of figures

List of tables

Acronyms and Abbreviation

Greek Symbols

π	$\simeq 3.14\ldots$
i	Unit Imaginary Number ($\sqrt{-1}$)
λ	Wavelength
σ	Beam Waist of Laser
κ	Stiffness Constant
η	Viscosity of Medium
α	Incident Angle
β	Refraction Angle

Acronyms / Abbreviations

BS	Beam Splitter
CGH	Computer Generated Holography
CMOS	Complementary Metal Oxide Semiconductor
DPSS	Diode-Pumped Solid State
DVI	Digital Visual Interface
FPS	Frames Per Second
FWHM	Full Width at Half Maximum

GLMT	Generalized Lorentz-Mie Theory
HOT	Holographic Optical Tweezer
ID	Iris Diaphragm
LC	Liquid Crystal
LCSLM	Liquid Crystal Spatial light modulator
LCoS	Liquid Crystal on Silicon
LMT	Lorentz-Mie Theory
MO	Microscope Objective
NA	Numerical Aperture
NDF	Neutral Density Filter
NLCSLM	Nematic Liquid Crystal Spatial light modulator
OT	Optical tweezers
OD	Optical Density
RMS	Root Mean Square
SLM	Spatial Light Modulator
SWF	Spherical Wavefront
WXGA	Wide Extended Graphics Array

CHAPTER 1

Introduction

1.1 Introduction and thesis overview

Since the development of electromagnetic theory by Maxwell (Maxwell 1873), it has been accepted that light carries not only energy but also momentum [1]. The momentum of light changes when light encounters any particle in its path and due to momentum conservation the particle experiences a force resulting in radiation pressure. The first experimental proof of radiation pressure was performed by Nichols and Hull in 1901 qualitatively and in 1903 quantitatively [2–4]. The magnitude of radiation pressure is not significant for less intense light, but can be substantial for intense light. Therefore, the phenomenon of radiation pressure had not been much useful practically until the invention of laser in 1960. In 1970, A.Ashkin utilized the radiation pressure of laser to demonstrate the acceleration and trapping of micron-sized particle by using two counter-propagating laser beams [5]. A few years later, in 1986, Ashkin made use of laser radiation pressure to demonstrate the single-beam gradient force trap to pull the dielectric particles towards the highest light intensity [6]. Even though it was very difficult to hold and move micron-sized particles against the light propagation direction but Ashkin's single-beam gradient trap opened the door of optical trapping to the scientific community. To define it formally, optical trapping is a non-contact and non-invasive technique to trap small particles (size ranging from tens of nano meters to tens of micro meters) in three dimension. When an expanded and collimated laser beam goes through a high numerical aperture objective lens, the beam gets tightly focused. This tightly focused beam when passes through a small transparent particle of appropriate refractive index, then the particle feels a gradient force towards the focal point and a scattering force in the laser propagation direction. So, if the gradient force dominates over the scattering force, the particle near the focal point of a tightly focused beam gets trapped. Optical traps can be arranged in a more sophisticated manner to not only trap one or more micron-sized particles but also to manipulate the same like a tweezer. Such an arrangement is known as optical tweezers [7, 8]. In this thesis the terms "optical trap" and "optical tweezer" will often be used interchangeably.

The optical force of the order of pico-Newtons as observed in optical tweezers (OT) is of great significance to the microscopic world for various applications. Due to contactless control of the particle in the optical tweezer, it is of great advantage to apply the same in biological science. The first application of optical tweezer in biological science was found in Ashkin's work, where he trapped organic materials (viruses, bacteria and cells) with an argon laser [9]. Since then the applications of optical trap have been increasing significantly with every passing day, for instance, in the study of cell sorting [10, 11] and translocation of single cell in microenvironment [12], in the study of mechanical properties of biomolecules [13], interaction of DNA and RNA with proteins [14, 15] and so on. Not only in biological science, applications of optical trapping are also found in medical science for instance, in cancer diagnosis [16], diagnosis of malaria [17], to measure the deformability of RBC [18, 19] and so on. Optical tweezers also find significant number of applications in physical sciences to measure the viscosity and surface tension of fluid and droplets [20, 21] and rheological properties of matter in liquid [22, 23]. The principle of optical trap is also applicable in a magneto-optical trap to observe atom cooling and trapping [24, 25] and to study the Brownian motion of microsphere in aqueous solution [26, 27].

Most of the above important applications need a proper theoretical understanding of the origin of the force in an optical trap. Only an accurate theoretical model can facilitate computing the various forces acting on the trapped particle so as to realize an efficient trap. Improvement of trapping efficiency in axial and transverse directions and stability of the trap are very important factors for any application of the optical trap [28–30]. An appropriate theoretical force calculation model also helps to investigate the quality and strength of an optical trap and thus the dynamical behavior of the trapped particle [31, 32].

There are primarily two theoretical regimes to obtain the forces in an optical trap depending on the size of the trapped particle relative to the wavelength of the laser beam. One is Rayleigh regime where the particle size is much smaller than wavelength of light, and the other regime is ray-optics regime where the particle size is greater than the wavelength of light.

In the Rayleigh regime, the particle is considered as an infinitesimal point dipole in the instantaneous electric field due to the light beam [33]. The optical forces in the trap is obtained in terms of two components, namely, the scattering force and the gradient force by assuming an appropriate electromagnetic model. This allows calculation of optical force on particles having size less than and comparable to the wavelength of light [34, 35]. However, the complexity of the calculation in electromagnetic models increases with an increase of particle size, for complex particle structure, and for different complex structured beams.

For bigger particles (i.e. particle size $>>\lambda$) force on the trapped particle can be calculated in the geometrical optics or ray-optics regime. Roosen and co-workers [36, 37] gave the first theoretical expressions to explain the optical levitation problem in the ray-optics regime. Ashkin, in 1992, proposed the first comprehensive model to compute the optical force in the ray optics regime by using the laws of geometrical optics and considering the incident beam of light as sum of infinite number of rays with given power, momentum, direction and polarization [38]. Soon there were further works based on the solid geometry ray-tracing method [39, 40] to calculate the trapping forces. In most cases, the solid geometry ray tracing method works for two situations: paraxial low focus condition and non-paraxial tight focus condition. Paraxial focus is not relevant in most of the applications involving single beam gradient trap as such applications require tightly focused beams.

Under non-paraxial conditions, when the beam is strongly focused, the rays converge (forming a cone-like structure) to the focus. Ashkin's work on single-beam gradient trap on dielectric sphere [41] can be categorized as ray-pencil model that applies under both paraxial and non-paraxial conditions. There have been some further works using the ray-pencil model such as to study the influence of glass-water interface [40] and oil-water interface on trapping forces [42]. Each ray can also be considered as a vector to take into account the direction and incident angle of ray to calculate the force as well as torque on a trapped ellipsoid [43]. The optical force has been calculated in the ray optics regime to study the effect of spherical aberration on the trapped sphere [44], for a radially polarized beam [45] and for cylindrically symmetric beam profiles [46]. Recently, S.Zhang et al.[47] showed a ray-optics model considering the ray tracing of Gaussian beam as a one-sheet hyperboloid which works for both paraxial and non-paraxial conditions .

As already stated, the electromagnetic models for optical force are more appropriate for smaller particles when the particle size is comparable to the wavelength of light. However, in several applications especially in the area of biological and biomedical sciences, the trapped particle or object can be several times the wavelength in size. Therefore for such applications, ray-optics model can be more efficient in predicting in the various forces acting on the particle. The ray-pencil model of optical force calculation is applicable for bigger particles under tight focusing conditions using a high numerical aperture lens. However, such models have mostly been used for Gaussian beam profiles assuming a flat wavefront at the entrance pupil of the focusing lens. Although there have been some recent developments in the ray optics regime for non-Gaussian beams as well, however only cylindrically symmetric beam profiles are considered. Thus ray-pencil model needs further development to be more robust and to be easily applicable for non-Gaussian in particular arbitrary amplitude profiles and arbitrary phase profiles. Besides, in the last couple of decades, there has been a lot of interest in vector beams [48] and beams with arbitrary polarization profiles which can also be accompanied by an arbitrary phase profile [49]. Ray-pencil model needs to be further developed for trapping applications [50] involving such vectors beams.

In this thesis, we start with the ray-pencil model of Ashkin [41] and adapt it to compute optical forces on a dielectric sphere for an incident beam carrying an arbitrary amplitude and phase profile. We use two approaches to accomplish the above, where in one, we trace rays from a known wavefront at the exit pupil, while in the other we trace rays from the entrance pupil of the lens by using exact ray tracing. We first show that results obtained using our proposed augmented model agree with the corresponding results obtained using the cylindrical polar coordinates for of the ray-pencil model [8]. Further to demonstrate the correctness of our proposed force calculation model experimentally, we develop a dynamic holographic optical trap using a nematic liquid crystal spatial light modulator (NLCSLM). The experimental arrangement includes a Labview program that controls display in the NLCSLM and the image capturing of the trapped bead by the camera. We configure the setup to be able to provide uniform velocity and acceleration to the trapping beam. Images of moving beads when the trapping beam is moving with a constant speed or acceleration can be analyzed to estimate the optical force acting on the trapped bead under various conditions. We compared the experimentally measured optical forces with those obtained by our proposed model for different beam profiles, powers and focusing lenses. Reasonable agreement of the experimental results with the theoretical results demonstrate the accuracy of our force calculation model.

Below we provide chapter wise overview of the thesis work.

Thesis overview

Chapter1 introduces optical trapping or optical tweezer in general and its applications. It then provides a brief overview of the reported force calculation models in different regimes. The chapter then discusses the need for a robust model that can work for arbitrary amplitude and phase profiles associated with the beam and thus elaborates objective of the thesis work.

Chapter2 starts with the principle of the ray-pencil model proposed by Ashkin and then introduces the proposed augmented model to adapt Ashkin's force expressions for different beam profiles. The model is then employed to study the optical forces on beads using different beam profiles, powers and focusing lenses.

Chapter3 describes the principle of computer generated holography and development of a dynamic holographic optical trap using a nematic liquid crystal spatial light modulator. Results of some proof of principle experiment are presented.

Chapter4 begins with the description of the experimental method to estimate the optical force acting on trapped bead. It then illustrates the experimental tools to implement the said method. The chapter then estimates optical forces on beads under various conditions and beam profiles. The respective optical forces under equivalent conditions are also computed using the proposed model and compared with the experimental results.

Chapter5 concludes the thesis work with a summary and a brief discussion on future prospects.

1.2 Summary

This chapter has provided a general introduction and research objectives of the thesis work. We have first discussed the definition and historical overview of optical trapping and optical tweezers. Then importance of optical tweezers have been discussed in various fields of science. We have explained briefly the importance of force calculation model for optical trapping applications and the existing force calculation models in different regimes. We have then introduced the objective of the thesis that is to augment the existing form of the ray-pencil model and to demonstrate its validity both numerically and experimentally. The chapter ends with brief discussion of the chapter wise thesis overview.

★ ★ ★

CHAPTER 2

Force Calculation Model of Optical trapping

2.1 Introduction

In this chapter, we discuss about optical force calculation especially on larger particles by using theoretical models. We first show why models in the geometrical optics regime are more appropriate for calculating the optical force involved in most of the present day applications. We elaborate force calculation using the ray-pencil model. We then introduce a modification in the existing ray-pencil model in order to be able to compute the optical force due to a beam with arbitrary phase profile. The chapter presents two versions of the proposed modification, in one version, we use gradient of the incident wavefront to obtain the incident ray directions while in the other version we use exact ray tracing through the focusing lens to get the ray directions. The chapter ends with results of numerical simulation where we compare the results obtained with our modified model with those of obtained with the existing ray-pencil model.

2.2 Optical force calculation models in different regimes

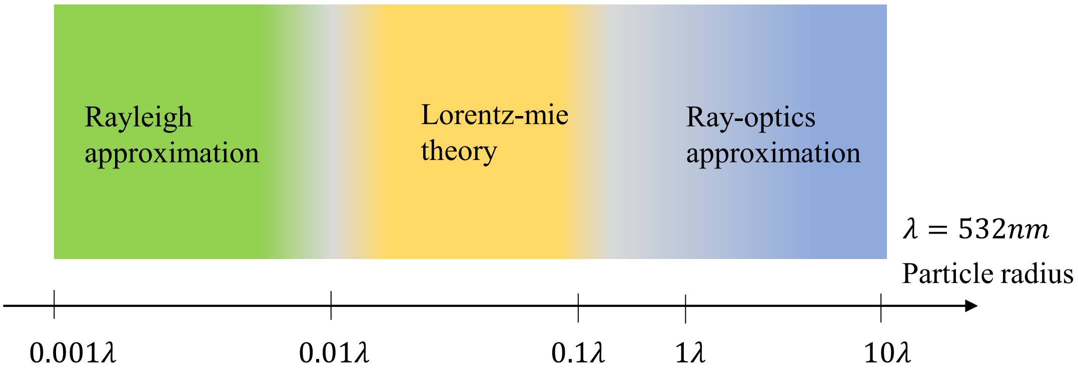

Fig. 2.1 Three different approximation regimes of optical trapping depending on the particle size and wavelength of light.

There are two primary regimes to explain the origin of optical force on a particle in a trap. Selection of the regime depends on the relative size of the particle with respect to the wavelength of the laser beam. In one regime the laws of electromagnetic theory are used to develop the model for trapped particles whose size is less than or equal to the wavelength of light. However, for trapped particles whose size is bigger compared to the wavelength of light, the laws of geometrical optics are used to explain the optical trapping force. The electromagnetic regime can be further divided into Rayleigh regime applicable for particles much smaller than the wavelength of light and intermediate regime valid for particles whose size is comparable to the wavelength of light. Table 2.1 shows the suitable particle size (a) for force calculation models in different regimes while Fig. 2.1 shows a pictorial representation of the appropriate model for a given particle size.

Table 2.1 **Different regimes of optical trapping.**

Electromagnetic wave regime		**Geometrical-optics regime**
Rayleigh regime	Intermediate regime	
Particle size (a) $\ll \lambda$	$a \sim \lambda$	$a \gg \lambda$

As stated already in the Rayleigh regime the trapped particle is approximated as an infinitesimal point dipole in an electric field [33]. Here the optical forces originate due to the scattering of electromagnetic wave by the spherical particle. In the presence of the electric field the particle acts as an oscillating dipole. The oscillating dipole scatters the electromagnetic waves in all directions which changes the magnitude and direction of the energy flux of the incident electric field. The changes in the energy flux results in a change in momentum of the dipole and the corresponding force, known as scattering force. The expression of the scattering force can be written as

$$\vec{F}_{scat}(\vec{r}) = (\frac{n_{med}}{c})\sigma_{scat}\vec{I}(\vec{r}) \tag{2.1}$$

where, n_{med} is refractive index of medium, c is velocity of light, and $\vec{I}(\vec{r})$ is the intensity of the electric field. Further σ_{scat} is the scattering cross-section given as

$$\sigma_{scat} = \frac{8}{3}\pi k^4 a^6 \left(\frac{n_{eff}^2 - 1}{n_{eff}^2 + 2}\right)^2 \tag{2.2}$$

where, $k = \frac{2\pi}{\lambda}$ is the wave number, a is radius of the particle, $n_{eff} = \frac{n_p}{n_{med}}$ is the ratio of refractive indices of the particle and medium. Substituting Eq. 2.2 in Eq. 2.1 we get

$$\vec{F}_{scat}(\vec{r}) = \frac{8}{3}\pi k^4 a^6 (\frac{n_{med}}{c}) \left(\frac{n_{eff}^2 - 1}{n_{eff}^2 + 2}\right)^2 \vec{I}(\vec{r}) \tag{2.3}$$

So, the scattering force is axial in nature and it pushes the dipole along the z (i.e. propagation direction). Additionally, there exists another force namely the gradient force which is primarily responsible for trapping. The gradient force in Rayleigh regime is the time averaged Lorentz force acting on the polarized dipole in an electric field [51]. Its expression is given as

$$\begin{aligned} \vec{F}_{grad}(\vec{r}) &= \left\langle (\vec{p}(\vec{r},t)\cdot\nabla)\vec{E}(\vec{r},t) \right\rangle_T \\ &= \frac{2\pi n_{med} a^3}{c} \left(\frac{n_{eff}^2 - 1}{n_{eff}^2 + 2}\right) \nabla I(\vec{r}) \end{aligned} \tag{2.4}$$

Using Rayleigh approximation we can compute the trapping forces on atoms, proteins, viruses etc whose size is less compared to the wavelength of light [52, 53]. For modeling of trapping forces on microscopic particles whose size is comparable to the wavelength of light, Rayleigh approximation is not appropriate. For such particles on the other hand models in the intermediate regime also known as Mie regime can be used to calculate the trapping forces. The scattering of a plane-wave by spherical particles can be analyzed by using Lorentz-Mie theory (LMT) [54]. However optical tweezers use highly focused beam where plane wave scattering approximation is insufficient. Therefore, a generalized theory of scattering known as generalized Lorentz-Mie theory (GLMT) has been developed [55, 56]. However, the GLMT approach is much more computationally intensive as it requires calculation of three scattering cross sections and beam-shape coefficients (BSCs) of the scattered field.

From the above discussions, it is evident that electromagnetic theory is more appropriate for computing trapping forces on smaller particles. For bigger particles complete electromagnetic theory can be employed, but the method is much more complex and requires more computational time. However, most of the present day applications of the optical tweezers involve trapping of large biological objects [57, 58]. The biological objects have sizes much greater than the wavelength of light. Hence for convenient computation of trapping forces in case of such applications, models in the geometrical-optics regime are more appropriate. Ray-optics approximation of the optical trapping phenomenon is simpler and gives quite reasonable results. Besides, recently the optical traps have been realized using not just Gaussian beams but other complex beams such as vortex beams or cylindrical vector beams. The ray-optics model can be easily reconfigured to be applicable for such complex beams. A review of the available literature shows that the ray-optics model for optical trap proposed by A.Ashkin [6, 41] has been successfully employed in a number of different situations [45, 59]. Below we will discuss the origin and mathematical formulation of trapping forces in the ray-optics regime.

2.3 Optical trapping in Ray-optics regime

2.3.1 Origin of the optical forces

Origin of the optical force on a particle in the ray-optics regime is explained on the basis of conservation of linear momentum. The incident light beam is considered as a bunch of rays

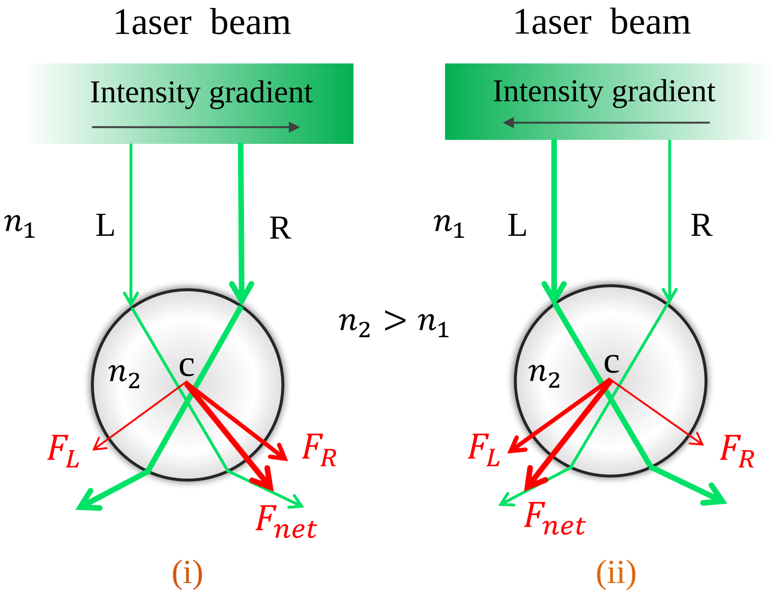

Fig. 2.2 Directions of net optical force on a sphere for a laser beam with intensity increasing from (i) left to right, and (ii) from right to left.

each with suitable intensity, momentum, direction and state of polarization. When the rays are incident on a particle suspended in a given medium they get reflected and refracted according to the laws of geometrical optics, depending on appropriate refractive index of the particle. The momentum associated with the reflected or refracted ray thus undergoes a change. However, net moment of the entire system must be conserved, and to conserve the net momentum the particle experiences the optical forces. Figure 2.2 (i) shows a spherical particle illuminated by a collimated beam whose intensity increases from left to right. Two rays of different intensities, L with low intensity and R with high intensity are incident on the particle. Both the rays undergo refraction as shown in Fig. 2.2 (i). The change in momentum gives rise to forces F_L and F_R that act on the particle. Since R has higher power than L the particle experiences a net force F_{net} which is in the bottom-right direction. Figure 2.2 (ii) shows similarly the spherical particle illuminated by a collimated beam whose intensity increases from right to left. Proceeding the same way we will see that the net force on the particle F_{net} now acts in the bottom-left direction.

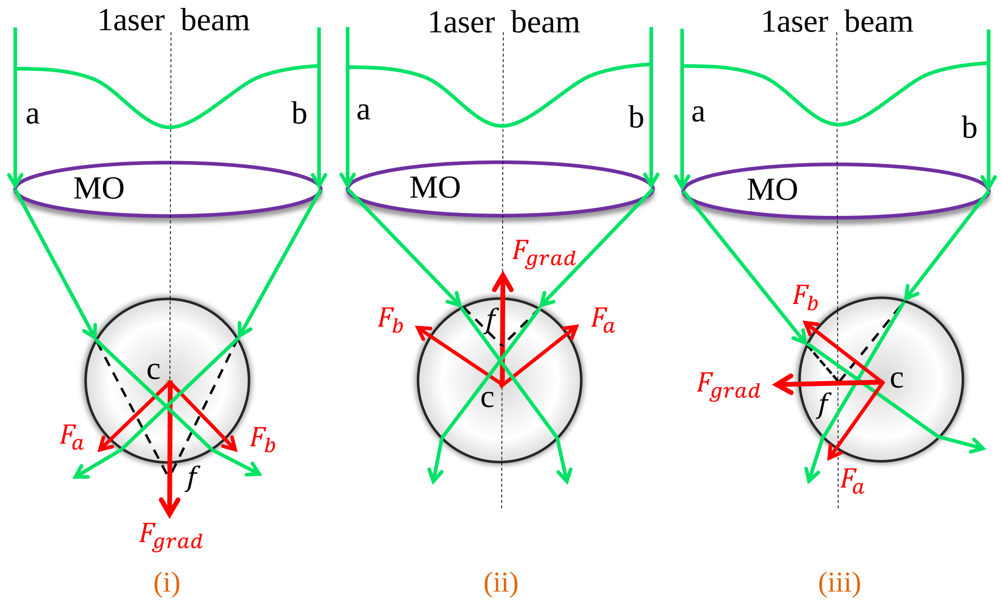

Fig. 2.3 Optical trapping force due to a focused Gaussian beam in three different situations where, (i) particle is located above the focus of the beam, (ii) particle located below the focus of the beam and (iii) particle is located off-axis.

A laser beam usually has a Gaussian intensity profile where the intensity peaks on the axis. Figure 2.3 shows such a laser beam focused on a spherical particle. We consider a pair of incident rays a and b symmetrically situated and of same intensity, both of which get refracted through the spherical particle. Based on our discussion in the above case we can see that refraction of the two rays give rise to forces F_a and F_b. If the center of the particle is above the focus of the beam as shown in Fig. 2.3 (i) then the net force F_{grad} on the particle is in the downward direction. If the center of the particle is below the focus of the beam as shown in Fig. 2.3 (ii) then the net force F_{grad} on the particle is in the upward direction. On the other hand if the particle is shifted slightly to the right of the focus as seen in Fig. 2.3 (iii) then the net force F_{grad} on the particle is in the left direction. Thus if the particle is displaced from the focus either in the axial or transverse directions by a small amount, it experiences a restoring force in the opposite direction. The optical forces arising due to conservation of momentum of the system lead to trapping of the particle near the focus.

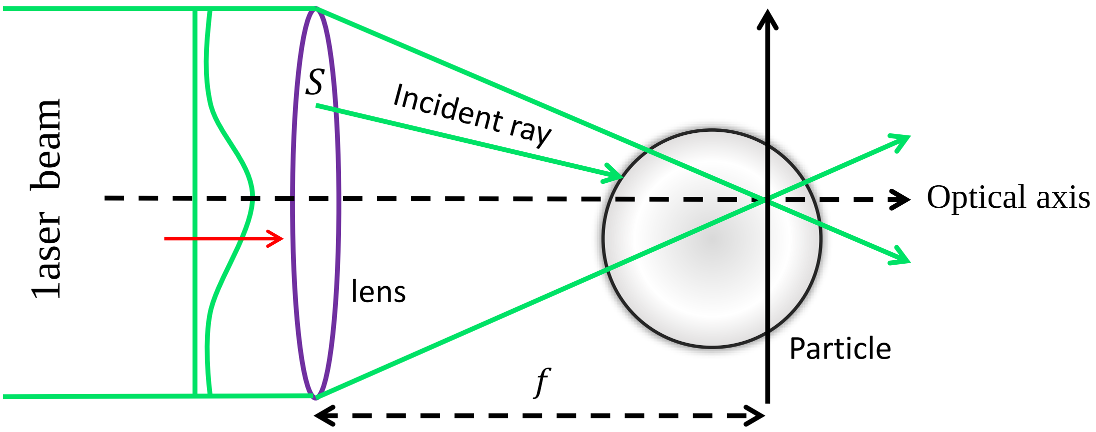

Fig. 2.4 Schematic diagram representing ray-pencil model.

2.3.2 Mathematical formulation of force calculation model in the ray optics regime

Optical force calculation models in the ray-optics regime can be divided into two types, namely, the ray-pencil model and the spherical wavefront model (SWF model). Figure 2.4 is a representative diagram of the ray-pencil model [41, 8]. This model considers a highly focused laser beam which makes a cone like structure after focusing by the lens. The focus of the lens is also the position of the beam waist where the particle gets trapped. For calculation of force, the direction of each incident ray is first determined from the known initial coordinate (say S as shown in Fig. 2.4) of the ray at the lens surface and the focal point. On the other hand the spherical wavefront (SWF) model provides the optical trapping forces in the paraxial low focus condition [60, 61]. Figure 2.5 shows a spherical wavefront of radius of curvature r_P intersecting the particle at point P. We now have

$$r_p = z_p \left[1 + (\frac{z_r}{z_p})^2\right] \tag{2.5}$$

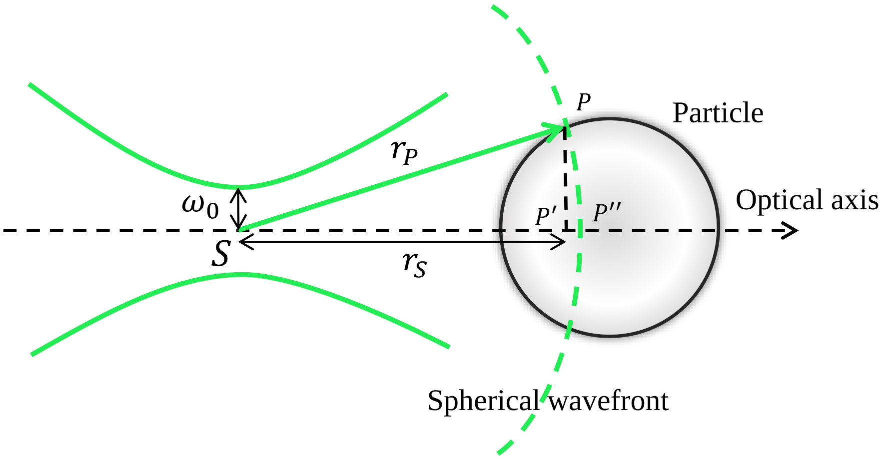

Fig. 2.5 Schematic diagram depicting the spherical wavefront model.

where, z_r is the Rayleigh length and is given by

$$z_r = \frac{\pi \omega_0^2}{\lambda} \tag{2.6}$$

Here ω_0 is the beam waist and λ is wavelength of light. z_p is the distance between S and P' which is the z coordinate of P and S is the position of beam waist. The model uses the approximation $|SP'| = |SP''|$, which is the case when r_P is very large or when the wavefront is almost planar. Net force on the particle is obtained by integrating over all the rays those are incident on the particle within the cone. The limit of the integration are obtained from the direction of $\vec{r_p}$. However, the SWF model provides correct optical trapping force only under paraxial focusing conditions. On the contrary the ray-pencil model is applicable for both paraxial and strong focus conditions.

Force due to a single ray

Figure 2.6 (i) shows a single ray with power dP incident on a dielectric sphere at an angle of incidence α. The incident momentum is $n_{med}\, dP/c$ where n_{med} is the refractive index of the medium. Part of the incident ray gets reflected with power dPR and the refracted ray undergoes infinite number of reflections and refractions in succession with decreasing powers, dPT^2, dPT^2R,...., dPT^2R^n. Here R and T are the Fresnel reflection and transmission coefficients,

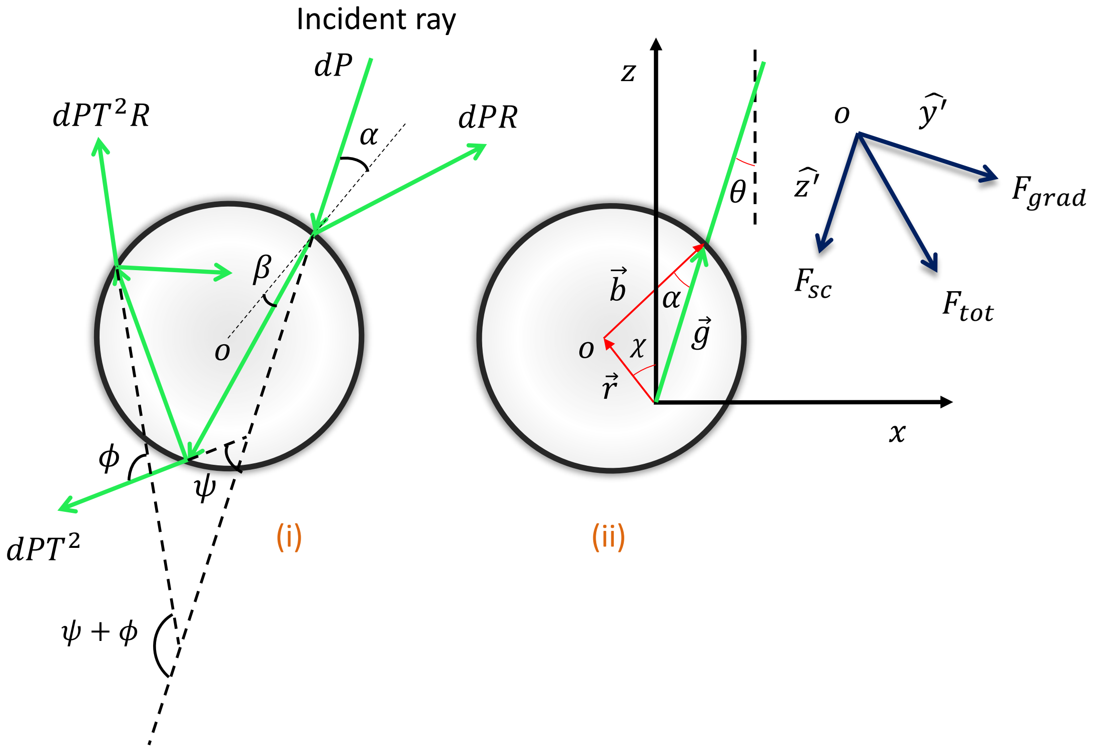

Fig. 2.6 Geometry for force calculation in the ray optics regime due to a single incident ray of power dP. (i) shows the multiple reflections and refractions of the single ray incident on the spherical particle and (ii) shows the geometry to calculate the incident angle when the sphere is shifted by $\vec{r}$ from the focus.

respectively. Due to the momentum change experienced by this single ray a force acts through the center of the sphere. This force can be divided into two components $dF_{z'}$ acting along $\hat{z'}$ and $dF_{y'}$ acting along $\hat{y'}$ given as [38]

$$dF_{z'} = \frac{n_{med} dP}{c} - \left[\frac{n_{med} dPR}{c}\cos(\pi - 2\alpha) + \sum_{n=0}^{\infty} \frac{n_{med} dPT^2 R^n}{c}\cos(\psi + n\phi)\right] \tag{2.7}$$

and

$$dF_{y'} = 0 - \left[\frac{n_{med} dPR}{c}\sin(\pi - 2\alpha) - \sum_{n=0}^{\infty} \frac{n_{med} dPT^2 R^n}{c}\sin(\psi + n\phi)\right] \tag{2.8}$$

We combine the two components in complex plane as $dF_{tot} = dF_{z'} + idF_{y'}$, so that we can write

$$dF_{tot} = \frac{n_{med} dP}{c}(1 + R\cos 2\alpha) - i\frac{n_{med} dPR}{c}\sin 2\alpha - \frac{n_{med} dPT^2}{c}\sum_{n=0}^{\infty} R^n e^{-i(\psi + n\phi)} \tag{2.9}$$

Taking real and imaginary parts we get

$$dF_{z'} = \frac{n_{med}dP}{c}\left[1 + R\cos(2\alpha) - \frac{T^2[\cos(2\alpha - 2\beta) + R\cos(2\alpha)]}{1 + R^2 + 2R\cos(2\beta)}\right] \tag{2.10}$$

and

$$dF_{y'} = -\frac{n_{med}dP}{c}\left[R\sin(2\alpha) - \frac{T^2[\sin(2\alpha - 2\beta) + R\sin(2\alpha)]}{1 + R^2 + 2R\cos(2\beta)}\right] \tag{2.11}$$

More details about the derivation of the above force components can be found in Appendix A.

The force $dF_{z'}$ as given by Eq.2.10 is called scattering force which acts in the propagation direction of the incident ray and the force $dF_{y'}$ as given by Eq.2.11 is called the gradient force which acts perpendicular to the scattering force. Both the force components depend on the power dP carried by the ray, refractive index of the medium, angle of incidence, and angle of refraction. To be noted that since the Fresnel transmission and reflection coefficients R and T depend on polarization of light [1] the two forces are also polarization dependent. If we consider the light to be randomly polarized or circularly polarized so that each ray has equal amount of s and p polarizations then we can write

$$R(\alpha,\beta) = \frac{1}{2}\left[\frac{\sin(\alpha-\beta)}{\sin(\alpha+\beta)}\right]^2 + \frac{1}{2}\left[\frac{\tan(\alpha-\beta)}{\tan(\alpha+\beta)}\right]^2 \tag{2.12}$$

and

$$T(\alpha,\beta) = 1 - R(\alpha,\beta) \tag{2.13}$$

The net force on the sphere due to a single ray therefore is

$$d\vec{F} = (n_{med}/c)[Re(Q_{trap})\hat{z'} + Im(Q_{trap})\hat{y'}]dP \tag{2.14}$$

where,

$$Q_{trap} = 1 + R\exp(-2i\alpha) - T^2\frac{\exp[-2i(\alpha-\beta)]}{1 + R\exp(2i\beta)} \tag{2.15}$$

is called as trapping efficiency. Hence, the force experienced by the dielectric sphere for a given ray can be calculated using Eq. 2.14 provided the respective (α,β) and (R,T) values are known. In this work we assume R and T values as given by Eqs. 2.12 and 2.13.

Net force due to a tightly focused Gaussian beam

Considering all the rays incident on the sphere the net force on it can be obtained by vectorially adding $d\vec{F}$ due to each ray. Therefore,

$$\begin{aligned}\vec{F} &= \sum d\vec{F} && (2.16)\\ &= \sum \frac{n_{med}}{c}[Re(Q_{trap})\hat{z'} + Im(Q_{trap})\hat{y'}]dP && (2.17)\end{aligned}$$

The elementary power element dP depends on the intensity distribution at the entrance pupil of the objective lens. In this thesis we denote the components of the net force along x, y and z as F_x, F_y and F_z.

In most of the cases the intensity distribution at the entrance pupil is considered as Gaussian distribution in which case the intensity at the location $\rho(x,y)$ in the pupil plane is given as

$$I(x,y) = I_o \exp(\frac{-\rho^2}{2\sigma^2}) \tag{2.18}$$

where σ is the beam waist and $\rho = \sqrt{x^2+y^2}$. We are expressing the power using cylindrical co-ordinates as the Gaussian distribution has a cylindrical symmetry. The power in the elemental area dA at (x,y) in the pupil plane is $dP = I(\rho)dA$, which is also taken as the power in the corresponding ray passing through (x,y). If P_{tot} is the net power in the Gaussian beam then

$$\begin{aligned}dP &= \frac{P_{tot}}{2\pi\sigma^2}\exp(-\frac{\rho^2}{2\sigma^2})dA\\ &= \frac{P_{tot}}{2\pi\sigma^2}\exp(-\frac{\rho^2}{2\sigma^2})\rho d\rho d\varphi && (2.19)\end{aligned}$$

since in cylindrical polar coordinates, the elementary area $dA = \rho d\rho d\varphi$. Now, considering the objective lens obeys Abbe's sine condition, that is

$$\rho = \sqrt{x^2+y^2} = f\sin\theta \tag{2.20}$$

where, θ is the angle the ray makes with the optical axis of objective lens. Thus the angle made by the ray with the z axis is decided by the radial distance from the axis in the pupil plane. Hence

$$dP = \frac{P_{tot}}{2\pi\sigma^2} \exp\left(\frac{-f^2 \sin^2\theta}{2\sigma^2}\right) f^2 \sin\theta \cos\theta \, d\theta d\varphi \tag{2.21}$$

Substituting Eq.2.21 in Eq.2.17 we get [8]

$$\vec{F} = \int_0^{\theta_0} \int_0^{2\pi} \frac{n_{med}}{c} [Re(Q_{trap})\hat{z}' + Im(Q_{trap})\hat{y}'] \frac{P_{tot}}{2\pi\sigma^2} \exp\left(\frac{-f^2 \sin^2\theta}{2\sigma^2}\right) f^2 \sin\theta \cos\theta \, d\theta d\varphi \tag{2.22}$$

In the above Eq.2.22 the unit vectors are expressed as

$$\hat{z}' = (-\sin\theta\cos\varphi, -\sin\theta\sin\varphi, -\cos\theta) \tag{2.23}$$

and

$$\hat{y}' = \frac{\hat{z}' \times (\vec{r} \times \hat{z}')}{|\hat{z}' \times (\vec{r} \times \hat{z}')|} \tag{2.24}$$

The expression of the incident angle α can be derived using Fig.2.6 (ii) as

$$\alpha = \cos^{-1}\left[\frac{g^2 + b^2 - r^2}{2bg}\right] \tag{2.25}$$

where,

$$\begin{aligned} g = \sqrt{b^2 - r^2 + r^2(\sin\chi\sin\theta\cos\varphi + \cos\chi\cos\theta)^2} \\ + r(\sin\chi\sin\theta\cos\varphi + \cos\chi\cos\theta) \end{aligned} \tag{2.26}$$

Using Snell's law

$$\beta = \sin^{-1}\left(\frac{n_{med}}{n_s}\sin\alpha\right) \tag{2.27}$$

where, n_s is the refractive index of sphere. The value of θ_0 is decided by the numerical aperture of the focusing lens or the critical angle of incidence on the glass coverslip in case the specimen slide containing the dielectric sphere uses a glass coverslip, which ever is smaller. Thus the net force on the dielectric sphere in the x, y and z directions can be calculated for a Gaussian incident beam of a given power P_{tot} by performing the integration in Eq. 2.22.

2.4 Augmented ray-pencil model to calculate optical forces

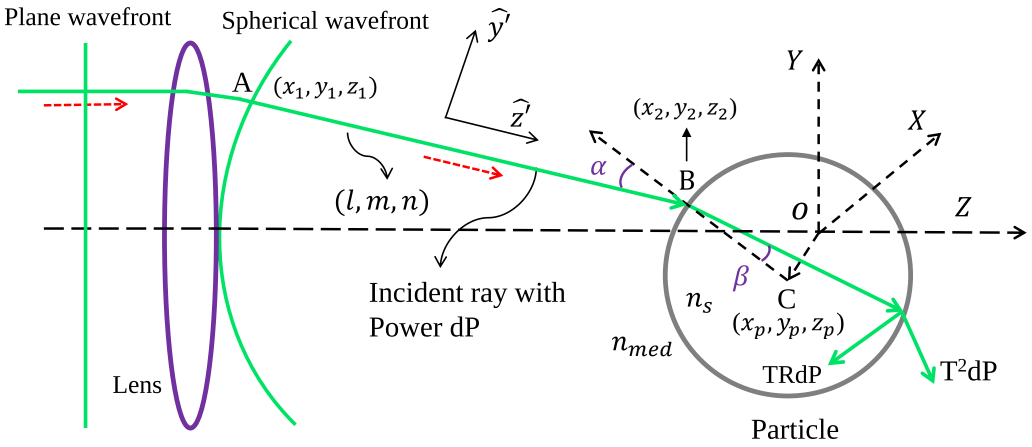

Fig. 2.7 A schematic diagram showing a ray with given direction cosines getting incident on a dielectric sphere.

In the ray-pencil model discussed in the previous section one must know the direction of each ray and its angle of incidence on the dielectric sphere. For a plane wave and an ideal lens following Abbe's sine condition the angle made by a certain ray with the optical axis is determined by the radial distance of the ray from the optical axis in the exit pupil plane. The integral expression of optical force expressed in cylindrical polar coordinate discussed in section 2.3 considers cylindrically symmetric beam profiles to derive the value of incidence angle α and the direction of the gradient force. However, the beam profile in many applications may not be cylindrically symmetric. One may often encounter lack of cylindrical symmetry when the beam is distorted due to aberrations or when some complex beam such as vortex beam is used for trapping. For such beams a ray may not subtend an angle as per Abbe's sine condition. For all such cases the ray-pencil model discussed in the previous section is not sufficient. Below, we propose an augmentation of ray-pencil model that enables optical force calculation for any arbitrary beam profiles including aberrated beams and complex beams.

Let (l, m, n) be the direction cosines of the ray which passes through the point A(x_1, y_1, z_1) in the exit pupil of the lens, as shown in Fig. 2.7. We consider that the dielectric sphere of radius a is kept with its center at $(x_p,\ y_p,\ z_p)$. We further assume that the ray with direction cosines $(l,\ m,\ n)$ intersects the dielectric sphere at B(x_2,y_2,z_2). The parametric equation of the incident ray is

$$\frac{x - x_1}{l} = \frac{y - y_1}{m} = \frac{z - z_1}{n} \tag{2.28}$$

while the equation of the sphere is $(x - x_p)^2 + (y - y_p)^2 + (z - z_p)^2 = a^2$. Therefore (x_2,y_2,z_2) satisfies the equation

$$\left[\frac{l}{n}(z_2 - z_1) + x_1 - x_p\right]^2 + \left[\frac{m}{n}(z_2 - z_1) + y_1 - y_p\right]^2 + \left[z_2 - z_p\right]^2 = a^2 \tag{2.29}$$

The above Eq. 2.29 is a quadratic equation in z_2, which can be written as

$$C_1 z_2^2 + C_2 z_2 + C_3 = 0 \tag{2.30}$$

where

$$\begin{aligned} C_1 &= 1 \\ C_2 &= (-2l^2 z_1 + 2lnx_1 - 2m^2 z_1 + 2mny_1 - 2lnx_p - 2mny_p - 2n^2 z_p) \\ C_3 &= (l^2 z_1^2 - 2lnx_1 z_1 + n^2 x_1^2 + m^2 z_1^2 - 2mny_1 z_1 + n^2 y_1^2 + 2lnx_p z_1 \\ &\quad -2n^2 x_1 x_p + 2mnz_1 y_p - 2n^2 y_1 y_p + n^2 x_p^2 + n^2 y_p^2 + n^2 z_p^2 - n^2 a^2) \end{aligned} \tag{2.31}$$

The ray will intersect the sphere only if

$$C_2^2 - 4C_1C_3 > 0 \tag{2.32}$$

Solution of Eq. 2.30 is given as

$$z_2 = \frac{-C_2 - \sqrt{C_2^2 - 4C_1C_3}}{2C_1} \tag{2.33}$$

Although there is one more solution given as $z_2 = \frac{-C_2+\sqrt{C_2^2-4C_1C_3}}{2C_1}$, however the same is not considered, as we take the smaller solution to correspond to the intersection point. Knowing z_2 from Eq. 2.33 we can get

$$x_2 = l\frac{z_2 - z_1}{n} + x_1,\ y_2 = m\frac{z_2 - z_1}{n} + y_1 \tag{2.34}$$

We then define $\vec{r} = (x_p - x_2)\hat{x} + (y_p - y_2)\hat{y} + (z_p - z_2)\hat{z}$, whose unit vector is

$$\hat{r} = \frac{x_p - x_2}{r}\hat{x} + \frac{y_p - y_2}{r}\hat{y} + \frac{z_p - z_2}{r}\hat{z} \tag{2.35}$$

where $r = \sqrt{(x_p - x_2)^2 + (y_p - y_2)^2 + (z_p - z_2)^2}$. For the ray starting from (x_1, y_1, z_1) on the exit pupil, the value of α is then given as

$$\alpha = \cos^{-1}(\hat{r}.\hat{z'}) \tag{2.36}$$

and the respective β will be given by the Eq. 2.27. The direction of the gradient force, $\hat{y'}$ is given by Eq. 2.24.

2.4.1 Gradient of wavefront approach to obtain the direction cosines of the ray in the image space

A plane wave incident on the entrance pupil of an ideal lens becomes a spherical wavefront in the exit pupil [62]. The equation of the spherical wavefront at the exit pupil considering such an ideal lens of focal length f is given by $x^2 + y^2 + (z - f)^2 = f^2$ where we assume that the origin of the coordinate system coincides with the intersection point between the optical axis of the lens and the focal sphere. Hence

$$z = f - \sqrt{f^2 - x^2 - y^2} \tag{2.37}$$

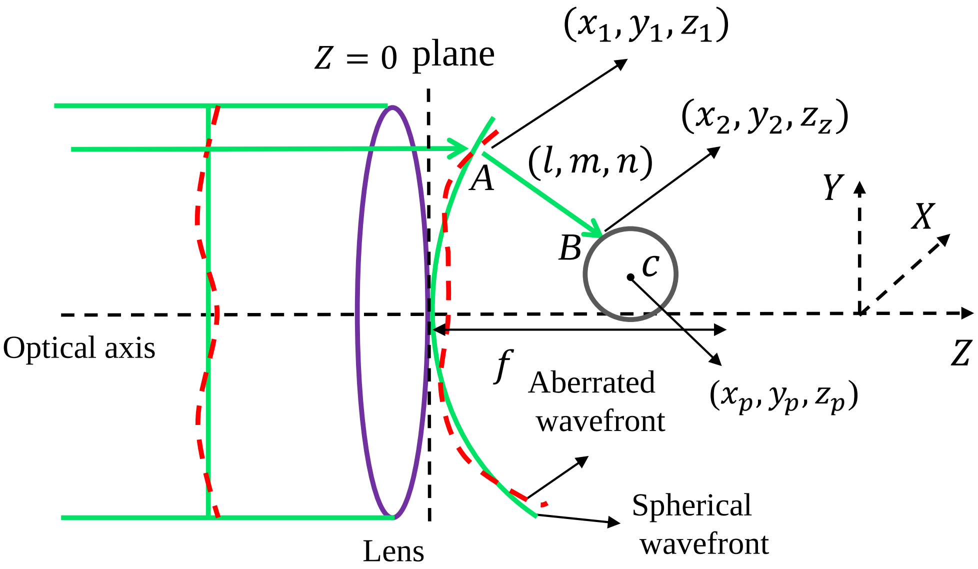

Fig. 2.8 Gradient of wavefront giving the direction of a ray in the exit pupil. The exit pupil intersects the optical axis in the z = 0 plane.

If the beam contains an additional phase profile represented by $\phi(x,y)$, the above equation gets modified as

$$z = f - \sqrt{f^2 - x^2 - y^2} + \frac{\lambda}{2\pi}\phi(x,y) \tag{2.38}$$

such that

$$W(x,y,z) = z + \sqrt{f^2 - x^2 - y^2} - \frac{\lambda}{2\pi}\phi(x,y) - f = 0 \tag{2.39}$$

Considering a point (x_1, y_1, z_1) at the exit pupil, we can obtain the normal to the wavefront at the exit pupil, by taking gradient of $W(x,y)$. Therefore

$$\vec{g} = \vec{\nabla} W(x,y,z)|_{(x_1,y_1,z_1)} = g_1\hat{x} + g_2\hat{y} + g_3\hat{z} \tag{2.40}$$

Hence the direction cosines of the ray at (x_1, y_1, z_1) on the exit pupil will be

$$\begin{aligned} l &= \frac{g_1}{\sqrt{g_1^2+g_2^2+g_3^2}} \\ m &= \frac{g_2}{\sqrt{g_1^2+g_2^2+g_3^2}} \\ n &= \frac{g_3}{\sqrt{g_1^2+g_2^2+g_3^2}} \end{aligned} \tag{2.41}$$

and it makes an angle $\theta = \cos^{-1}(n)$ with the z axis. Hence the direction of the scattering force is

$$\hat{z'} = l\hat{x} + m\hat{y} + n\hat{z} \tag{2.42}$$

where (l, m, n) are given by Eq. 2.41.

2.4.2 Geometrical exact ray tracing approach

Geometrical exact ray tracing is a technique to trace rays of light exactly through any number of refractions on curved surfaces without using paraxial approximations. On the other hand the objective lens that is normally used to setup a single beam optical trap consists of several convex or concave surfaces separated by transparent materials of different refractive indices. Hence starting from the entrance pupil of the lens one can trace the exact path of the rays if the specification of the objective lens is given. Here we use the exact ray tracing technique [63, 64] to obtain direction cosine of each ray on the emergent (i.e. image side) side of the lens. Knowing the direction cosine of each ray constituting an incident beam and its location on the last surface of the lens, we can compute the respective contribution of optical force using Eq. 2.22.

Geometrical exact ray tracing expressions

Figure 2.9 shows the diagram of a single ray starting from A(x_i, y_i, z_i) located in a medium of refractive index n_1 and getting incident at B on a curved surface of radius of curvature c_1 (with C as the center). The curved surface separates the two media with refractive indices n_1 and n_2.

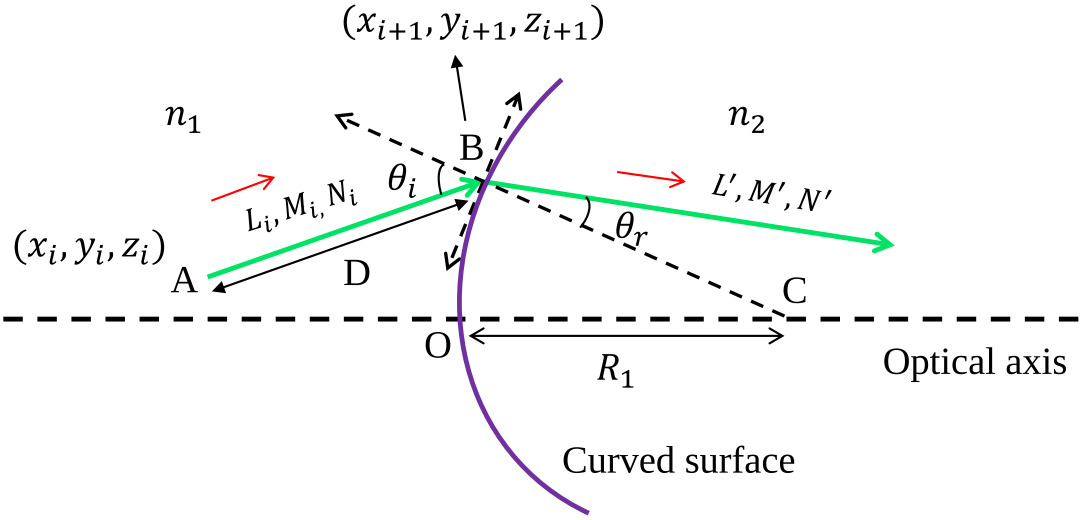

Fig. 2.9 Representative diagram for exact ray tracing as a ray is refracted through a spherical surface.

The incident ray has direction cosines L_i, M_i and N_i. If we assume that the distance between A and B to be D then the coordinates of B are given as

$$\begin{aligned} x_{i+1} &= x_i + L_i D \\ y_{i+1} &= y_i + M_i D \\ z_{i+1} &= z_i + N_i D \end{aligned} \tag{2.43}$$

where,

$$D = \frac{F_{ext}}{G_{ext} + \sqrt{G_{ext}^2 - c_1 F_{ext}}} \tag{2.44}$$

,

$$F_{ext} = c_1(x_i^2 + y_i^2 + z_i^2) - 2z_i \tag{2.45}$$

and

$$G_{ext} = N_i - c_1(L_i x_i + M_i y_i + N_i z_i) \tag{2.46}$$

After refraction at the curved surface, the final direction cosines of the ray will be

$$\begin{aligned} L' &= qL_i + \alpha_{ext}(\cos\theta_r - q\cos\theta_i) \\ M' &= qM_i + \beta_{ext}(\cos\theta_r - q\cos\theta_i) \\ N' &= qN_i + \gamma_{ext}(\cos\theta_r - q\cos\theta_i) \end{aligned} \tag{2.47}$$

where, $q = \frac{n_1}{n_2}$, α_{ext} = -c_1x_0, β_{ext} = -c_1y_0, γ_{ext} = (1-c_1z_0), cosθ_i = $\sqrt{G_{ext}^2 - c_1F_{ext}}$ and cosθ_r = $\sqrt{1-q^2(1-\cos^2\theta_i)}$.

So, Eq.2.43 and 2.47 are the important equations to calculate the intersection coordinate B($x_{i+1}, y_{i+1}, z_{i+1}$) and direction cosines L', M', N' after the first transmission of the ray through the curved surface as shown in Fig. 2.9. These equations can be used repeatedly to obtain direction cosine of each ray in the image space for a plane or aberrated wavefront at the entrance pupil. In this case also the direction cosines of the rays in the entrance pupil can be determined by taking gradient of the respective wavefront.

So far we have considered the beam at the entrance or the exit pupil to be scalar only. However our two approaches can be generalized for vector beams as well. This requires calculating the Fresnel coefficients as each ray is incident on the dielectric sphere, in lieu using the Eq. 2.12. In the exact ray tracing approach, each ray can be traced vectorially considering refraction of each orthogonal polarization component separately on each surface, till we get the vectorial form of the ray in the image space. Moreover, the described models work in the ray-optics regime only where the particle size is bigger than the wavelength of light. Although, the models can also work for microscopic particle of any shape, we have considered only spherical particle to calculate the optical trapping force.

2.5 Results and discussions

2.5.1 Gradient approach of the augmented ray-pencil model

In order to assess the accuracy of the proposed augmented ray-pencil model we consider trapping due to focusing by an oil immersion objective lens with NA = 1.4 and 100× magnification.

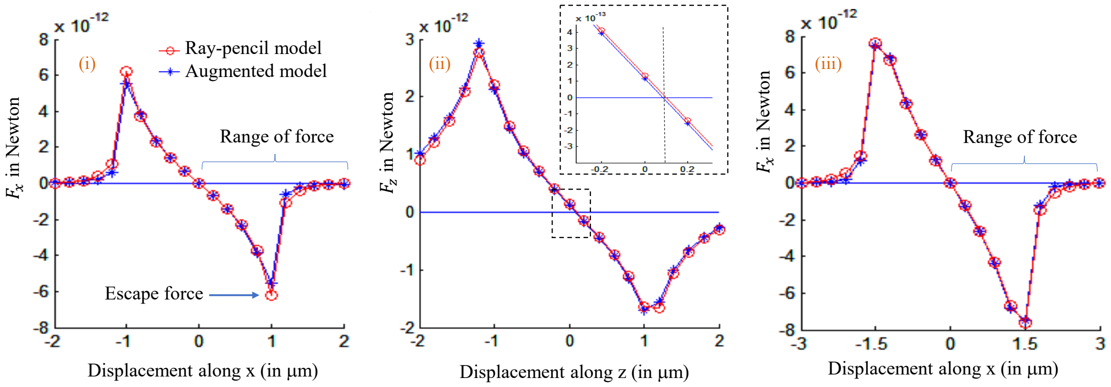

Fig. 2.10 Plots of (i) F_x vs displacement along x and (ii) F_z vs displacement along z of the 2 μm bead, (iii) F_x vs displacement along x of the 3 μm bead, using the ray-pencil model and the gradient approach of the augmented model. Power of the laser beam is 10 mW and focusing is done using the 1.4 NA lens. In all plots the zero displacement value correspond to the focal point.

We first compute various optical forces acting on a 2 μm diameter silica bead of refractive index = 1.46. The results using our model are compared with the same using the ray-pencil model discussed in section 2.3. In our numerical simulation we use the following parameters of the optical trap setup: focal length of lens = 1.8 mm, entrance pupil radius = 2.5 mm, σ = 1.9 mm, and refractive index of medium = 1.343. In our numerical simulation we keep the

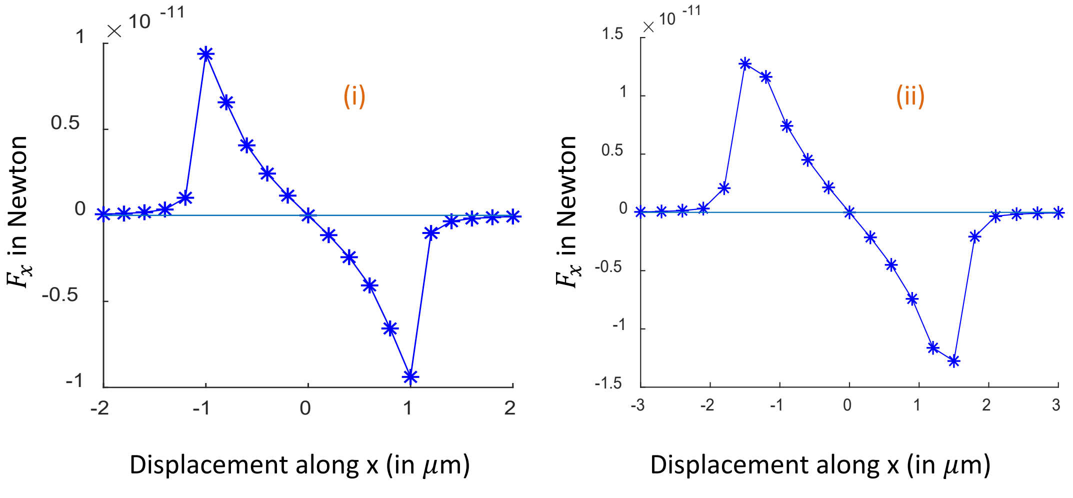

Fig. 2.11 Plots of x-component of the optical force for the (i) 2 μm bead and (ii) 3 μm bead, as they move along the x-axis through the focus. Beam power is 17 mW. Results are obtained using the wavefront gradient approach of the augmented model.

focal point of the lens fixed while we move the center of the dielectric sphere with respect to the focal point. The separation between focus and the center of the sphere is denoted as displacement throughout this thesis. First we move the sphere along the x-axis through the focus of the lens from $x = -2\mu$m to $x = 2\mu$m. We compute the x-component of the net optical force at an interval of 0.1 μm. Figure 2.10 (i) shows the plot of F_x vs displacement of the 2 μm bead using the ray-pencil model and the gradient approach of the augmented model. In our calculation using the augmented model we divide the entrance pupil into 256×256 number of pixels. On the other hand, for the ray-pencil model we use 256 values each of θ and ϕ. It is seen from the Fig. 2.10 (i) that there is a very good agreement between proposed model with the ray-pencil model. We observe that the peak values of the optical force in the +x and -x directions which we also refer to as escape force have nearly the same magnitude and occur at the same displacement for the two models. Moreover, the maximum value of the displacement up to which the optical force is non-zero which we can refer as the range of the optical force are also having the same value for the two models. In order to compare the behavior of the z-component of the optical force for axial displacement of the bead we compute the optical forces on the bead as the bead is moved through the focus along the optical axis. From Fig. 2.10 (ii) we see that the axial forces for axial displacement of the bead using the two models are having almost identical behavior. As expected the force on the bead in the -z direction is greater than the force in the +z direction. On magnifying the central part of the plot as shown in the Fig. 2.10 (ii) it is seen that the axial force crosses the zero axis at around z = 0.09 μm. We then use a larger spherical bead with diameter 3 μm and refractive index = 1.59 in our numerical simulation. As seen in Fig. 2.10 (iii) when we displace the bead along the x-axis from -3 μm to 3 μm, the x-component of the optical forces using the two models show identical behavior. We also observe that the range of the optical force in this case is about 3 μm.

From the above numerical simulation, it is evident that the proposed augmented ray-pencil model is giving accurate values of the optical forces for dielectric sphere of different sizes. We then use our augmented model to simulate the optical forces on the 2 μm and 3 μm beads as the power of the trapping beam is increased to 17 mW. Figures 2.11 (i) and (ii) show the plots of x-component of the optical force for the 2 μm bead and 3 μm bead, respectively, as they

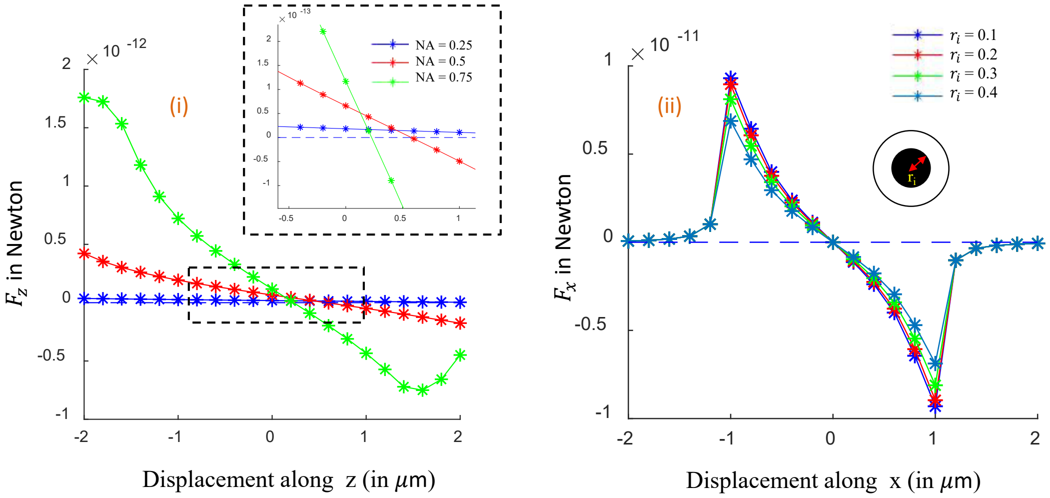

Fig. 2.12 Plots of (i) the z-component of the optical force against the displacement of the bead along the optical axis for different NA, (ii) F_x vs displacement along x for annular beams whose pupil plane is also shown. Results are obtained using the wavefront gradient approach of the augmented model.

move along the x-axis through the focus. We notice that with 17 mW of power the peak values of the optical forces have increased by a factor of 1.7, relative to the same when the power was 10 mW. The slope of the optical force vs displacement plot at the trap center gives the value of the stiffness constant. Thus the increase in beam power also increases the respective stiffness constants.

We also use our proposed model to compute the optical force on the 2 μm bead using 17 mW of laser power as we change the NA of the objective lens. The plot of the z-component of the optical force against the displacement of the bead along the optical axis as seen in Fig. 2.12 (i) shows that for low NA values there is no equilibrium position and the equilibrium position appears only for larger NA values. Many optical systems use annular light beams where a circular opaque mask of a certain radius, say r_i is placed symmetrically in the entrance pupil of the lens. Figure 2.12 (ii) shows such an entrance pupil. We use our proposed model to compute optical forces using annular beams with normalized r_i having values 0.1, 0.2, 0.3, and 0.4. The power of the laser is kept at 17 mW while the 2 μm bead is moved through the focus along the x-axis. The plot of the x-component of the optical force against displacement as seen in

Fig. 2.12 (ii) indicates that as the radius of the circular mask increases the stiffness constants decreases.

2.5.2 Exact ray tracing approach of the augmented model

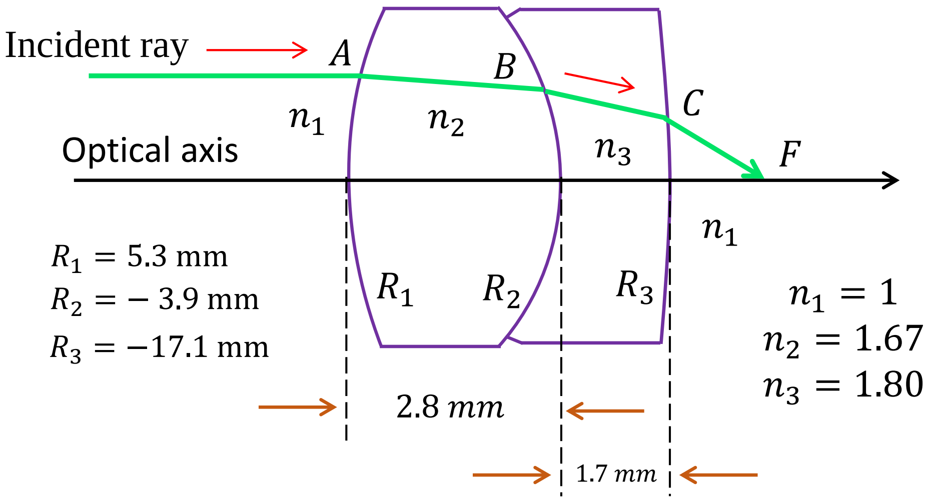

Fig. 2.13 Schematic diagram depicting a ray passing through a lens (make: Thorlabs, model: AC050-008-A-f = 7.5 mm).

To demonstrate the working of the exact ray tracing approach of the proposed model we consider a doublet lens system (make: Thorlabs, model: AC050-008-A-f = 7.5 mm). The schematic diagram of the lens is shown in Fig. 2.13. We consider the same Gaussian beam as above with a plane wavefront and compute optical forces again on a 2 μm bead. We then trace parallel rays through the lens surfaces starting from the entrance pupil after dividing the entrance pupil into 256 $\times$ 256 pixels. For each ray we obtain the coordinates (x_1, y_1, z_1) on the last surface of the lens and the direction cosines (l, m, n) in the image space. Figure 2.14 shows the paths of a few rays as each move from object side to image side. The x-component of the optical force is computed by displacing the bead along the x-axis through the focus.

Figure 2.15 (i) shows the plot of x-component of the optical force against displacement. It is seen that even with such a low NA lens there exist an attractive force towards the focus in the transverse direction. However, if we compute the axial component of the force as the bead is displaced along the optical axis, it is seen from Fig. 2.15 (ii) that due to the dominance of the

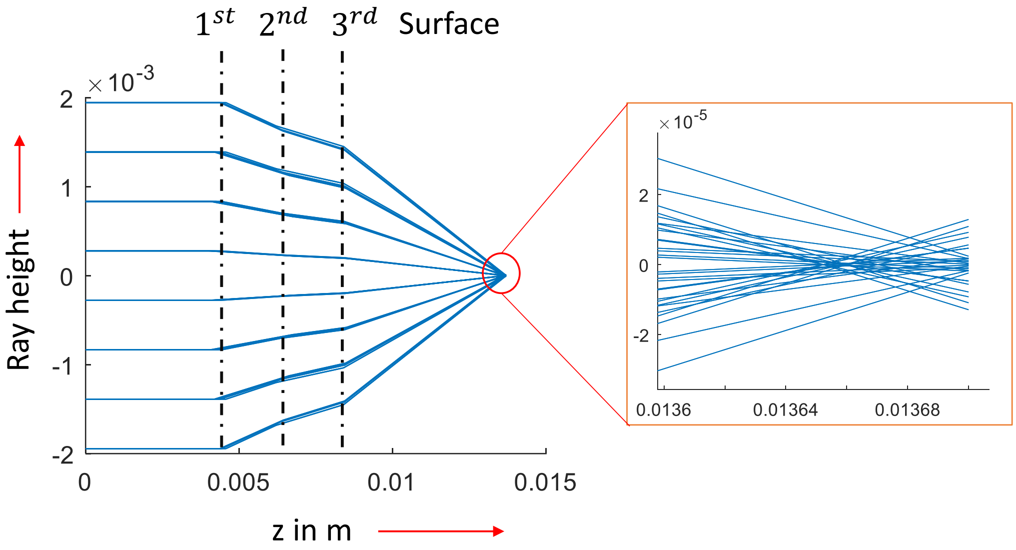

Fig. 2.14 Tracing of a bunch of collimated rays using the exact ray tracing method. The ray height and axial coordinate are expressed in meters. Inset shows that all the rays do not meet at the nominal focus.

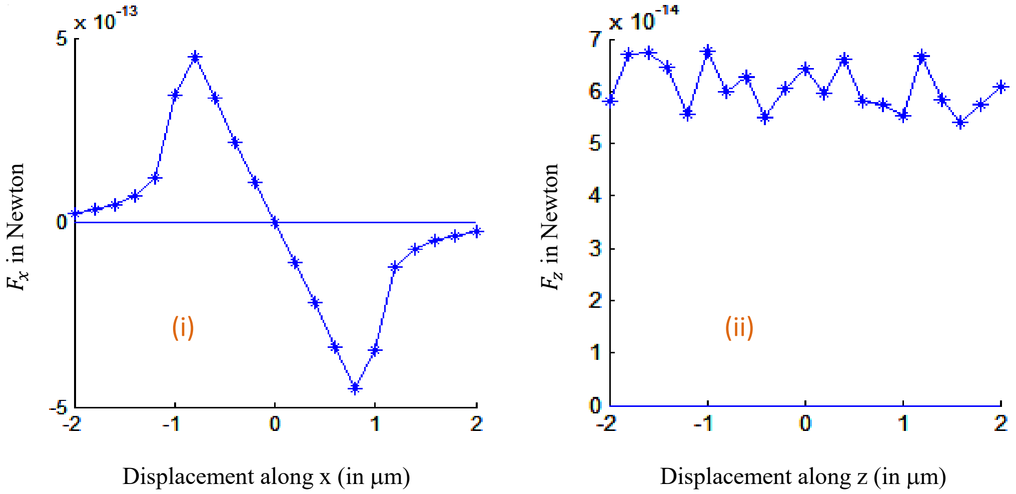

Fig. 2.15 Plots of (i) F_x vs displacement along x and (ii) F_z vs displacement along z for the 2 μm bead using the exact ray tracing approach of the augmented model.

scattering forces there is no appearance of equilibrium position.

2.6 Summary

In this chapter, we have briefly discussed various optical force calculation models while emphasizing more on the models in the ray-optics regime. Force calculation models in the ray-optics regime are particularly important for applications involving trapping of larger particles. We have described the ray-pencil model and how it can be implemented for Gaussian laser beams. We have then introduced an augmentation in the ray-pencil model so that the model can be applied for arbitrary beam profiles. We have demonstrated the working of the proposed model by comparing numerical simulation results with those using the existing ray-pencil model.

★ ★ ★

CHAPTER 3

Development of the Holographic Optical Tweezers

3.1 Introduction

In this thesis we implement a holographic optical tweezer based on a computer generated holography technique. In this chapter we therefore start with a discussion on the classical holography and the working principle of the computer generated holography technique. We then discuss how we can implement the binary computer generated holograms using a nematic liquid crystal spatial light modulator (NLCSLM). The chapter then discusses how the binary hologram implemented using an NLCSLM, can be used to move a laser beam in the sample plane and thereby construct an optical trap. We discuss the construction of the holographic optical trap and characterize its various parameters. Finally, we discuss some experimental results to demonstrate the working of the proposed HOT.

3.2 Principle of classical holography

Holography was first invented by D.Gabor in 1947 [65] for which he was later awarded the Nobel prize in Physics. Holography is a two-step process comprising recording of hologram and reconstruction of the object beam. Unlike photography, a hologram records the information of both intensity and phase of an object [66]. The name ‘hologram’ came from greek words ‘holos’ and ‘gramma’ whose meaning is ‘complete information’ [67]. The basic principle of holography is depicted in Fig.3.1.

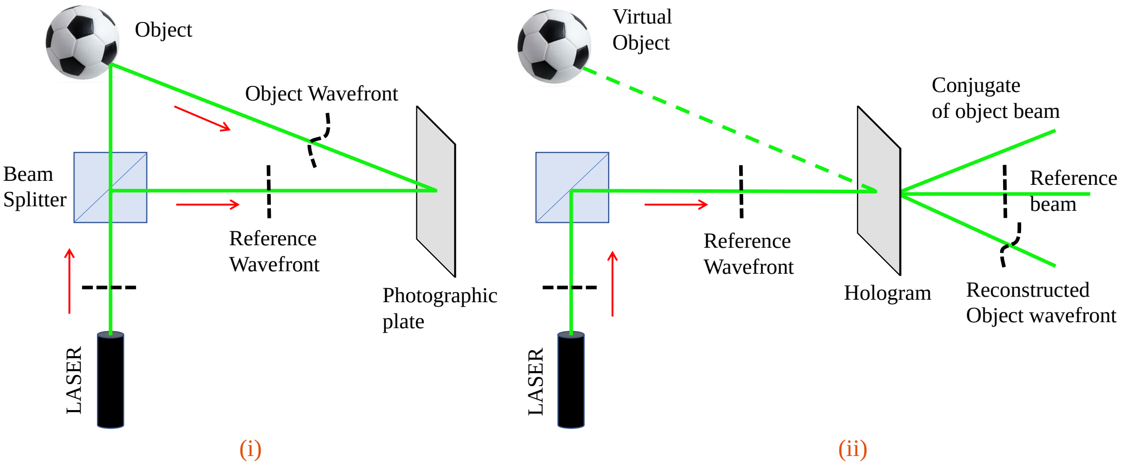

Fig. 3.1 Principle of classical holography. (i) Recording of the hologram and (ii) the reconstruction of object beam.

Recording of interference pattern

The first step of holography is the recording of the interference pattern that takes place between a plane reference beam and an object beam as seen in Fig. 3.1 (i). Two mutually coherent beams are generated from a single laser beam using a beam splitter (BS). One beam is the reference beam whose wavefront usually is plane and the other beam which gets reflected from the object is known as the object beam. The two respective wavefronts superimpose with each other constructively and destructively to form an interference pattern which is recorded on a photographic plate. This recorded photographic plate is known as hologram. The intensity distribution of the interference pattern is thus analogous to the transmittance function of the hologram.

Reconstruction of object beam wavefront

In the second step, the reconstruction of the complex amplitude profile of the object beam takes place. The recorded plate or hologram acts as a diffracting element for an incident beam. During reconstruction, as shown in Fig. 3.1 (ii), the hologram is illuminated by the same reference beam wavefront. The hologram diffracts the reference beam into three prominent diffraction orders. The object beam wavefront is realized in one of the diffracted beams. Among other two beams, the undiffracted beam is simply the reference beam and the third beam is the conjugate of the object beam whose complex amplitude is conjugate to that of the object beam. If one looks along the object beam a virtual image of the object is seen at the same place of the object even in the absence of the actual object as illustrated in Fig. 3.1 (ii).

Thus, using the classical holography principle, one can recreate any complex amplitude profile of the object beam by illuminating the respective hologram with a reference beam. The hologram needs to have a transmittance function proportional to the intensity distribution in the interference between the object beam and the reference beam, even in the absence of physical object to generate the object beam.

3.3 Computer generated holography

Computer generated holography (CGH) [68] uses the principle of classical holography to generate an object wavefront. As we have stated in the previous section, the mathematical description of the object beam and the reference beam is sufficient to calculate the interference pattern. The calculated interference pattern is then used to fabricate a hologram which has a transmittance function proportional to the intensity distribution in the interference pattern. Such a hologram is called computer generated hologram, which can be implemented using a light modulating device. The light modulation incorporated by a computer generated hologram can be either in analog or discrete. There is a certain type of computer generated hologram known as binary hologram where the light modulation has got two values. In this thesis we are going to use binary hologram in our experimental setup due to certain advantages of the hologram. There are several advantages of computer generated binary holography. Binary holography is advantageous, mainly because its implantation is simple and accurate. These holograms are easy to generate and can be realized on any light modulating device, such as spatial light modulator. Binary holograms can facilitate analog modulation of the amplitude and phase of light.

3.3.1 Construction of binary hologram

Let us consider $\Phi_{ob}(x,y)$ is the desired object beam phase and $\Phi_{ref}(x,y)$ is the phase function of the reference beam. (x,y) are the coordinates in the hologram plane defined over a unit circle $\sqrt{x^2+y^2} \leq 1$. Then the complex amplitude profile of the desired object beam will be

$$A_{ob}(x,y) = e^{i\Phi_{ob}(x,y)} \tag{3.1}$$

and that of reference beam will be

$$A_{ref}(x,y) = e^{i\Phi_{ref}(x,y)} \tag{3.2}$$

considering unit amplitude. Assuming these two beams are mutually coherent then the intensity distribution at the hologram plane will be

$$\begin{aligned} I &= |A_{ob}(x,y) + A_{ref}(x,y)|^2 \\ &= |e^{i\Phi_{ob}(x,y)} + e^{i\Phi_{ref}(x,y)}|^2 \\ &= 2[1+\cos(\Phi_{ob}(x,y) - \Phi_{ref}(x,y))] \end{aligned} \tag{3.3}$$

Thus the phase difference $\Phi(x,y) = (\Phi_{ob}(x,y) - \Phi_{ref}(x,y))$ as seen in Eq.3.3 lead to a co-sinusoidal variation in the intensity distribution [69]. Here we assume that the object beam and reference beam make some angle with one another and the tilt in the object beam is represented by $\tau(x,y) = t_x x + t_y y$. In most of the cases the reference beam is taken as a plane wavefront with its plane perpendicular to the direction of propagation, so that one can consider $\Phi_{ref}(x,y) = 0$.

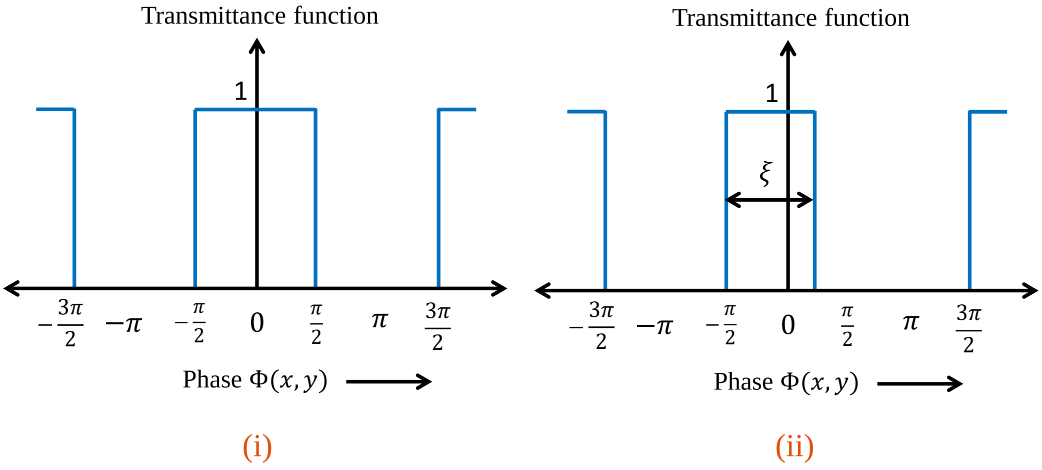

Fig. 3.2 Plots of binary hologram transmittance function vs phase Φ (modulo 2π -$\frac{\pi}{2}$) at a given location of the hologram plane, for (i) pure phase modulation, and (ii) phase and amplitude modulation.

Thus the overall phase of the object beam can be written as

$$\Phi_{ob}(x,y) = \phi(x,y) + \tau(x,y) = \Phi(x,y) \tag{3.4}$$

where $\phi(x,y)$ is a pure phase function defined with respect to a plane which is perpendicular to the propagation direction of object beam. The actual dependence of intensity in the interference pattern, on the object beam phase is given by Eq. 3.3. However, according to the algorithm to construct the binary hologram [70], the binarised transmittance function values in the hologram plane are given as

$$\mathbf{H}_{bh}(x,y) = \begin{cases} 1 & \text{for } \cos(\Phi(x,y)) \geq 0. \\ 0 & \text{otherwise.} \end{cases} \tag{3.5}$$

To understand the generation of the object beam wavefront in the diffracted beam from the binary hologram we consider the Fourier series analysis [71] of the transmittance function. The plot of the transmittance function $\mathbf{H}_{bh}(x,y)$ against the phase $\Phi(x,y)$ (i.e. 2π modulo of $\Phi(x,y)$ -$\frac{\pi}{2}$), which is a square wave is shown in Fig. 3.2 (i). So using the Fourier series of the square wave

$$\mathbf{H}_{bh}(x,y) = \frac{1}{2} + \frac{1}{\pi}\left[(e^{i\Phi}+e^{-i\Phi}) - \frac{1}{3}(e^{i3\Phi}+e^{-i3\Phi}) + \frac{1}{5}(e^{i5\Phi}+e^{-i5\Phi}) - .....\right] \tag{3.6}$$

In the above Fourier series the first term represents 0 order reference beam, while the terms with $e^{i\Phi}$ and $e^{-i\Phi}$ represent +1 and -1 diffraction orders, the terms with $e^{i3\Phi}$ and $e^{-i3\Phi}$ represent +3 and -3 orders and so on [72]. The diffraction orders such as ±1, ±3, ±5, ±7,.... contain the pure phase $\pm\phi$, $\pm3\phi$, $\pm5\phi$, $\pm7\phi$,..., propagate at relative angles given by $\pm\tau$, $\pm3\tau$, $\pm5\tau$, $\pm7\tau$,.... with respect to the undiffracted zero order and contain relative powers $\frac{1}{\pi^2}$, $\frac{1}{9\pi^2}$, $\frac{1}{25\pi^2}$, $\frac{1}{49\pi^2}$,.... respectively.

The diffraction pattern resulting from a binary hologram when a reference beam is incident on it can be obtained numerically by performing Fourier transform of the transmittance function representing the binary hologram.

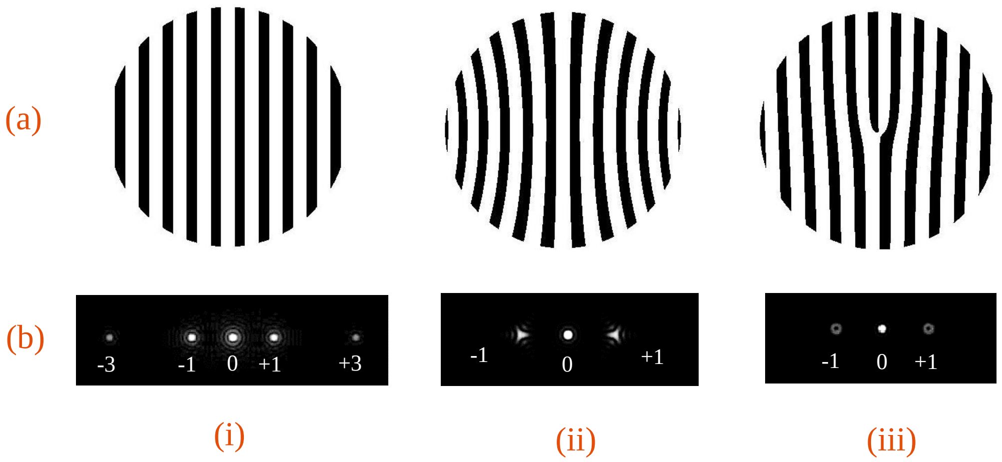

Fig. 3.3 (a) Binary holograms constructed using (i) $t_x = 14\pi$, $t_y = 0$, (ii) $t_x = 14\pi$, $t_y = 0$ and $\phi = Z_{10}$ and (iii) $t_x = 14\pi$, $t_y = 0$ and $\phi(x,y) = \theta$, where θ is the azimuthal angle. The corresponding computed diffraction patterns are shown in (b) (i)→(iii).

The +1 order is the most important of among all the diffraction orders as it carries the exact phase of the object beam and has the largest power. It has a diffraction efficiency of about 10%. The pure phase term $\phi(x,y)$ in Eq.3.4 can be used to incorporate any aberrations or vortex phase into the object beam. In our experimental work, aberrations are considered in terms of

Zernike circle polynomials [73]. So, the pure phase term can be written as $\phi(x,y) = \sum c_j \times Z_j$ where, c_j is the RMS (Root mean square) amplitude of j^{th} Zernike polynomial.

Figure 3.3 (a) shows binary holograms for an object beam with tilt values $t_x = 14\pi$, $t_y = 0$ and (i) $\phi(x,y) = 0$, (ii) $\phi(x,y) = Z_{10}$ (x-trefoil) and (iii) $\phi(x,y) = \theta$, where θ is the aziumuthal angle. The corresponding diffraction patterns are shown in Fig. 3.3 (b)(i)→(iii).

3.3.2 Amplitude modulation of the object beam using binary hologram

Previously, we have discussed about pure phase modulation of the object beam keeping its amplitude fixed as 1. However the modulation of the amplitude of the object beam [74] is important as one can then regulate the diffraction efficiency or the power of the object beam. Regulation of power is important even for optical trapping experiment. Now, we will discuss another feature of the binary hologram to modulate the amplitude profile of the object beam.

Let us consider that $a_{ob}(x,y)e^{i\Phi(x,y)}$ is the complex amplitude of the object beam. We then introduce a parameter ξ which in fact describes the binarised fringe width at (x,y), as seen in Fig. 3.2 (ii). It varies from 0 to π, such that when $\xi = \pi$ the plot becomes a square wave. The transmittance function of the binary hologram for both phase and amplitude modulation can be written as

$$\mathbf{H}_{bh}(x,y) = \begin{cases} 1 & \text{for } \Phi(x,y) < \xi(x,y) \\ 0 & \text{for } \Phi(x,y) \geq \xi(x,y) \end{cases} \tag{3.7}$$

Fourier series analysis of the hologram transmittance vs 2π modulo of the object beam phase plot at (x,y) can now be written as

$$\mathbf{H}_{bh}(\Phi) = a_0 + \sum_n a_n \cos(n\Phi) + \sum_n b_n \sin(n\Phi) \tag{3.8}$$

where, the coefficients a_n and b_n are given as

$$a_n = \frac{1}{n\pi}\left[\sin(-\frac{n\pi}{2} + n\xi) + \sin(\frac{n\pi}{2})\right] \tag{3.9}$$

and

$$b_n = 0 \tag{3.10}$$

Thus the coefficient of +1 order beam is

$$a_{+1} = \frac{1-\cos\xi}{2\pi} \tag{3.11}$$

Therefore the power in the +1 order beam is

$$\left(\frac{1-\cos\xi}{2\pi}\right)^2 = |a_{+1}|^2 = \frac{I}{\pi^2} \tag{3.12}$$

where, I is the normalised intensity in the +1 order object beam which also is the normalised power P in the beam. Hence for a given normalised power P in the +1 order beam, we need

$$\xi = \cos^{-1}\left(1-2\sqrt{P}\right) \tag{3.13}$$

The Eq. 3.13 is used in Eq. 3.7 to construct the binary hologram to regulate the power in the +1 order beam. For a given ξ the diffraction efficiency of the +1 order beam is $|a_{+1}|^2 = (\frac{\sin^2\frac{\xi}{2}}{\pi})^2$ × 100%. Hence the maximum obtainable diffraction efficiency remains $(\frac{1}{\pi})^2 \times$ 100%. If we want to generate a +1 order beam with complex amplitude $a_{ob}(x,y)e^{i\Phi(x,y)}$ we need to define $I = I(x,y) = |a_{ob}(x,y)|^2$ and hence ξ needs to be calculated for each (x,y) value.

3.4 Implementation of binary hologram using nematic liquid crystal spatial light modulator

Liquid crystal spatial light modulator (LCSLM) is an important device which uses the property of liquid crystal molecules to modulate the phase, amplitude and polarization of an incident light beam spatially [75]. An LCSLM consists of a 2D array of micron-sized cells or pixels. Each pixel of LCSLM contains liquid crystal molecules (LC molecules) that have physical properties between isotropic liquid and crystalline solid. The LC molecules are of ellipticalshaped with one long axis called director axis. The LCSLM devices normally use two types of LC molecules, nematic and smectic. In nematic phase, all the LC molecules in a cell are randomly positioned however they all tend to orient along a common direction. LCSLM consisting of nematic LC cell is called nematic LCSLM (NLCSLM).

A schematic diagram of a nematic LC cell is shown in Fig. 3.4. The cell comprises pair of glass plates, transparent conductors and alignment layers surrounding the LC molecules. In the case of 90° twisted cells the two alignment layers have scratch marks in two opposite directions called alignment directions. The LC molecules, which are close to the alignment layer, follow the direction of the scratch marks in the alignment layer to orient themselves. As a result the nematic molecules in the cell form a 90° twist in orientation from one alignment layer to the other as shown in Fig. 3.4 (ii), when no field is applied. If a laser beam is incident on the front surface of the LC cell and the polarization of the beam is parallel to the alignment direction of the front surface, then the beam comes from the other surface with its polarization rotated by 90°. Therefore if any analyzer, with its polarization axis parallel to the alignment direction of the front surface, is placed after the back surface, then the laser beam will not pass through the analyzer. However, if an appropriate AC electric field is applied between the two transparent conductors, then the LC molecules rotate themselves in the direction of the applied

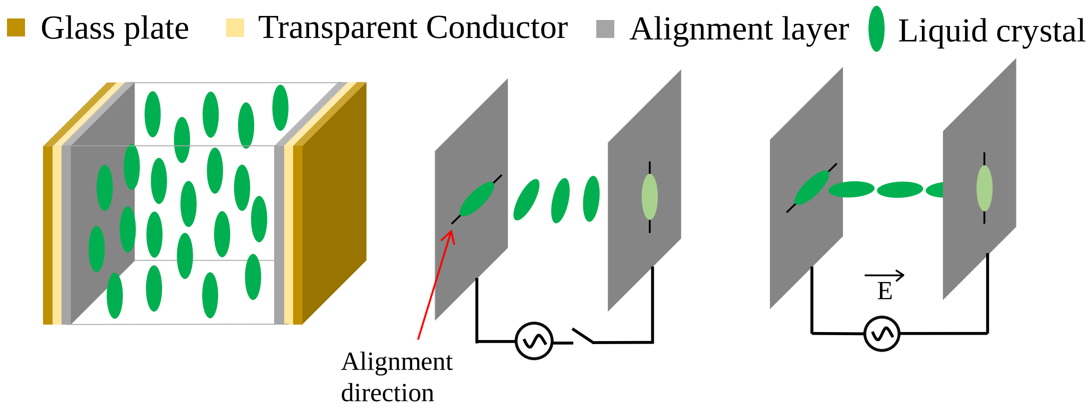

(i) (ii) (iii)

Fig. 3.4 Schematic diagram of (i) an LC cell with all molecules aligned vertically, of a 90° twisted nematic LC a cell, (ii) in the absence of electric field and (iii) in the presence of an AC electric field.

electric field as shown in Fig. 3.4 (iii). In this case the polarization of the laser beam will not rotate as it comes out from the back surface and thus will pass through the analyzer. This is the basic principle of modulating the amplitude of an incident laser beam by an LC cell with the help of external electric field.

In our experiments we use a 45° twisted NLCSLM (model LC-R 720, make HOLOEYE Photonics AG, Germany). This NLCSLM is based on the liquid crystal on silicon (LCoS) display technology and works in the reflection mode. The detail specifications of the NLCSLM are given in table 3.1.

Table 3.1 **Specification of the LC-R 720 NLCSLM.**

Display type	LCoS WXGA (Wide Extended Graphics Array)
Mode	Reflective type, 45° twisted nematic
Resolution	1280 H × 768 V
Pixel pitch	$20 \times 20\ \mu$m
Gray levels	8-bit (256)
Frame rate (Maximum)	180 Hz
Operating voltage	24V DC

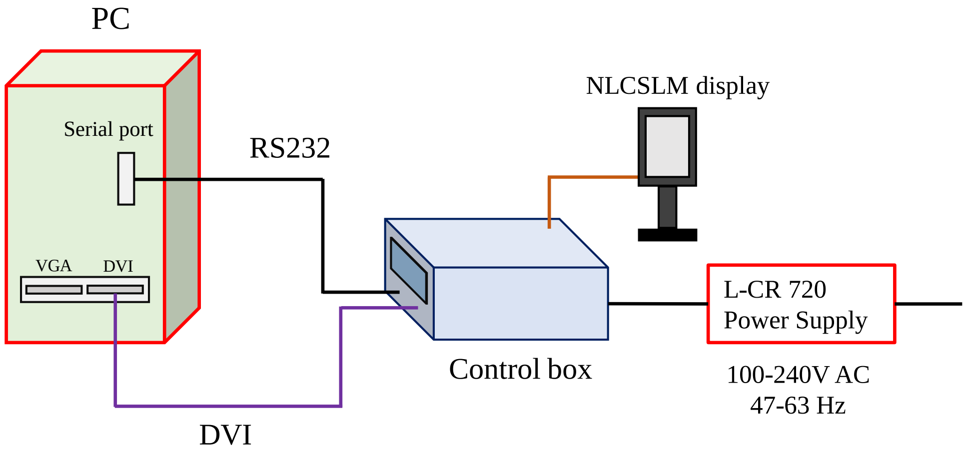

Fig. 3.5 Schematic diagram showing the connections between PC, the synchronization unit and the NLCSLM.

The NLCSLM can be addressed using a PC where user defined external field values can be applied individually to each LC cell of the device. Figure 3.5 shows the connections between the NLCSLM and PC via which one can address the NLCSLM display. The device can display 8 bit image patterns at a rate of 180 Hz sent by user as DVI output. The external electric field applied to a given cell is determined by the 8 bit pixel value at the analogous location of the image being sent to the display panel. Therefore the computed binary hologram can simply be sent to the NLCSLM as DVI data to make the device work as binary amplitude hologram. A RS232 communication can be optionally used to configure the display properties of the NLCSLM.

3.5 Holographic optical tweezer

Holographic optical tweezer (HOT) uses holographic technique to control and manipulate microscopic particles in an optical trap. In 2002 Curtis et al. first came up with the term 'holographic optical tweezers' in their work of holographic trapping using spatial light modulators [76]. Holographic control of the trapping beam has many advantages and the technique has found important applications such as manipulation of micro [77] and nano particles [78], study of cells structure [79] etc. The key feature of HOT is the control over more than one trapping beam using diffractive optical element like SLM [80].

3.5.1 Use of binary hologram for programmable beam control

As discussed already the computer generated binary hologram can control the phase and amplitude of the +1 diffracted order beam. In addition the CGH technique can also be utilized to move the +1 order beam according to the spatial frequency of the grating pattern in the binary holograms. The spatial frequency of the hologram depends on the tilt values (t_x and t_y). In accordance with the change in the tilt values the distance between the undiffracted 0 order [81] and +1 order changes. Therefore one can move the +1 order beam with respect to 0 order by changing the tilts (t_x and t_y) of the hologram. Figures 3.6 (i) (a) and (b) show two binary holograms constructed with different tilt values. The resulting diffraction pattern seen in Fig.

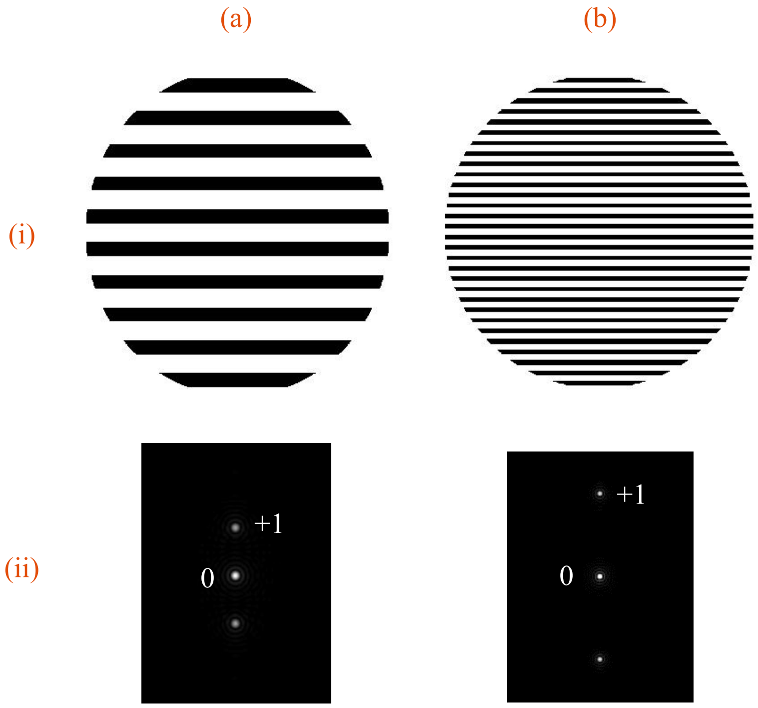

Fig. 3.6 (i) Binary holograms with different tilt values and (ii) the resulting diffraction patterns showing separation of the +1 order with respect to the 0 order.

3.6 (ii) shows that the +1 order beam moves relative to the 0 order beam when the tilt values are increased. A basic experimental setup for holographic beam control is shown in Fig. 3.7. An expanded and collimated laser beam falls on a binary hologram which is implemented on an NLCSLM. The hologram diffracts the incident laser into a number of orders. Lens L_3 collects the diffracted orders and focuses onto a pinhole. The pinhole isolates the +1 order beam from others and the isolated beam gets expanded and collimated by lens L_4. The collimated beam is then focused by the objective lens onto the sample plane. Here, the lenses L_3 and L_4 are arranged to form a 4f relay system so that the hologram or the NLCSLM plane is optically conjugate to the back focal plane of the objective lens. Being the conjugate plane any change in the hologram plane will be reflected identically at the back focal plane of the objective lens. Therefore as the tilt values in the hologram displayed on the NLCSLM changes the +1 order beam focused in the sample plane moves accordingly. The relative shift of the +1 order in the

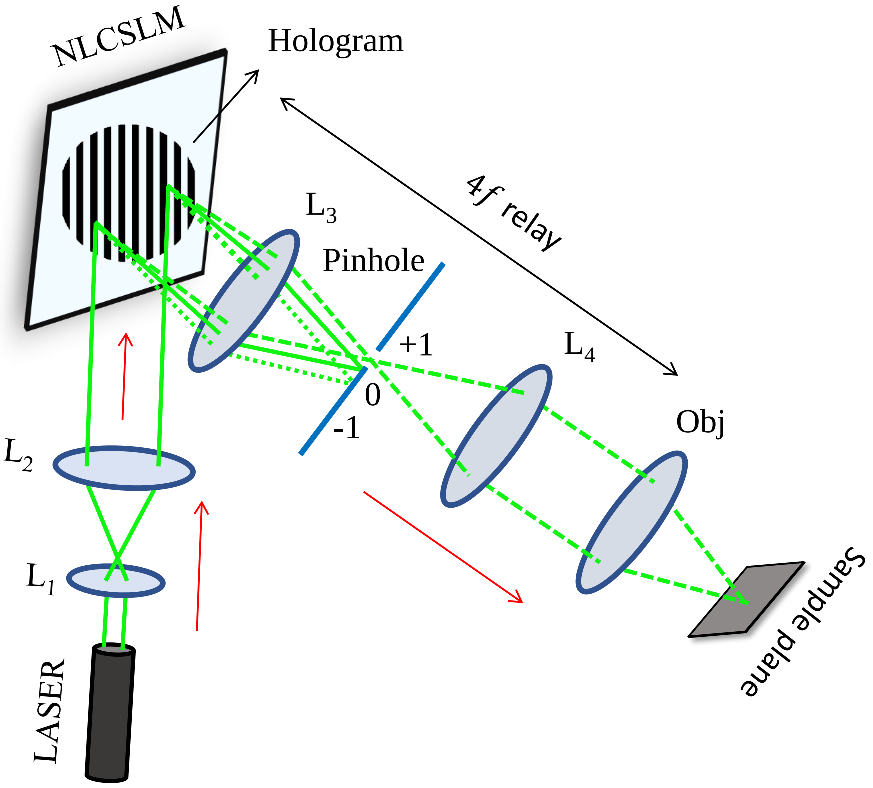

Fig. 3.7 A basic experimental setup to obtain the user-defined +1 order beam at the sample plane.

sample plane is decided by the following Equation,

$$\Delta x = f \times \tan\theta = m \frac{f\lambda \times \sqrt{\Delta t_x^2 + \Delta t_y^2}}{d} \tag{3.14}$$

where, f is the focal length of objective lens, θ is the change of beam angle due to the change in tilt, λ is the wavelength of light, Δt_x and Δt_y are the changes in tilt values of the hologram and d is the size of hologram. The transverse magnification between the hologram plane and the back focal plane of the objective is given by m.

In a trapping experiment the size of the beam at the back aperture of the objective lens is also important, since the beam needs to cover the entire aperture. If the beam underfills the aperture then the effective numerical aperture of the objective will be less than the prescribed value. The size of the hologram as defined on the display panel decides the size of +1 order diffracted beam in the back aperture. The hologram size can be modified by incorporating a digital mask to the hologram (which will be discussed in the subsequent section). In addition it is also important to choose the focal lengths of lenses L_3 and L_4 properly for correct transverse magnification between the hologram plane and the back focal plane of the objective lens.

3.5.2 Basic components of the experimental arrangement

The experimental arrangement to implement the holographic optical tweezer comprises several important components in addition to the NLCSLM assembly to realise binary holograms discussed already. Below we are going to describe some of the other important components of the setup.

(i) DPSS laser

The laser is one of the most important components for a holographic tweezer. For the trapping experiment, the laser should ideally produce light of single mode (TEM_{00}- Gaussian mode), with low power fluctuations and high pointing stability. In addition, a smaller beam waist, uniform spatial mode profile, and narrow laser bandwidth are also important. In our work we use a diode-pumped solid state (DPSS) laser of wavelength 532 nm with an output power 1.1 W. The detailed specifications of the laser is given in table 3.2.

(ii) The microscope objective

The microscope objective lens is another crucial element of the optical trapping arrangement. High numerical aperture (NA = 1.2 to 1.4) objective lenses create strongly focused beam to trap small particles. For our trapping experiment we use primarily two high NA lenses UPlanSApo100XO (Olympus) and UPlanSApo60XW (Olympus). Both the lenses are super-apochromat type. Hence they are corrected for chromatic and spherical aberrations. Besides they have a very high transmission from visible to near IR range. In addition to the two high NA lenses we also use a low NA lens UPlanFLN10X2 (Olympus) for checking the beam alignment and for characterizing the beam forming optics. The specifications of the three lenses are presented in table 3.3.

Table 3.2 **Specifications of the DPSS laser.**

Model no.	MLL-FN-532nm-1W-13100726
Technology	DPSS
Output power	1.1 W
Wavelength	532 nm
Power stability	0.200%
Operating mode	CW
Transverse mode	TEM_{00}
Beam diameter ($\frac{1}{e^2}$)	1.2 mm
Beam divergence (Full angle)	1 mrad
Beam quality (M^2)	1.169
Warm-up Time	<10mins

Table 3.3 **Specifications of the microscope objectives.**

Manufacturer	**NA**	**Magnification**	**Immersion media**	**Working distance**	**Correction level**
UPlanSApo100XO	1.4	100×	Oil	0.13 mm	Super-apochromat
UPlanSApo60XW	1.2	60×	Water	0.28 mm	Super-apochromat
UPlanFLN10X2	0.30	10×	Air	10 mm	Semi-apochromat

(iii) CMOS camera

In an optical trapping experiment observations of the beam and the trapped beads are done with a camera. In this thesis we use two complementary metal oxide semiconductor (CMOS) cameras, namely, USB 3.0 CMOS (Thorlab, DCC3240) and another is FLIR (GS3-U3-23S6M). Detail specifications of these cameras are given in table 3.4.

(iv) Synchronization unit

The dynamic holographic beam movement and corresponding image acquisition of beam or the bead require synchronisation between hologram display and camera acquisition. For this

Table 3.4 **Specifications of the cameras.**

Camera Model No.	Thorlab: DCC3240	FLIR: GS3-U3-23S6M
Sensor type	CMOS	CMOS
Resolution	1280×1024	1920×1200
Pixel pitch	5.3 μm	5.86 μm
Frame rate	60 fps	163 fps
Interface	USB 3.0	USB 3.1

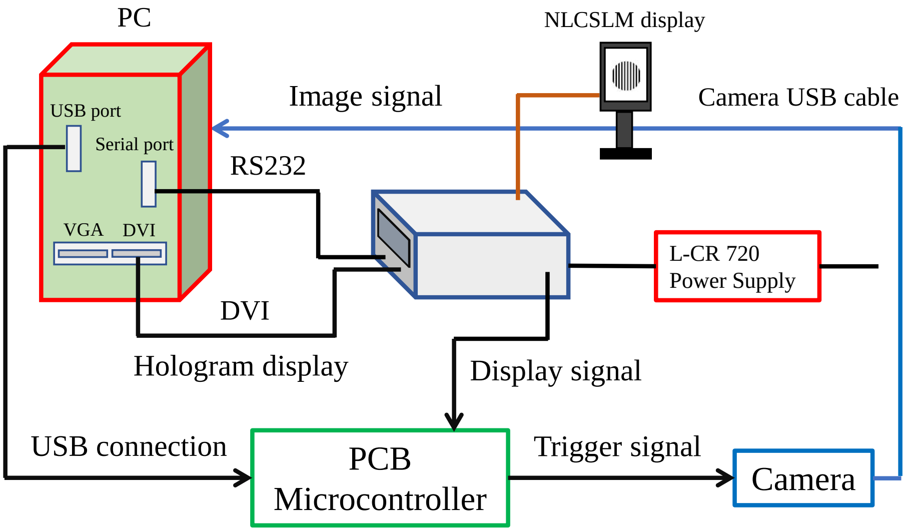

Fig. 3.8 Schematic diagram of the synchronization assembly consisting of the PC, NLCSLM, PIC Microcontroller board and the camera.

purpose we develop a synchronization unit using a PIC18F2550 microcontroller (Microchip technology) which has 28 input/output pins for different functions. Figure 3.8 shows the schematic diagram of the synchronisation operation. The microcontroller board is connected to the PC via USB communication. The NLCSLM provides a TTL sync signal which goes to the PIC microcontroller as an interrupt. The microcontroller is programmed to generate trigger signals for synchronised image acquisition by the camera. Figure 3.9 presents an oscilloscope screen shot showing the the NLCSLM sync signal and a typical trigger signal for the camera with a time interval between two acquisition as 50 msec.

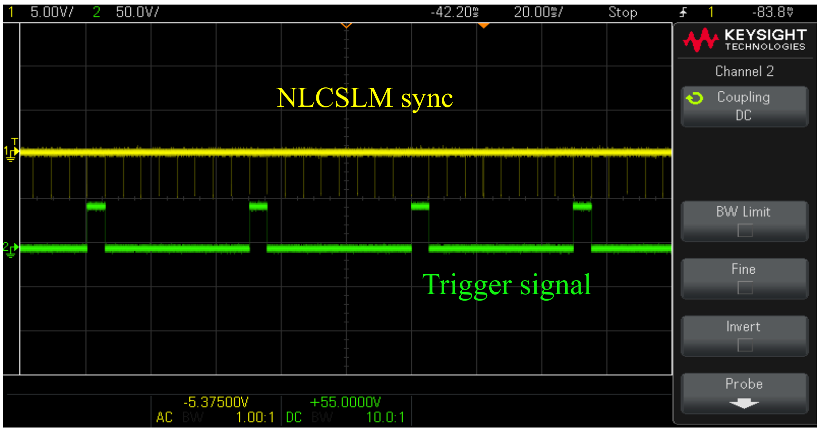

Fig. 3.9 Screen shot from digital oscilloscope showing the sync signal from NLCSLM and the generated camera trigger signal.

(v) Bead sample preparation

In our proof of principle experiment using the HOT we are going to trap latex and silica beads of different sizes. Normally these beads are available in a dense colloidal solution and hence to use them in a trapping experiment specimen slides are to be prepared. We use raw sample of silica beads from Bangs Laboratories, Inc.(P/N SS04N/9857) and latex beads from Sigma Aldrich. It requires a number of items, namely, microscope slide, glass cover slip, double-sided tape, micro-pipete, pipete tips, Kim wipes, nail polish, ethanol, distilled water and a vortex mixer, during the preparation. Below step by step sample preparation procedure is described.

Important steps:

Step 1: First we clean the microscope slide and glass cover slip properly using ethanol. This removes the unwanted dirt and oil from the glass surface.

Step 2: We then place two small double sided tapes at the middle of the microscope slide at 3-4 mm separation. This creates a sufficient channel for the movement of sample beads.

Step 3: Preparation of 1:10000 diluted solution: We first shake the raw bead solution properly to distribute the beads thoroughly in the solution. We take 1 μl of raw bead sample and mix with 99 μl distilled water. This makes the solution of dilution 1:100. Now, from this stock

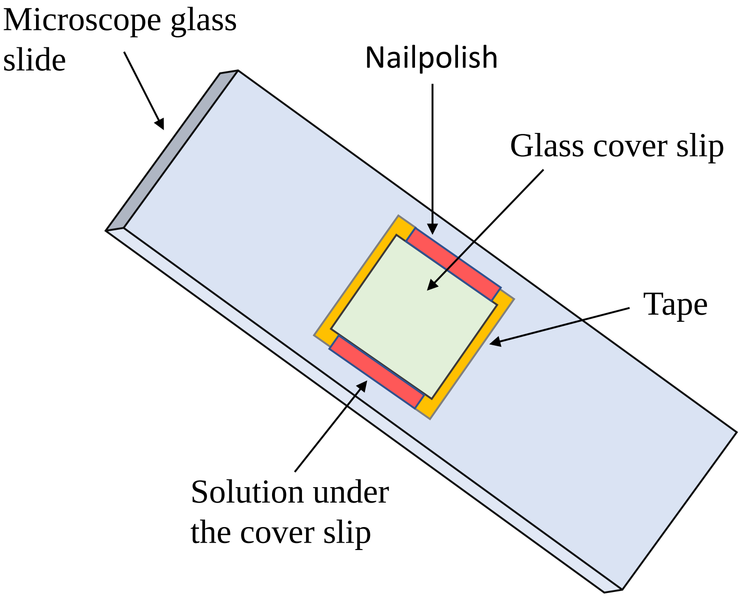

Fig. 3.10 Diagram of microscope slide and cover slip which enclose the sample solution.

solution we take 1 μl solution and again mix with 99 μl distilled water. This prepares the sample solution of dilution 1:10000. After every mixing we shake the solution properly using the vortex mixer to distribute the beads all over the prepared solution. We dilute the sample properly so that during trapping of single particle, other particles do not come close to the trapping position.

Step 4: Then we take 15-20 μl of prepared solution and place it at the channel between two double-sided tape.

Step 5: We then place the glass cover slip on top of the double-sided tape so that the solution stay in the channel in between glass slide and cover slip.

Step 6: We seal the open ends of the channel by applying nail polish to prevent the drainage of solution.

A diagram of microscope glass slide and cover slip enclosing the prepared bead solution is shown in Fig. 3.10.

3.5.3 Characterization and assessment of the holographic optical trap setup

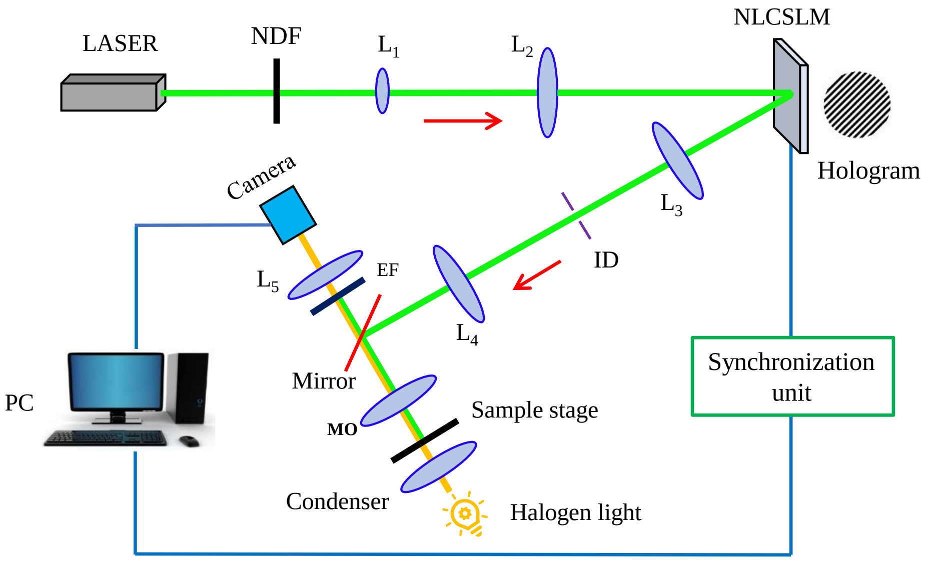

Fig. 3.11 Experimental arrangement of the dynamic holographic optical trap setup. The hologram is described over 256×256 pixels so that the beam overfills the entrance pupil of the 1.4 NA objective lens.

We build upon the holographic beam control setup to realise the experiment arrangement of the holographic optical tweezer. Figure 3.11 shows the schematic diagram of the experimental arrangement. The binary hologram based beam forming assembly is same as that shown in Fig. 3.7. Here we use the DPSS laser of output power 1.1 W emitting at wavelength 532 nm as the laser source. We can optionally use a neutral density filter (NDF) just after the laser to regulate the incident laser power. The microscope objective and the specimen stage are part of an Olympus inverted microscope (IX51) (Not shown in the figure). A dichroic mirror is used between lens L_4 and the microscope objective (MO) so that the 532 nm beam from the laser is reflected towards the sample plane. To observe the beads we use light from a halogen lamp which illuminates the sample plane with the help of a condenser lens. Light transmitted by the sample plane is collected by the MO and is then transmitted by the dichroic mirror and an emission filter to be finally focused onto the camera by lens L_5. Camera thus images the sample plane using long wavelength light from the halogen lamp.

Before going to the actual trapping experiment we perform some preliminary experiments to characterize the holographic optical trap setup.

(a) Beam movement with uniform and accelerated step size

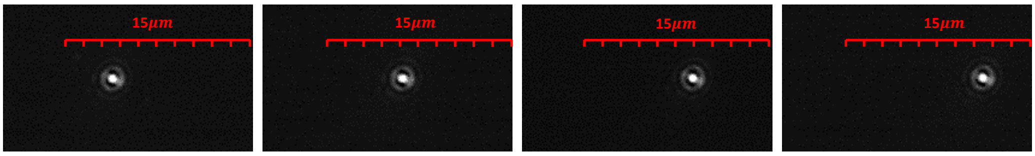

(i) (ii) (iii) (iv)

Fig. 3.12 Experimental images of consecutive beam positions in the sample plane with step size equal to 1.5 μm. The markings of the scale bar in each image have interval equal to 1.5 μm.

We have so far discussed how using the binary hologram based assembly we can move the +1 order beam to different locations in the sample plane. First we show that the +1 order beam can be moved in the sample plane with equal or uniform step size. We construct a series of holograms with uniformly increasing tilt values and display them sequentially on the NLCSLM at an interval of 100 msec. The increment in tilt is chosen to move the +1 order beam by 1.5 μm in the sample plane using the 100X lens after each hologram update. Figure 3.12 shows the experimental images of consecutive beam positions in the sample plane. We locate the beam center from each experimental image and then estimate the step size of the actual beam as the holograms are updated. If Δp_x is the number of camera pixels between two consecutive beam positions, then the estimated step size = $\Delta p_x \times$ (camera pixel pitch)/(magnification of objective lens). Table 3.5 shows the estimated step size for the horizontal beam movement obtained from the experimental images. We observe that the estimated step size $\approx$ 1.5 μm.

We then construct binary holograms to provide non uniform or accelerated step sizes to the +1 order beam. Holograms are designed to increase the step size by 0.5 μm after each step. Figure 3.13 shows the experimental images of the accelerated beam positions.

Table 3.5 **Estimated step size of the beam in the sample plane with change of tilt values in the hologram.**

Serial no. of positions	**Tilts in hologram** (t_x , t_y)	**Position of beam (camera pixel index)** (x , y)	**Estimated step size in pixels** (Δp_x)	**Estimated step size in** μ**m**
1	$(76.2873\pi , 110.398\pi)$	(704 , 478)		
2	$(81.8765\pi , 105.137\pi)$	(679 , 479)	25	1.456
3	$(87.4656\pi , 99.8771\pi)$	(653 , 479)	26	1.523
4	$(93.0547\pi , 94.6167\pi)$	(628 , 479)	25	1.456

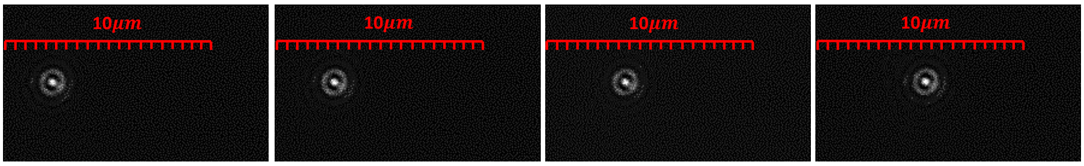

(i) (ii) (iii) (iv)

Fig. 3.13 Experimental images of accelerated beam positions in the sample plane. The markings of the scale bar in each image are of interval equal to 0.5 μm.

Table 3.6 **Estimated step size of the accelerated beam in the sample plane.**

Serial no. of position	**Tilts in hologram** (t_x , t_y)	**Position of beam (camera plane index)** (x , y)	**Estimated step size in pixels** (Δp_x)	**Estimated step size in** μ**m**
1	$(104.233\pi , 84.096\pi)$	(568 , 472)		
2	$(102.37\pi , 85.8495\pi)$	(578 , 472)	10	0.586
3	$(98.6439\pi , 89.3564\pi)$	(595 , 472)	17	0.996
4	$(93.0547\pi , 94.6167\pi)$	(619 , 471)	24	1.406

The experimental images are then used to estimate the step sizes of the beam movement. Table 3.6 shows that using our setup we are also able to move the +1 order beam with non uniform step size upto a reasonable accuracy.

(b) Programmable control of diffraction efficiency

We have already discussed the generation of binary holograms to modulate the amplitude of the +1 order diffracted beam. We use the parameter ξ whose expression is given by Eq.3.13, during the construction of binary holograms. Dynamic control of power of the +1 order diffracted beam, i.e. the diffraction efficiency, is very much advantageous in a trapping experiment to understand the effect of variation in beam power. We construct and display holograms and measure the power in the +1 order beam at the back aperture of the 100X objective lens using a photometer. We make the power measurements once placing an ND filter after the laser and once without the ND filter. Table 3.7 shows measured values of power in the incident beam and the +1 order diffracted beam and the respective diffraction efficiencies. The power of laser is 1.1 W before the ND filter. The laser power incident on the NLCSLM is 118 mW in the case of neutral density filter (NDF) of 0.4 optical density (OD) after the laser and 211 mW without any ND filter. From the table 3.7 we see that for ξ = 1 we get the maximum diffraction efficiency

Table 3.7 **Experimental measurement of diffraction efficiency.**

Parameter ξ	**Power in the +1 order beam**		**Diffraction efficiency**	
	NDF = 0.4 OD	No NDF	NDF = 0.4 OD	No NDF
1	10.55 mW	18.92 mW	8.94 %	8.96 %
0.9	9.76 mW	17.65 mW	8.27 %	8.36 %
0.8	9.15 mW	16.49 mW	7.75 %	7.81 %
0.7	8.53 mW	15.50 mW	7.22 %	7.34 %
0.6	7.56 mW	13.98 mW	6.40 %	6.62 %
0.5	7.19 mW	12.89 mW	6.09 %	6.10 %
0.4	6.49 mW	11.68 mW	5.5 %	5.53 %
0.3	5.26 mW	9.84 mW	4.45 %	4.66 %
0.2	4.19 mW	8.15 mW	3.55 %	3.86 %
0.1	2.98 mW	5.79 mW	2.52 %	2.74 %
0	25.63 μW	45.65 μW	0.02 %	0.02 %

≈ 8.9 % which is very close to the theoretical limit of 10 %. In our experiments discussed in the next chapter we keep construct binary holograms using $\xi = 1$.

(c) Programmable control of the entrance pupil

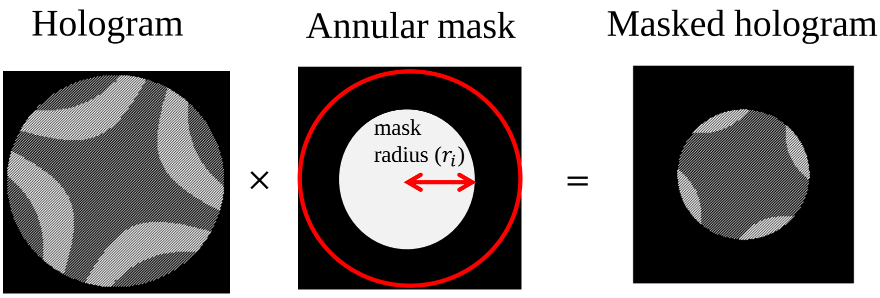

Fig. 3.14 Multiplication of a given hologram with an annular mask with inner radius r_i.

Each hologram after construction can be multiplied with an annular mask with inner circle having pixel value 1 and the annular part having pixel value 0. This multiplication changes the effective size of the hologram as shown in Fig. 3.14.

As we vary the radius of the inner circle (mask radius), the radius of the beam at the back aperture of the objective lens also changes. This in turn changes the effective numerical aperture of the objective lens and also net power in the beam in the sample plane. We have

$$FWHM = \frac{0.5\lambda}{NA} \tag{3.15}$$

where FWHM is the full width at half maximum [82] of the +1 order focal spot in the sample plane and NA is the effective numerical aperture of the objective. Thus as the mask radius is varied the FWHM of the beam in the sample plane also changes. Table3.8 shows the experimentally measured FWHM of beam spot with respect to the mask radius using the 100X objective lens. It is seen that the FWHM value increases with the decrease of mask radius (or hologram size) as the effective NA of the lens also decreases. In addition to the change in the FWHM, the mask radius also effects the power in the beam. The measurement of power in the

Table 3.8 **Mask radius vs FWHM of the beam in the sample plane.**

Mask radius (normalized value)	**FWHM of beam (nm)**
1	330.26
0.9	330.65
0.8	330.98
0.7	331.96
0.6	337.16
0.5	433.61
0.4	516.55
0.3	651.23
0.2	932.16
0.1	1885.63

Table 3.9 **Mask radius vs power of the beam.**

Mask radius	**Beam power**	
(normalized value)	NDF = 0.4 OD	No NDF
1	10.35 mW	18.56 mW
0.9	8.84 mW	16.69 mW
0.8	6.89 mW	15.25 mW
0.7	5.45 mW	11.78 mW
0.6	4.13 mW	8.89 mW
0.5	3.6 mW	6.56 mW
0.4	2.1 mW	4.02 mW
0.3	1.162 mW	2.48 mW
0.2	561.2 μW	1.36 mW
0.1	192.05 μW	330.26 μW

+1 order beam (at the back focal plane of the objective lens) with respect to the mask radius is shown in table 3.9.

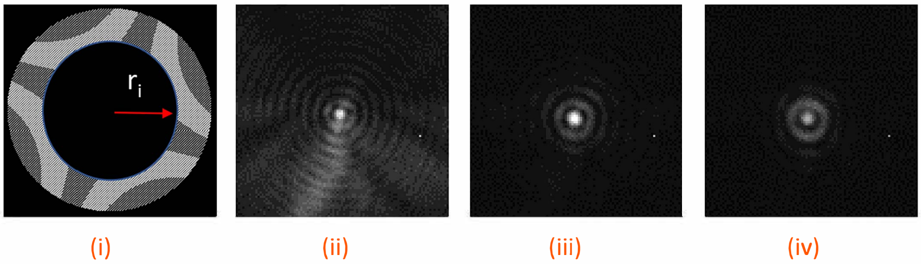

Fig. 3.15 (i) An annular mask comprising inner circular disc of radius r_i with pixel value 0 and the annular part with pixel value 1, which multiplies the binary hologram. (ii → iv) show the experimental images of the +1 order focal spots using the 1.4 NA objective lens, corresponding to $r_i = 0.5$, 0.3 and 0.1, respectively.

We can also employ a reverse of the annular mask seen in Fig. 3.14 to generate annular illumination beam. Figure 3.15 (i) shows such an annular mask comprising inner circular disc of radius r_i with pixel value 0 and the annular part with pixel value 1, applied on the binary hologram. Figures 3.15 (ii → iv) show the experimental images of the +1 order focal spots using the 1.4 NA objective lens, corresponding to $r_i = 0.5$, 0.3 and 0.1, respectively. We can see as r_i increases the size of the inner disc in the focal spot decreases, however there appears stronger sidelobes.

(d) Trapping of beads with different objective lenses

We then assess the capability of our setup to trap beads of different sizes. We use both the 100× and 60× objective lenses to perform the trapping. We first focus the +1 order beam at a random location in the sample solution. The sample stage is then moved in x-y directions to bring a single bead closer to the focal spot. After a particle gets trapped, we then move the trapped bead by moving the +1 order beam holographically. Figures 3.16 (a)(i)→(iii) show the trapping and horizontal movement of a 3 μm diameter latex bead using the 100X objective lens. Here the power of the trapping beam is around 17 mW in the entrance pupil. Figures 3.16 (b)(i)→(iii) show trapping and diagonal movement of a 2 μm diameter silica bead using the 60X objective lens. In this case the amount of power in the entrance pupil is around 10 mW.

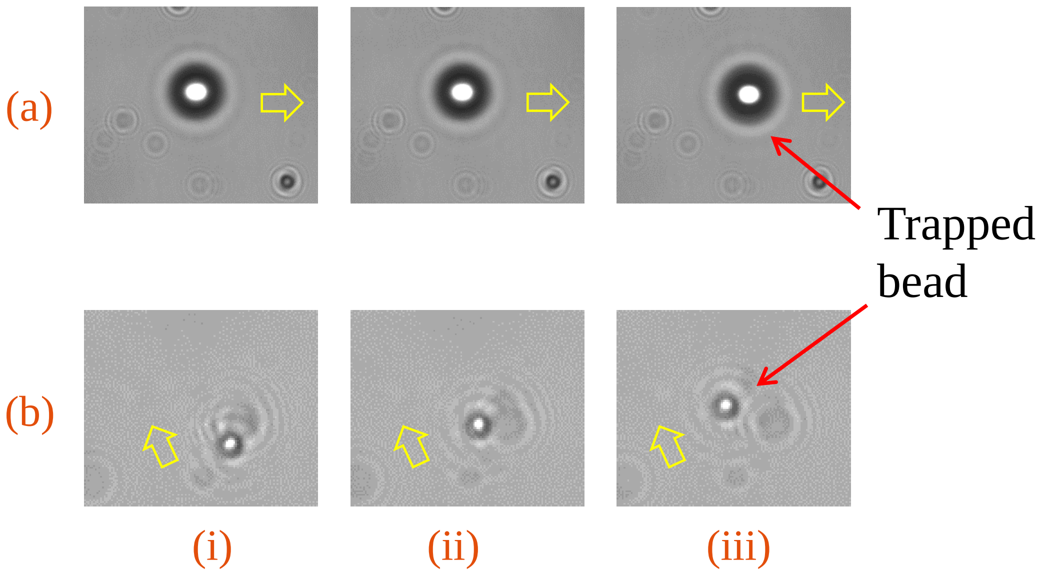

Fig. 3.16 Experimental images of trapped beads. Trapping and movement of (a) (i)→(iii) 3μm (diameter) latex bead and (b) (i)→(iii) of 2 μm (diameter) Silica bead.

3.6 Summary

In this chapter, we have discussed the principle of classical holography and extended the concept to discuss computer generated holography. We have then discussed the construction of binary hologram to modulate the complex amplitude of the +1 order diffracted beam and implementation of the same using an NLCSLM. This is followed by a discussion on the experimental arrangement to implement the holographic optical trap. We have then presented experimental results to demonstrate the performance of various features of our experimental arrangement. We have ended the chapter with a demonstration of trapping and movement of beads using two different objective lenses.

★ ★ ★

CHAPTER 4

Experimental validation of the augmented ray-pencil model

4.1 Introduction

This chapter presents the experimental validation of the theoretical results of the proposed augmented force calculation model for optical trapping using our dynamic holographic optical tweezer setup. The chapter starts with the discussion on measurement methods of optical force and trap-stiffness which can be implemented using our setup. It then presents experimental results of uniform speed and acceleration of trapped beads in water medium achieved with our setup. Afterwards the chapter discusses the experimental validation of trap stiffness, maximum force or escape force, and range of optical force. We end this chapter by a comparison of experimental results with numerical simulation results using vortex beams for trapping.

4.2 Experimental techniques to measure the optical trapping force

It is already discussed that optical tweezer is a technique to realize pico-Newton level small forces to trap and move a microscopic particle in a liquid medium. The complete trapping system behaves like a harmonic potential well and the particle gets trapped in the minimum potential energy region. Figures 4.1 (i) and (ii) show the trapped particle in two different positions of the harmonic potential well. In one dimension the potential energy of the particle is defined as $U(x_1) = \frac{1}{2}kx_1^2$, where k is the harmonic constant and x_1 is the position of the particle from equilibrium position (i.e. trap centre). Thus the force is linearly dependent on the position (x_1) of the particle. In order to measure this force it is important to know the displacement of the particle from equilibrium position [83].

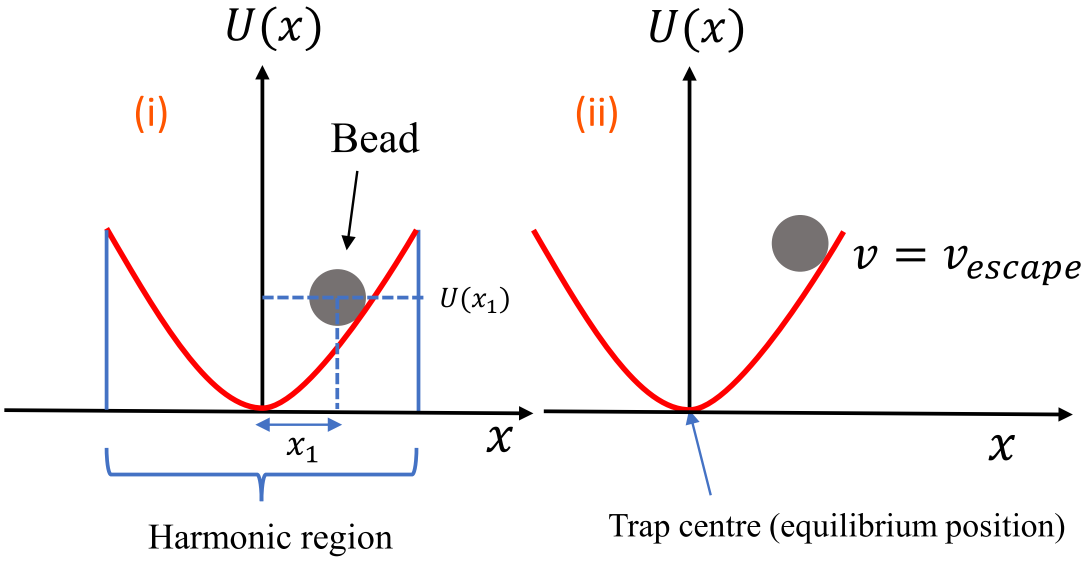

Fig. 4.1 Trapped particle in harmonic potential well $U(x)$.

There are several methods that can be followed for the experimental measurement of trapping forces. These are drag force method, escape force method, equipartition method, power spectrum and step response method. However, we will discuss below two of these methods which are used in this work.

4.2.1 Drag force method

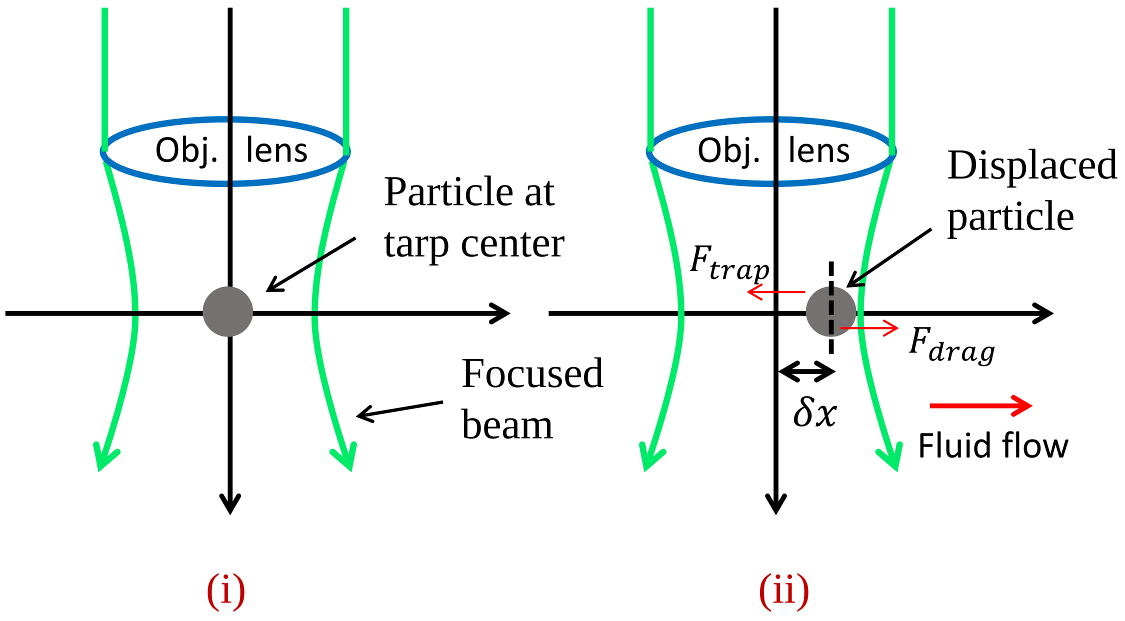

Fig. 4.2 Illustrative diagram of two different positions of trapped particle. (i) is showing the trapped particle at the center of the trap and (ii) shows the displaced particle from the trap center due to fluid flow in the direction showed in the figure.

Drag force method is one of the important methods to estimate optical force when the particle is displaced from the trap center [84]. The displacement of the particle can be done in two ways, one is by moving the translation stage relative to the fixed focused beam and the other is by moving the focused trapping beam relative to the stage. In both cases, the displaced particle in the fluid medium feels a viscous drag force that opposes the relative movement of the particle [85]. The viscous drag force on the particle follows Stokes' law [86], hence when the trapping force is balanced by the drag force, we have

$$F_{drag} = 6\pi\eta a v = F_{trap} \tag{4.1}$$

where, F_{drag} is the viscous drag force that acts on the particle in fluid medium, η is the viscosity of the fluid, a is radius of the particle and v is the flow velocity relative to the particle. If, in equilibrium, the displacement of the particle is δx, from the trap center as shown in Fig. 4.2

(ii), then the trapping force is

$$\begin{aligned} F_{trap} &\propto \delta x \\ &= \kappa \delta x \end{aligned} \tag{4.2}$$

where, κ is the stiffness constant that characterizes the trapping force. So, from Eq. 4.1 and Eq. 4.2 we have

$$\kappa = \frac{6\pi\eta a v}{\delta x} \tag{4.3}$$

Thus one can employ the drag force method to measure the trapping force and trap stiffness constant experimentally.

4.2.2 Escape force method

In escape force method, the same technique as the drag force method is followed to measure the trapping force corresponding to the displacement when the particle escapes from the trap [87]. Figure 4.1 (ii) shows the position of the particle near the edge of the potential well. At the edge, the relative flow velocity reaches the critical limit = v_c, beyond this critical limit the particle escapes from the trap. This critical velocity is known as the escape velocity (v_{escape}) of the trap and the corresponding trapping force is called escape force [88] or maximum trapping force, which is given by

$$F_{max} = F_{escape} = 6\pi\eta a v_{escape} \tag{4.4}$$

Therefore, knowing the escape velocity, the maximum optical force on the trapped particle can be determined. This method, however, cannot give us the information of trap-stiffness as the particle reaches the non-linear region where the Hooke's law doesn't work.

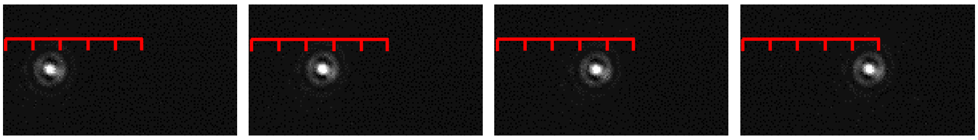

(i) (ii) (iii) (iv)

Fig. 4.3 Experimental images of beam movement (i) → (iv) at average uniform velocity of 20 μm/sec. The markings of the scale bar in each image are of equal length = 1 μm.

4.3 Transverse translation of trapped bead with uniform speed and uniform acceleration

In the previous section we have briefly discussed the experimental techniques to measure the optical forces acting on a trapped bead. However, to implement each technique specific devices or experimental arrangement may be required. In this work we will try to implement the drag force method and the escape force method utilizing our holographic optical trap setup. Additionally, to do further assessment of the various optical forces and their range, we have decided to implement uniform and non-uniform relative movement of the trapping beam. Behavior of the trapped particle when the beam has a uniform velocity or a fixed acceleration can add to our understanding regarding the forces acting on the particle.

In chapter 3 we have observed how the trapping beam in the sample plane can be moved to any user defined location, as long as the beam does not go out of the range of the setup. Here, we construct a sequence of binary holograms with tilts in each hologram described in such a way that the +1 order beam moves in a specific direction in equal step size as the sequence of holograms is displayed on the NLCSLM. We capture each position of the focal spot of the +1 order beam in the sample plane by taking one image of the sample plane after each display of binary hologram. Figures 4.3 (i→iv) show four successive positions of the +1 order beam in the sample plane using 1.4 NA oil immersion lens. We observe that after the display of each hologram the beam moves by an amount of 1 μm in accordance with the increment in the applied tilt values. It is to be noted that the step size of the beam can be arbitrarily large only to be limited by the pixel resolution of the NLCSLM, and the step interval is decided by the update or refresh rate of binary holograms.

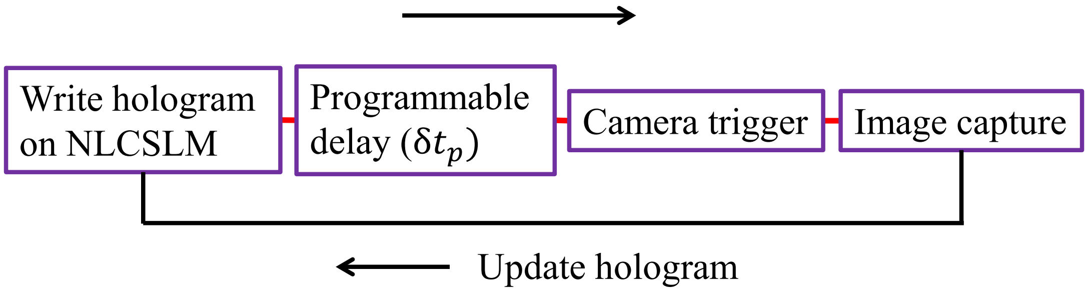

Fig. 4.4 Sequence of events between hologram display and image capture by camera.

To control the step interval precisely and also to ensure that the sequence of binary holograms are displayed without any miss or repetition, the display in the NLCSLM and the image captured in the camera are synchronized with the help of our microprocessor based unit as shown in Fig.4.4. As illustrated in the above figure after the 1^{st} hologram is displayed, the labview program in the PC sends a signal and a number (say n) to the microprocessor unit after which the microprocessor unit creates a trigger signal for the camera after an interval equal to $n\times$ 5.5 msec. The interval ensures that the camera captures the sample plane only after the NLCSLM successfully displays a given binary hologram. For rest of the binary holograms in the sequence the above process is repeated such that the timing of the image capture by the camera relative to the display of a new binary hologram remains identical. Using this arrangement, we are able to achieve a minimum step interval of 50 msec [89]. Table 4.1 shows the coordinates of successive beam locations, their separations and estimated mean velocity which is approximated as 20 μm/sec.

After verifying that our holographic optical trap setup is capable of providing a uniform speed to the beam, we then utilize the same to move the trapped particle. We first trap 2 μm diameter silica beads using the 1.4 NA lens with a beam power of 10 mW (as measured in the entrance pupil plane of the objective lens). To be noted that when the beam powers in the entrance pupil plane are 10 mW and 17 mW, the power in the sample plane of the 1.4 NA lens are measured to be $\approx$ 5 mW and $\approx$ 9 mW, respectively, owing to various losses in transmission

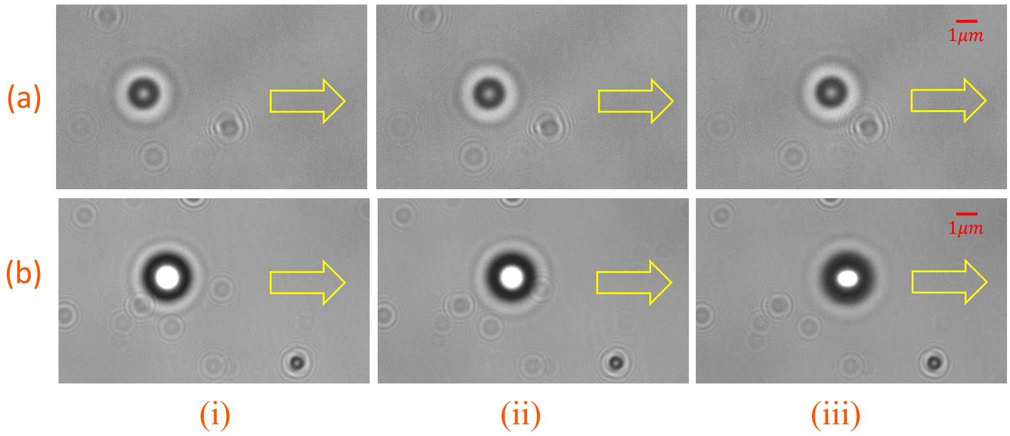

Fig. 4.5 Images of three consecutive bead locations as (a) the 2 μm bead is following the beam movement of 32 μm/sec and (b) the 3 μm bead is following the beam movement of 40 μm/sec.

through the lens and the fact that the beam overfills the entrance pupil of the objective lens. The Gaussian intensity profile of the beam in the entrance pupil corresponds to σ = 4 mm. We perform experiments on the bead by using different step sizes and step intervals. We observe that the 2 μm bead can be moved with a uniform velocity upto a value of 32 μm/sec, which is when the beam has a step size of 1.6 μm and the holograms are updated at an interval of 50 msec.

Table 4.1 **Experimental measurement of beam velocity for a given step size of 1.0 μm and step interval of 50 msec.**

No. of positions	**Position of beam (Camera plane index)** (x , y)	**Estimated step size in μm**	**Estimated velocity of beam in μm/sec**	**Average velocity in μm/sec**
1	(577 , 479)			
2	(593 , 479)	0.937	18.74	
3	(611 , 480)	1.054	21.08	20
4	(628 , 479)	0.996	19.92	

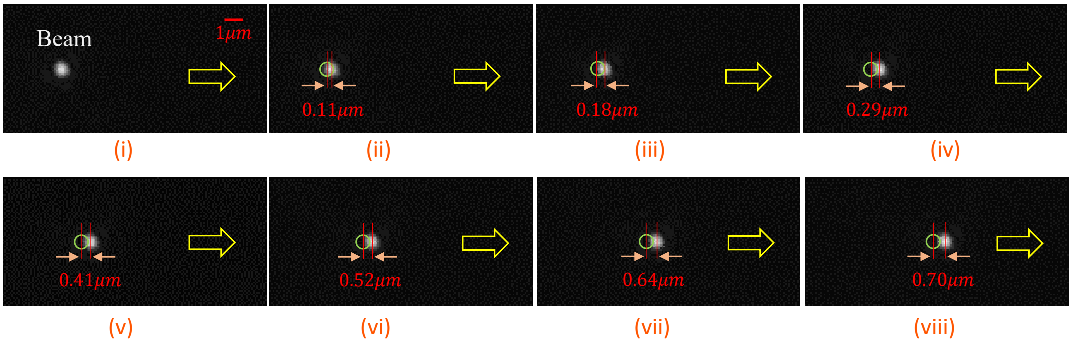

Fig. 4.6 (i)→(viii) are the experimental images of successive beam positions for a trapping beam accelerating at 40 μm/sec^2. Green circle in an image is the position of the beam in the previous image frame.

Figure 4.5 (a) shows three consecutive positions of 2 μm diameter bead with a step size of 1.6 μm. If we increase the step size further keeping the step interval same at 50 msec, we observe that soon the trap is lost. This indicates that for the given bead and using the given beam power we can not impart any larger velocity more than 32 μm/sec. We also perform similar experiments with bigger particles such as beads of 3 μm diameter using the same lens and beam power of $\approx$ 9 mW in the sample plane. We notice that for the bigger bead our holographic optical trap is able to provide a maximum velocity of 40 μm/sec which is when the step size is 2.0 μm and the step interval is 50 msec as shown in Fig. 4.5 (b).

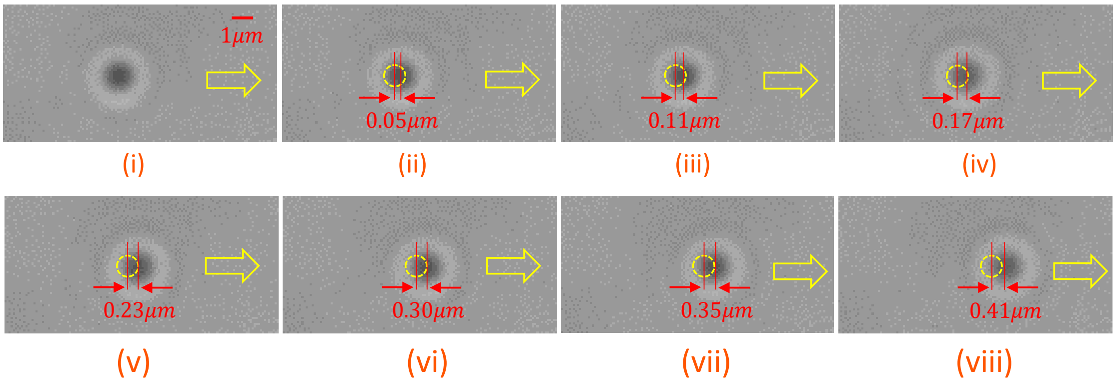

Fig. 4.7 (i)→(viii) are the experimental images of successive bead positions for a trapping beam accelerating at 20 μm/sec^2. Yellow dotted circle in an image is the position of the bead in the previous image frame.

We can also display a sequence of binary holograms to provide a uniform acceleration to the trapping beam using a similar arrangements. In this case the successive holograms correspond to tilt increments which themselves increase by a fixed amount. Figures 4.6 (i→viii) show the experimental images of successive beam positions when the tilt increment in a given hologram is more than the same of the previous hologram by 0.1 μm. We then perform experiment to provide uniform acceleration to the trapped bead by using the above arrangement. Figures 4.7 (i→viii) show images of the trapped beads when the beam is accelerating at a rate of 20 μm/sec^2. We notice that the bead follows the trapping beam upto 10 number of steps without getting lost.

4.4 Experimental measurement of stiffness constant κ

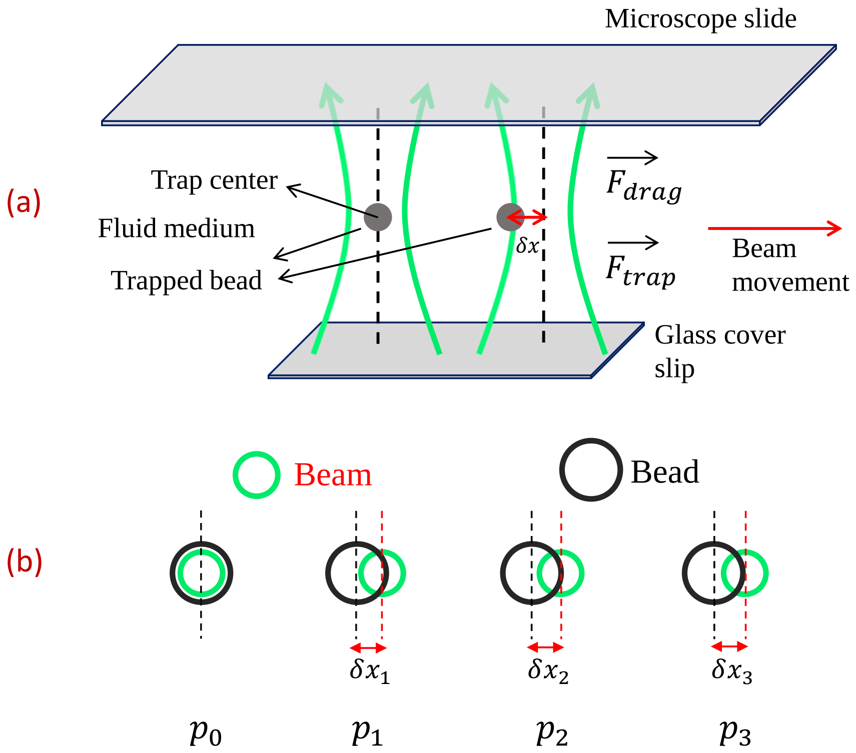

Fig. 4.8 (a) shows relative positions of the beam and the trap center as the beam is moving from left to right. (b) shows separations between the beam and the bead as the beam starts moving from the position p_0.

We employ the drag force method to measure the stiffness constant associated with a trapped spherical bead. As we have discussed already, the drag force method requires movement of the fluid relative to the bead which normally is provided by moving the sample stage with a uniform velocity. However, moving the sample stage with a uniform velocity will require a precision translation stage. Fortunately by providing a uniform velocity to the trapped bead as we have demonstrated already in the previous section it will be possible to get a relative motion between the bead and the fluid using our holographic setup. As shown in Fig. 4.8 (a) the beam and hence the bead is moved with a uniform velocity in a particular direction. Therefore, the bead will experience a drag force $\vec{F_{drag}}$ in a direction opposite to the beam movement. The bead is also acted upon by the trapping force $\vec{F_{trap}}$ opposite to the direction of the drag force. The trap force balances the drag force when the bead is displaced from the trap center by an amount δx. In our experiment the beam moves with a uniform velocity (in small discrete steps) and is followed by the bead moving with the same uniform velocity, however maintaining a certain distance form the center of the beam, as seen in Fig. 4.8 (b). From our experimental arrangement described in the previous section we have the images of the moving beads captured a given duration after the display of each hologram. The duration is chosen in such a way that the beam positions with respect to time, corresponding to the image data, can be approximated to follow a straight line. Since, the exact position of the beam in the camera plane is known from the tilt values used in the hologram hence analysis of each image should give us the displacement of the bead with respect to the beam center for each beam position.

4.4.1 Procedure to estimate the stiffness constant experimentally

1. A sequence of binary holograms are computed to provide a uniform velocity to the trapping beam and then displayed on the NLCSLM. For each beam position the respective image of the trapped bead is captured.

2. Initial position of the beam in the camera plane prior to the beam movement which is also the initial position of the trapped bead is noted. This position is shown as p_0 in Fig. 4.8 (b).

3. Using the coordinate of p_0 the successive beam positions in the rest of the image frames p_1, p_2, p_3 and so on, are determined. The center of each trapped bead is visually identified and located in each image frame.

4. The bead displacement from the beam center δx_1, δx_2, δx_3 and so on for the successive image frames are determined by using the beam positions p_1, p_2, p_3 and so on and the respective bead positions.

5. The mean displacement δx of the bead for a given uniform velocity is then used to obtain the stiffness constant using the relation $\kappa = \frac{6\pi\eta av}{\delta x}$, where $\eta = 1.002\times10^{-3}$ Pascal-second.

4.4.2 Experimental results

We measure the stiffness constant of different trapped beads under different illumination conditions. For the purpose of comparing the experimental values with those obtained using the proposed model, we decide to consider the relative change in the experimental or theoretical values, rather than the absolute values. This is done by normalizing the experimental and theoretical values under a certain situation by the respective maximum value. Use of normalized values for comparison allows us to ignore the variations in the absolute values due to systematic errors.

First we consider the stiffness constant associated with the 2 μm and 3 μm beads when the illumination beam has a Gaussian intensity profile with a net power of $\approx$ 5 mW and $\approx$ 9 mW in the sample plane. We use the experimental results of the 2 μm bead when the trapping beam is moving with velocity 32 μm/sec and of the 3 μm bead when the trapping beam is moving with velocity 40 μm/sec. The stiffness constant for the 2 μm bead is estimated to be 4.04 $\times10^{-7}$ N/m and the same for the 3 μm bead is estimated to be 8.26 $\times10^{-7}$ N/m. The respective stiffness constant values obtained from the model are 5.17 $\times10^{-7}$ N/m and 1.14$\times10^{-6}$ N/m. As seen in the table 4.2 the respective theoretically obtained normalized stiffness constants agree reasonably well with the normalized experimental values .

In addition to the Gaussian illumination beam we also consider trapping of beads using annular beams whose generation has been discussed already in chapter 3. We manage to trap

Table 4.2 **Comparison between (normalized using the respective stiffness constant value for the 3 μm bead) theoretical and experimental stiffness constants for the 2 μm and the 3 μm beads using a Gaussian beam of power $\approx$ 5 mW and $\approx$ 9 mW (in the sample plane), respectively. Also seen is the experimental mean displacement δx which is used in the determination of experimental stiffness constant.**

Bead diameter in micron	**Power in mW**	**Mean δx (expt) in μm**	**Normalized stiffness (expt)**	**Normalized stiffness (theory)**
2	5	1.5	0.49 ± 0.05	0.45
3	9	1.37	1 ± 0.074	1

a small 0.7 μm silica bead using annular beams with inner radius (r_i) varying from 0.1 to 0.4. The experimental images of the trapped beads for each beam position are employed as in the above experiment to estimate the respective stiffness constants. The table 4.3 shows the experimentally obtained stiffness constants for the 0.7 μm beads for different annular beams normalized by the value corresponding to $r_i = 0.1$ and the respective theoretically obtained normalized stiffness constants. As we see from the experimental values in the table, with the increase of the inner radius the stiffness constant decreases and this trend agrees reasonably well with the theoretical calculations.

The small amount of disagreement between theory and experiment can be primarily attributed to the inability in defining the precise values of experimental parameters such as exact laser power in the sample plane, the value of σ in the entrance pupil, exact size of the bead, precise refractive index of the medium and the bead and influence of glass surface on bead movements. A small error in the measurement of any of these parameters may lead to significant change in the calculated forces. Moreover, for the model to give the most accurate optical force for a given beam, its entrance pupil needs to be described by as many pixels as possible.

Table 4.3 **Comparison between theoretical and experimental stiffness constants for the 0.7 μm bead using an annular Gaussian beam of power $\approx$ 9 mW in the sample plane as the normalized r_i value changes from 0.1 to 0.4. The experimental and the respective theoretical stiffness constant values are normalized by the respective stiffness constants for $r_i = 0.1$, which are estimated to be 2.813×10^{-6} N/m and 2.7878×10^{-6} N/m, respectively.**

Bead diameter in μm	**δx in μm**	**Beam velocity in μm/sec**	**Inner radius of annular beam (normalized radius)**	**Normalized stiffness (theory)**	**Normalized stiffness (experiment)**
0.7	0.03	8	0.4	0.77	0.63 ± 0.02
0.7	0.029	8	0.3	0.87	0.81 ± 0.1
0.7	0.022	10	0.2	0.95	0.86 ± 0.03
0.7	0.014	8	0.1	1	1 ± 0.01

4.5 Experimental measurement of escape force and the range of optical force

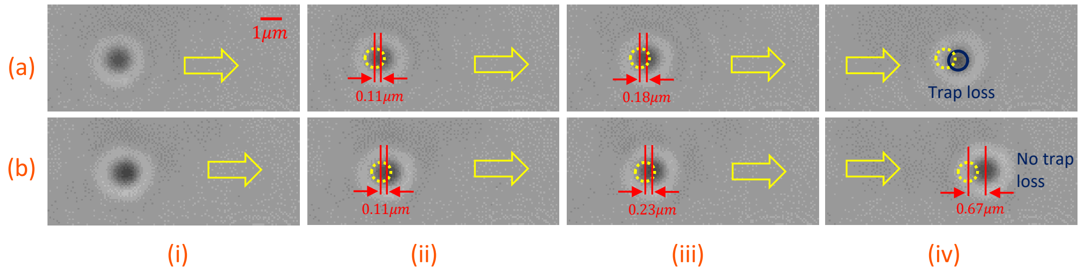

Fig. 4.9 Images of the trapped bead in successive three steps starting from the initial position (i), when the beam power is (a) $\approx$ 5 mW and (b) $\approx$ 9 mW in the sample plane. (iv) is the image frame in the 8^{th} step. Yellow dashed circle is the bead position in the previous step and yellow arrow is the direction of beam movement.

In section 4.3 we have presented experimental results showing bead movement with uniform velocity. The 2 μm bead could be moved with a maximum velocity of 32 μm/sec using beam power of ≈ 5 mW in the sample plane while the 3 μm bead could be moved with a maximum velocity of 40 μm/sec using beam power of ≈ 9 mW in the sample plane. Any further increase in the velocity of the beam leads to the loss of the respective trap, as the beam velocity becomes greater than the escape velocity. The peak value of the optical force vs displacement plot as seen in Fig. 2.10 of chapter 2 decides the maximum achievable velocity of the trapped bead.

Table 4.4 **Experimentally observed step size, step interval, maximum mean bead velocity and normalized escape force. Also shows normalized escape force obtained theoretically. The escape force is normalized using the maximum value in the respective column (i.e. corresponding to the 3 μm bead, which are estimated to be 1.13×10^{-12} N from experimental data and 2.0×10^{-12} N from the model).**

Bead diameter in μm	**Beam power in mW**	**Step size (in μm)**	**Step interval (in msec)**	**Bead velocity (in μm/sec)**	**Normalized escape force (Expt)**	**Normalized escape force (Model)**
2	5	1.6	50	32.0	0.53	0.4
2	5	1.8	67	26.9	0.44	0.4
3	9	2.0	50	40.0	1	1

As long as the beam provides a uniform velocity to the trapped bead the optical force acting on the bead is balanced by the drag force. Hence using the relation $\vec{F_{trap}} = 6\pi\eta av$ we can find out the escape force or the maximum optical force using the estimated maximum achievable bead velocity. Table 4.4 shows the experimentally obtained maximum bead velocities for the 2 μm and 3 μm beads using beam power of ≈ 5 mW and ≈ 9 mW in the sample plane, respectively, and the respective normalized forces. The escape force in each column is normalized using the respective escape force value corresponding to the 3 μm bead. It is noticed that there is a reasonably good agreement between the experiment and the theory in the case of normalized escape forces.

When we consider the accelerated bead as discussed in section 4.3 we observe that the instantaneous velocity of the trapped bead keeps increasing after every step. Therefore, the trapped bead will stop following the beam as soon as the instantaneous velocity of the beam exceeds the escape velocity. Calculations using ray-pencil model as discussed in section 2.5

of chapter 2 show that the escape velocity increases with the increase in the beam power. We have performed experiment using the 2 μm bead with beam power of $\approx$ 5 mW and $\approx$ 9 mW in the sample plane. Our results show that the 2 μm bead using $\approx$ 5 mW of sample plane beam power when given an acceleration of 40 μm/sec^2 the trap is lost in the 8^{th} step as seen in Fig. 4.9 (a). However, if the sample plane beam power is increased to $\approx$ 9 mW the trap is not lost even in the 8^{th} step as seen in Fig. 4.9 (b). This indicates that with the increase in beam power the bead can be moved with higher instantaneous velocity in agreement with the prediction by the model.

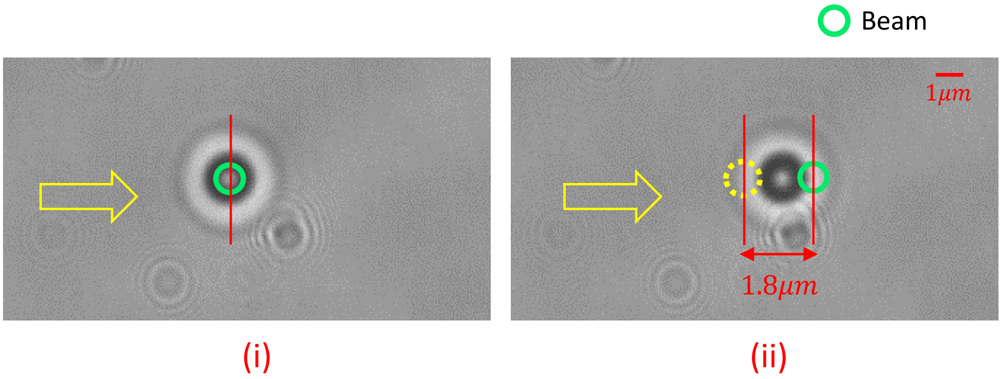

Fig. 4.10 Images of the 2 μm bead (i) in the initial position and (ii) after the first step by the beam. The green circle in (ii) is the beam position while the yellow dotted circle is the bead position in the previous image.

In chapter 2 we see that when a Gaussian beam traps a bead of given diameter the optical force remains non-zero upto a displacement very close to the diameter of the bead. Therefore, a trapped bead experiences an attractive force towards the trap center till the distance between the center of the bead and the beam is equal to the diameter of the bead. However, the magnitude of the optical force decreases as the separation increases, hence the bead will be able to overcome the drag force to come to the center from a distance equal to its diameter only if the beam has sufficient power. Provided the beam has sufficient power the maximum step size of the beam in our experiment to provide uniform velocity to the bead is determined by this range of the optical force. Our results seen in Fig. 4.10 show that we are able to move a 2 μm bead with a step size of 1.8 μm and step interval of 67 msec using beam power of $\approx$ 5 mW in the sample plane. Thus the step size is very close to the diameter of the bead as seen in Fig. 4.10, as expected considering the theoretical predictions.

4.6 Experimental validation of increase in the range of optical force using vortex beams

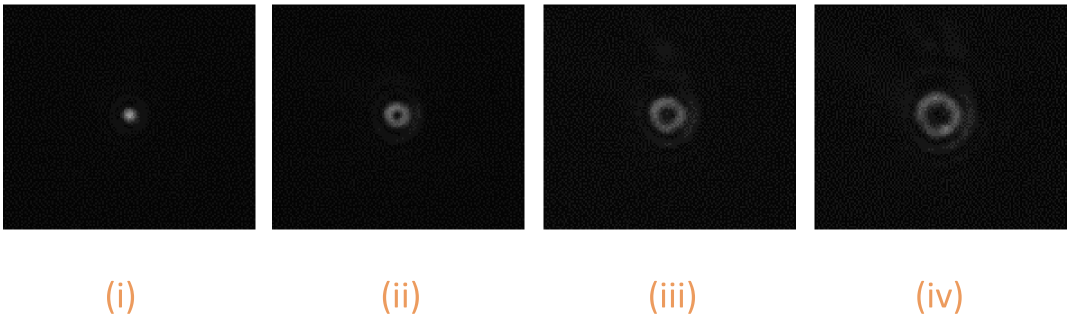

Fig. 4.11 Experimental images of focal spots for (i) $l = 0$, (ii) $l = 1$, (iii) $l = 2$ and (iv) $l = 3$, using the 1.4 NA lens.

Our holographic optical trap setup is capable of generating various complex as well as interesting light beams such as vortex beams. Vortex beam has a complex amplitude profile given as $\exp(il\theta)$ where, l is the topological charge which takes integral values and θ is the azimuthal angle. We have generated illumination beams with $l = 0$, $l = 1$, $l = 2$, $l = 3$ and experimental images of respective focal spots using the 1.4 NA lens are seen in Fig. 4.11. It is noticed that unlike the Gaussian beam ($l = 0$), the vortex beams have doughnut like intensity distribution whose size increases with the topological charge.

We have used the gradient approach of our force calculation model to compute the optical force vs displacement of the bead considering beam power of 17 mW and 2 μm diameter silica beads for trapping, due to Gaussian as well as vortex beams. For this computation we use $\phi(x,y) = l\theta(x,y)$ in Eq. 2.38 of chapter 2. From Fig. 4.12 we see that as the topological charge increases the stiffness constant of the trap decreases. However, with the increase in the l value, the magnitude of the optical force at larger displacements, for instance displacements larger than 1.5 μm, are found to be greater than the same for a beam with lower l value. To be noted

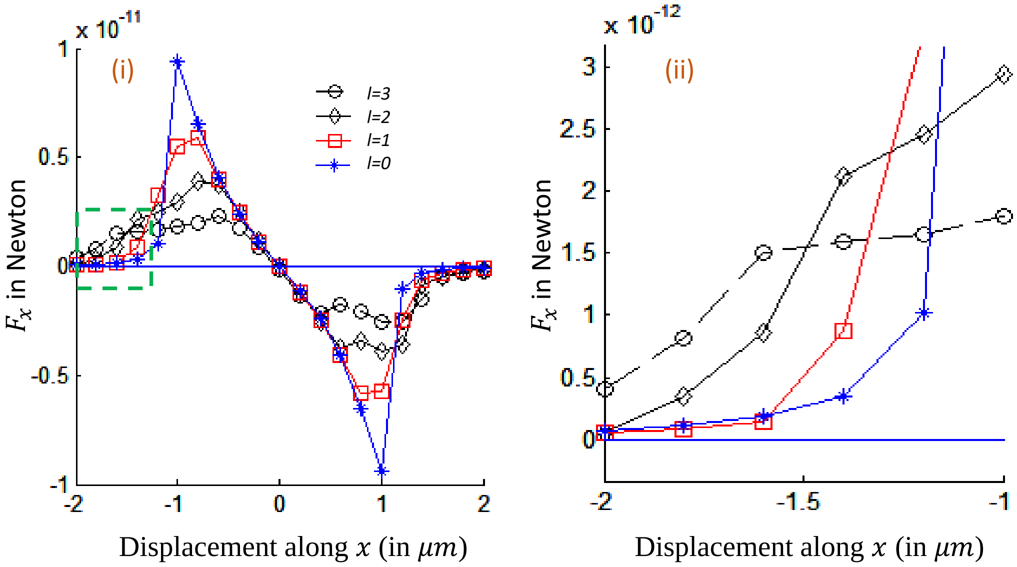

Fig. 4.12 (i) F_x vs displacement along x plot using the gradient approach of the augmented ray-pencil model for $l = 0$, $l = 1$, $l = 2$ and $l = 3$, using the 1.4 NA lens. (ii) shows a magnified view of the green dashed rectangular region in (i). It is seen that for displacements between 1.4 μm to 2 μm, the F_x values for the $l = 3$ and $l = 2$ beams are greater than the values for $l = 1$ and $l = 0$ beams.

that such enhancement in the optical force for higher l values relative to the lower l value will be observed for any beam power. Therefore, according to our model the Gaussian beam can impart the maximum possible velocity to a trapped bead compared to a vortex beam, having the same power. However, the vortex beam should be able to provide larger step size while transporting a bead, although with a smaller velocity or larger step interval.

In order to study the above behavior we trap 2 μm bead using both Gaussian and vortex beams. We move the beams first with a step size of 1.6 μm and a large step interval of 200 msec. As seen in Figs. 4.13 (a→d) the bead follows the trapping beam for larger topological charges, for instance, $l = 2$ and $l = 3$. On the other hand for $l = 1$ and for the Gaussian beam the trap loses the bead almost immediately as the beam starts moving. We perform another experiment with the same bead and beams by increasing the step size to 2 μm. As seen in Figs. 4.14 (a→d) with the increased step size the bead follows the beam only in the case of $l = 3$ while for all other cases the trap loses the bead once the beam starts to move. It is to be noted that if the step interval is made smaller, say equal to 50 msec, then both the Gaussian as well as

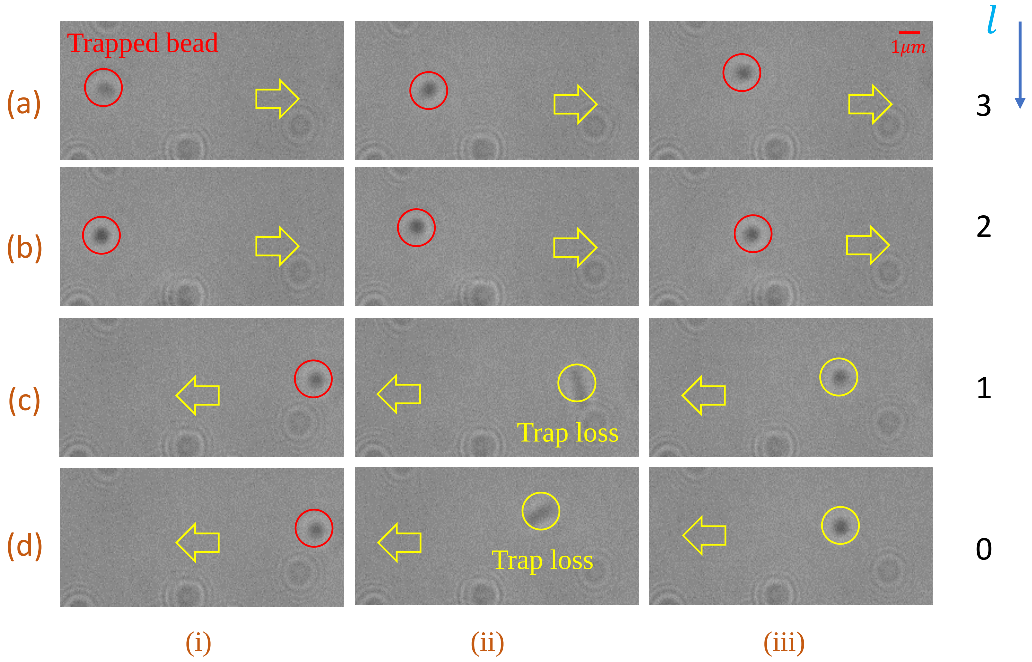

Fig. 4.13 (i), (ii) and (iii) are three consecutive positions of the 2 μm bead starting from the rest position (i). The step size of the moving beam is 1.6 μm. The value of l corresponding to each image row is shown on the right. The red circle encloses the trapped bead while the yellow circle encloses the lost bead. Yellow arrow head indicates the direction of trapping beam movement.

the vortex beams can not move the bead using the given step size. Therefore the above two experimental results offer a convincing validation of the optical force vs. displacement plot for arbitrary wavefronts using the proposed force calculation model.

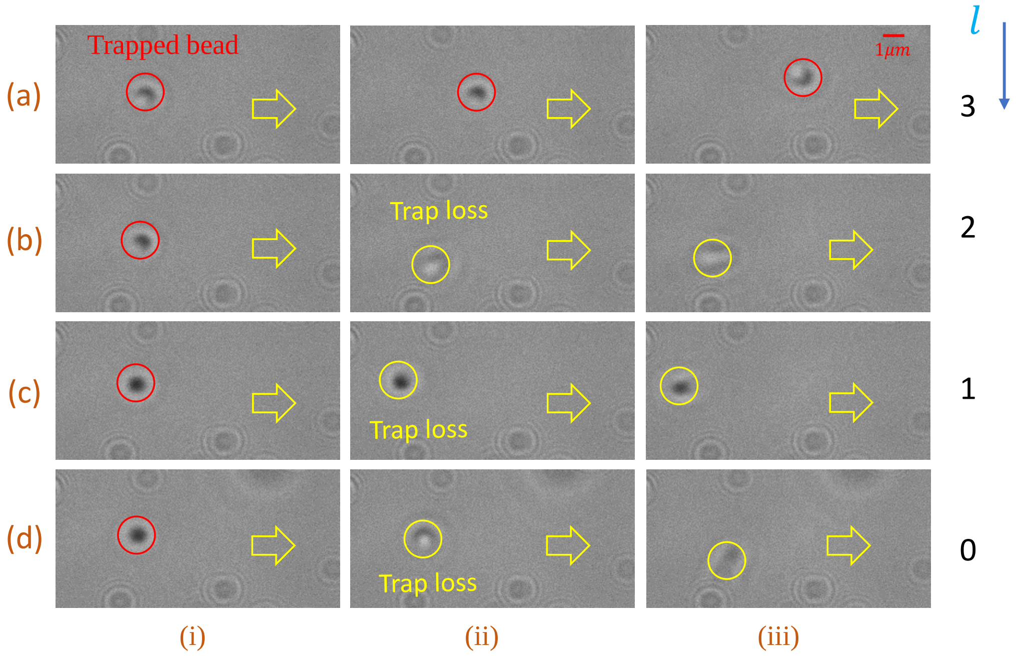

Fig. 4.14 (i), (ii) and (iii) are three consecutive positions of the 2 μm bead starting from the rest position (i). The step size of the moving beam is 2 μm. The value of l corresponding to each image row is shown on the right. The red circle encloses the trapped bead while the yellow circle encloses the lost bead. Yellow arrow head indicates the direction of trapping beam movement.

4.7 Summary

In this chapter we have first described the experimental techniques to measure the optical forces which are used in the present work. We have then demonstrated the capability of our set up to provide uniform velocity and acceleration to the trapped bead. We have discussed how stiffness constant has been measured in our experimental setup and then presented the experimental results along with the relevant numerically obtained results. We have also measured the escape force and the range of the optical forces experimentally and compared them with the numerical simulation results. We have performed experiments with vortex beams and observed the range of optical forces for various topological charges. Since the proposed augmented model can calculate the optical forces for any arbitrary complex amplitude profiles, we have used our model to obtain the range of optical forces for vortex beams and found that the experimental observations agree reasonably well with the theory.

* * *

CHAPTER 5

Overall conclusion and future prospects

5.1 Overall conclusion

A laser beam when focused tightly using a high numerical aperture lens, there appears a pico-Newton level attractive force on microscopic particles towards the focus. This phenomenon is known as single beam gradient trap. Over the last few decades single beam gradient trap has found applications in diverse areas specially in biological science and biomedical research. Acknowledging the contribution of optical trap, the area has been awarded with Nobel prize in Physics. For efficient working of the optical traps in various applications, it is important to be able to calculate the magnitude of various optical forces arising in the system, using some theoretical model. There have been models using electromagnetic wave approximation and ray-optics approximation of light beams. However, for most of the applications such as in biological science related areas where the trapped particle is much larger than the wavelength of light, the ray-optics models are found to be more appropriate. In this thesis we first study the popular optical force calculation model in the ray-optics regime reported by Ashkin, et al. [41]. In this thesis we refer to the Ashkin's model as the ray-pencil model. We observe that even though the model in principle should be able to calculate the optical forces due to any beam profile, however, the same has mostly been used for specific beam profiles such as Gaussian or cylindrically symmetric beam profiles. A survey of the present day applications of optical trap reveals that in many applications there have been use of non conventional light beams such as vortex beams. Besides most of optical systems invariably suffer from various aberrations. In all such cases the present form of the ray-pencil model is not suitable. In this work we have proposed an augmentation in the existing ray-pencil model so that it is able to calculate the optical forces for arbitrary beam profile including that of an aberrated beam and a vortex beam. We have presented the development of the mathematical expressions and showed how they can be easily computed using a PC. Having proposed the augmented ray-pencil model we have developed a holographic optical trap (HOT) setup using a nematic liquid crystal spatial light modulator (NLCSLM). We have used our holographic trap system to perform trapping experiments using various spherical beads and symmetric beam profiles. Our experimental results have validated the optical force calculations using our proposed model. We have also performed experiments using vortex beams with different topological charges. The proposed model was used to calculate the optical forces acting on a bead trapped by a focused vortex beams. Our experimental results using vortex beams have presented clear evidence on the accuracy of the above theoretical results.

Below we provide a chapter wise summary of this thesis work:

In chapter 1, we have started with a general introduction of the research objective and an overview of the entire thesis.

In chapter 2, we have briefly discussed various optical force calculation models while emphasizing more on the models in the ray-optics regime. We have described the ray-pencil model and how it can be implemented for Gaussian laser beams. We have then introduced an augmentation in the ray-pencil model so that the model can be applied for arbitrary beam profiles. We have demonstrated the working of the proposed model by comparing numerical simulation results with those using the existing ray-pencil model.

In chapter 3, we have introduced the principle of classical holography and extended the concept to discuss the computer generated holography technique. We have then discussed the construction of binary hologram to modulate the complex amplitude of the +1 order diffracted beam and implementation of the same using an NLCSLM. This is followed by a discussion on the experimental arrangement to implement the holographic optical trap. The chapter then presents experimental results to demonstrate the performance of various features of the holographic optical trap arrangement. We have ended the chapter with a demonstration of trapping and movement of beads using two different objective lenses.

In chapter 4, we have first described the experimental techniques to measure the optical forces relevant for the thesis work. We have then demonstrated the capability of our setup to provide uniform velocity and acceleration to a trapped spherical bead. The chapter then discusses how stiffness constant has been measured in our experimental setup and then presents the experimental results along with the relevant numerically obtained results. We have also measured the escape force and the range of the optical forces experimentally and compared them with the numerical simulation results. We have performed experiments with vortex beams and observed the range of optical forces for various topological charges experimentally. Since the proposed augmented model can calculate the optical forces for any arbitrary complex amplitude profiles, we have used our model to obtain the range of optical forces for vortex beams. We have found that the experimental observations agree reasonably well with the predictions of the augmented model.

Chapter 5 concludes the thesis with a summary and future prospects.

5.2 Future prospects

Even though we have validated the proposed augmentation of the ray-pencil model both numerically and experimentally yet our model with the help our holographic trap system can be employed to make several interesting investigations. Some such investigations are listed below.

1. We have used our model to compute the net optical force on the trapped bead due to a vortex beam. However, the same can also be extended to obtain the vectorial profile of the force in 3D. Such a 3D profile will be useful to understand how a trap particle behaves, for instance, rotation of the particle near the focus of the vortex beam.

2. Our model can also be used to study how various monochromatic aberrations effect the trap efficiency of a focused beam. Such theoretical study can then be validated

experimentally using our holographic optical trap, as using our experimental arrangement one can introduce a user defined phase profile into the incident beam.

3. Our model can also be used in the study of various physical properties of the trapping medium such as viscosity, refractive index, presence of impurity and so on. The tunability of our holographic optical trap can than be exploited to develop novel measurement techniques for precise measurement of the above properties. Numerical simulation results will help determining the accuracy of such experimental techniques.

4. The proposed augmentation of the ray-pencil model is at present applicable for scalar beams only however, the same can be further developed for arbitrary vector beams. We have already started working in this direction and observed some interesting results. We expect to conclude this work shortly by further developing the proposed model and extending it to vector beams.

★ ★ ★

APPENDIX A

Force calculation in the ray-optics regime

Using Fig. 2.6 of chapter 2 the expressions of scattering force F_{sc} and gradient force F_{grad} for a single ray on a particle, are derived in detail. Considering the conservation of linear momentum the force components for a single ray are given as

$$dF_{z'} = \frac{n_{med}dP}{c} - \left[\frac{n_{med}dPR}{c}\cos(\pi-2\alpha) + \sum_{n=0}^{\infty}\frac{n_{med}dPT^2R^n}{c}\cos(\psi+n\phi)\right] \tag{A.1}$$

which acts along $\hat{z}'$ and

$$dF_{y'} = 0 - \left[\frac{n_{med}dPR}{c}\sin(\pi-2\alpha) - \sum_{n=0}^{\infty}\frac{n_{med}dPT^2R^n}{c}\sin(\psi+n\phi)\right] \tag{A.2}$$

which acts along $\hat{y}'$. For the above two equations the meaning of the symbols have already discussed in section 2.3 of chapter 2. The total force on the particle in the complex plane is $dF_{tot} = dF_{z'} + idF_{y'}$. So,

$$\begin{aligned} dF_{tot} = {} & \frac{n_{med}dP}{c} - \left[\frac{n_{med}dPR}{c}\cos(\pi-2\alpha) + \sum_{n=0}^{\infty}\frac{n_{med}dPT^2R^n}{c}\cos(\psi+n\phi)\right] \\ & -i\left[\frac{n_{med}dPR}{c}\sin(\pi-2\alpha)\right] + i\left[\sum_{n=0}^{\infty}\frac{n_{med}dPT^2R^n}{c}\sin(\psi+n\phi)\right] \end{aligned} \tag{A.3}$$

or,

$$dF_{tot} = \frac{n_{med}dP}{c}\Big[1+R\cos(2\alpha)\Big] - i\Big[\frac{n_{med}dPR}{c}\sin(2\alpha)\Big] - \frac{n_{med}dPT^2}{c}\Big[\sum_{n=0}^{\infty} R^n\cos(\psi+n\phi) - i\sum_{n=0}^{\infty} R^n\sin(\psi+n\phi)\Big] \tag{A.4}$$

or,

$$dF_{tot} = \frac{n_{med}dP}{c}\Big[1+R\cos(2\alpha)\Big] - i\Big[\frac{n_{med}dPR}{c}\sin(2\alpha)\Big] - \frac{n_{med}dPT^2}{c}\Big[\sum_{n=0}^{\infty} R^n e^{-i(\psi+n\phi)}\Big] \tag{A.5}$$

or,

$$dF_{tot} = \frac{n_{med}dP}{c}\Big[1+R\cos(2\alpha)\Big] - i\Big[\frac{n_{med}dPR}{c}\sin(2\alpha)\Big] - \frac{n_{med}dPT^2}{c}\Big[\frac{e^{-i\psi}}{1-Re^{-i\phi}}\Big] \tag{A.6}$$

From Fig. 2.6 (i) we see that, $\psi = 2(\alpha-\beta)$ and $\phi = (\pi-2\beta)$ Therefore,

$$dF_{tot} = \frac{n_{med}dP}{c}\Big[1+R\cos(2\alpha) - iR\sin(2\alpha)\Big] - T^2\Big[\frac{e^{-2i(\alpha-\beta)}}{1-Re^{-i(\pi-2\beta)}}\Big] \tag{A.7}$$

or,

$$dF_{tot} = \frac{n_{med}dP}{c}\Big[1+R(\cos(2\alpha)-i\sin(2\alpha)) - T^2\frac{\cos(2\alpha-2\beta)-i\sin(2\alpha-2\beta)}{1+R\cos(2\beta)+iR\sin(2\beta)}\Big] \tag{A.8}$$

Extracting the real and imaginary parts from the above equation we get,

$$dF_{sc} = dF_{z'} = \frac{n_{med}dP}{c}\Big[1+R\cos(2\alpha) - \frac{T^2[\cos(2\alpha-2\beta)+R\cos(2\alpha)]}{1+R^2+2R\cos(2\beta)}\Big] \tag{A.9}$$

and

$$dF_{grad} = dF_{y'} = -\frac{n_{med}dP}{c}\Big[R\sin(2\alpha) - \frac{T^2[\sin(2\alpha-2\beta)+R\sin(2\alpha)]}{1+R^2+2R\cos(2\beta)}\Big] \tag{A.10}$$

References

---

[1] John David Jackson. Classical electrodynamics, 1999. 1, 16

[2] Ernest Fox Nichols and Gordon Ferrie Hull. The pressure due to radiation. In *Proceedings of the American Academy of Arts and Sciences*, volume 38, pages 559–599. 1

[3] Ernest Fox Nichols and Gordon Ferrie Hull. The pressure due to radiation.(second paper.). *Physical Review (Series I)*, 17(1):26, 1903.

[4] EF Nichols and GF Hull. The application of radiation pressure to cometary theory. *The Astrophysical Journal*, 17:352, 1903. 1

[5] Arthur Ashkin. Acceleration and trapping of particles by radiation pressure. *Physical review letters*, 24(4):156, 1970. 1

[6] Arthur Ashkin, James M Dziedzic, JE Bjorkholm, and Steven Chu. Observation of a single-beam gradient force optical trap for dielectric particles. *Optics letters*, 11(5):288–290, 1986. 1, 10

[7] Stephen P Smith, Sameer R Bhalotra, Anne L Brody, Benjamin L Brown, Edward K Boyda, and Mara Prentiss. Inexpensive optical tweezers for undergraduate laboratories. *American Journal of Physics*, 67(1):26–35, 1999. 2

[8] MS Rocha. Optical tweezers for undergraduates: theoretical analysis and experiments. *American Journal of Physics*, 77(8):704–712, 2009. 2, 5, 13, 18

[9] Arthur Ashkin and James M Dziedzic. Optical trapping and manipulation of viruses and bacteria. *Science*, 235(4795):1517–1520, 1987. 2

[10] Xiaolin Wang, Shuxun Chen, Marco Kong, Zuankai Wang, Kevin D Costa, Ronald A Li, and Dong Sun. Enhanced cell sorting and manipulation with combined optical tweezer and microfluidic chip technologies. *Lab on a Chip*, 11(21):3656–3662, 2011. 2

[11] Hu Zhang and Kuo-Kang Liu. Optical tweezers for single cells. *Journal of the Royal Society interface*, 5(24):671–690, 2008. 2

[12] Anusha Keloth, Owen Anderson, Donald Risbridger, and Lynn Paterson. Single cell isolation using optical tweezers. *Micromachines*, 9(9):434, 2018. 2

[13] Claudia Arbore, Laura Perego, Marios Sergides, and Marco Capitanio. Probing force in living cells with optical tweezers: from single-molecule mechanics to cell mechanotransduction. *Biophysical reviews*, 11(5):765–782, 2019. 2

[14] Steven B Smith, Yujia Cui, and Carlos Bustamante. Overstretching b-dna: The elastic response of individual double-stranded and single-stranded dna molecules. American Association for the Advancement of Science, 2020. 2

[15] Yuxin Hao, Clare Canavan, Susan S Taylor, and Rodrigo A Maillard. Integrated method to attach dna handles and functionally select proteins to study folding and protein-ligand interactions with optical tweezers. *Scientific reports*, 7(1):1–8, 2017. 2

[16] Christopher N LaFratta. Optical tweezers for medical diagnostics. *Analytical and bioanalytical chemistry*, 405(17):5671–5677, 2013. 2

[17] Samarendra K Mohanty, Abha Uppal, and Pradeep K Gupta. Self-rotation of red blood cells in optical tweezers: prospects for high throughput malaria diagnosis. *Biotechnology letters*, 26(12):971–974, 2004. 2

[18] Yi Liang, Guo Liang, Yinxiao Xiang, Josh Lamstein, Rekha Gautam, Anna Bezryadina, and Zhigang Chen. Manipulation and assessment of human red blood cells with tunable “tug-of-war” optical tweezers. *Physical Review Applied*, 12(6):064060, 2019. 2

[19] Min-Cheng Zhong, Xun-Bin Wei, Jin-Hua Zhou, Zi-Qiang Wang, and Yin-Mei Li. Trapping red blood cells in living animals using optical tweezers. *Nature communications*, 4(1):1–7, 2013. 2

[20] Manlio Tassieri, Francesco Del Giudice, Emma J Robertson, Neena Jain, Bettina Fries, Rab Wilson, Andrew Glidle, Francesco Greco, Paolo Antonio Netti, Pier Luca Maffettone, et al. Microrheology with optical tweezers: Measuring the relative viscosity of solutions ‘at a glance’. *Scientific reports*, 5(1):1–6, 2015. 2

[21] Bryan R Bzdek, Rory M Power, Stephen H Simpson, Jonathan P Reid, and C Patrick Royall. Precise, contactless measurements of the surface tension of picolitre aerosol droplets. *Chemical science*, 7(1):274–285, 2016. 2

[22] Rory M Power and Jonathan P Reid. Probing the micro-rheological properties of aerosol particles using optical tweezers. *Reports on Progress in Physics*, 77(7):074601, 2014. 2

[23] Manlio Tassieri, RML Evans, Rebecca L Warren, Nicholas J Bailey, and Jonathan M Cooper. Microrheology with optical tweezers: data analysis. *New Journal of Physics*, 14(11):115032, 2012. 2

[24] Keir C Neuman and Attila Nagy. Single-molecule force spectroscopy: optical tweezers, magnetic tweezers and atomic force microscopy. *Nature methods*, 5(6):491–505, 2008. 2

[25] MR Tarbutt. Magneto-optical trapping forces for atoms and molecules with complex level structures. *New Journal of Physics*, 17(1):015007, 2015. 2

[26] Matthias Grimm, Thomas Franosch, and Sylvia Jeney. High-resolution detection of brownian motion for quantitative optical tweezers experiments. *Physical Review E*, 86(2):021912, 2012. 2

[27] TJ Davis. Brownian diffusion of nano-particles in optical traps. *Optics express*, 15(5):2702–2712, 2007. 2

[28] NB Simpson, D McGloin, K Dholakia, L Allen, and MJ Padgett. Optical tweezers with increased axial trapping efficiency. *Journal of Modern Optics*, 45(9):1943–1949, 1998. 3

[29] Meng Bing-Huan, Zhou Jin-Hua, Zhong Min-Cheng, Li Yin-Mei, Wu Jian-Guang, and Ren Hong-Liang. Improvement of transverse trapping efficiency of optical tweezers. *Chinese Physics Letters*, 25(6):2300, 2008.

[30] Min Gu, Dru Morrish, and Pu Chun Ke. Enhancement of transverse trapping efficiency for a metallic particle using an obstructed laser beam. *Applied Physics Letters*, 77(1):34–36, 2000. 3

[31] Yi Deng, John Bechhoefer, and Nancy R Forde. Brownian motion in a modulated optical trap. *Journal of Optics A: Pure and Applied Optics*, 9(8):S256, 2007. 3

[32] Tongcang Li and Mark G Raizen. Brownian motion at short time scales. *Annalen der Physik*, 525(4):281–295, 2013. 3

[33] Yasuhiro Harada and Toshimitsu Asakura. Radiation forces on a dielectric sphere in the rayleigh scattering regime. *Optics communications*, 124(5-6):529–541, 1996. 3, 9

[34] Timo A Nieminen, Halina Rubinsztein-Dunlop, Norman R Heckenberg, and AI Bishop. Numerical modelling of optical trapping. *Computer Physics Communications*, 142(1-3):468–471, 2001. 3

[35] Alexander Rohrbach and Ernst HK Stelzer. Optical trapping of dielectric particles in arbitrary fields. *JOSA A*, 18(4):839–853, 2001. 3

[36] G Roosen and C Imbert. Optical levitation by means of two horizontal laser beams: a theoretical and experimental study. *Physics Letters A*, 59(1):6–8, 1976. 3

[37] Gerald Roosen. A theoretical and experimental study of the stable equilibrium positions of spheres levitated by two horizontal laser beams. *Optics Communications*, 21(1):189–194, 1977. 3

[38] Arthur Ashkin. Forces of a single-beam gradient laser trap on a dielectric sphere in the ray optics regime. *Biophysical journal*, 61(2):569–582, 1992. 3, 15

[39] Shenghua Xu, Yinmei Li, and Liren Lou. Axial optical trapping forces on two particles trapped simultaneously by optical tweezers. *Applied optics*, 44(13):2667–2672, 2005. 3

[40] Erik Fällman and Ove Axner. Influence of a glass-water interface on the on-axis trapping of micrometer-sized spherical objects by optical tweezers. *Applied Optics*, 42(19):3915–3926, 2003. 3, 4

[41] Arthur Ashkin. Forces of a single-beam gradient laser trap on a dielectric sphere in the ray optics regime. *Biophysical journal*, 61(2):569–582, 1992. 3, 4, 10, 13, 79

[42] Bum Jun Park and Eric M Furst. Optical trapping forces for colloids at the oil- water interface. *Langmuir*, 24(23):13383–13392, 2008. 4

[43] Jin-Hua Zhou, Min-Cheng Zhong, Zi-Qiang Wang, and Yin-Mei Li. Calculation of optical forces on an ellipsoid using vectorial ray tracing method. *Optics express*, 20(14):14928–14937, 2012. 4

[44] Xin-cheng Yao, Zhao-lin Li, Hong-lian Guo, Bing-ying Cheng, Dao-zhong Zhang, and Xue-hai Han. Effect of spherical aberration introduced by water solution on trapping force. *Chinese Physics B*, 9(11):824–826, 2005. 4

[45] Hikaru Kawauchi, Kazuhiro Yonezawa, Yuichi Kozawa, and Shunichi Sato. Calculation of optical trapping forces on a dielectric sphere in the ray optics regime produced by a radially polarized laser beam. *Optics letters*, 32(13):1839–1841, 2007. 4, 10

[46] Anita Devi and Arijit K De. Alternate analytic formulation of optical force on a dielectric sphere in the ray optics limit. *JOSA B*, 35(2):244–250, 2018. 4

[47] Shuhe Zhang, Meng Shao, Xiao Yang, and Jinhua Zhou. Calculating optical forces with skew line ray model for gaussian beam. *Optik*, 203:163935, 2020. 4

[48] Qiwen Zhan. Cylindrical vector beams: from mathematical concepts to applications. *Advances in Optics and Photonics*, 1(1):1–57, 2009. 4

[49] Andrew Forbes. Structured light from lasers. *Laser & Photonics Reviews*, 13(11):1900140, 2019. 4

[50] E Otte and C Denz. Optical trapping gets structure: structured light for advanced optical manipulation. *Applied Physics Reviews*, 7(4):041308, 2020. 4

[51] Christopher L Kuyper and Daniel T Chiu. Optical trapping: A versatile technique for biomanipulation. *Applied spectroscopy*, 56(11):300A–312A, 2002. 9

[52] Mike Woerdemann. *Structured Light Fields: Applications in Optical Trapping, Manipulation, and Organisation*. Springer Science & Business Media, 2012. 9

[53] Nunzia Malagnino, Giuseppe Pesce, Antonio Sasso, and Ennio Arimondo. Measurements of trapping efficiency and stiffness in optical tweezers. *Optics Communications*, 214(1-6):15–24, 2002. 9

[54] A Ungut, G Grehan, and G Gouesbet. Comparisons between geometrical optics and lorenz-mie theory. *Applied Optics*, 20(17):2911–2918, 1981. 10

[55] Gérard Gouesbet, Bruno Maheu, and Gérard Gréhan. Light scattering from a sphere arbitrarily located in a gaussian beam, using a bromwich formulation. *JOSA A*, 5(9):1427–1443, 1988. 10

[56] Gérard Gouesbet. Generalized lorenz-mie theory and applications. *Particle & particle systems characterization*, 11(1):22–34, 1994. 10

[57] Ruixue Zhu, Tatiana Avsievich, Alexey Popov, and Igor Meglinski. Optical tweezers in studies of red blood cells. *Cells*, 9(3):545, 2020. 10

[58] Karel Svoboda and Steven M Block. Biological applications of optical forces. *Annual review of biophysics and biomolecular structure*, 23(1):247–285, 1994. 10

[59] Yiqiong Zhao, Graham Milne, J Scott Edgar, Gavin DM Jeffries, David McGloin, and Daniel T Chiu. Quantitative force mapping of an optical vortex trap. *Applied physics letters*, 92(16):161111, 2008. 10

[60] Erkin Sidick, Scott D Collins, and Andre Knoesen. Trapping forces in a multiple-beam fiber-optic trap. *Applied optics*, 36(25):6423–6433, 1997. 13

[61] Shojiro Nemoto and Hiroyoshi Togo. Axial force acting on a dielectric sphere in a focused laser beam. *Applied optics*, 37(27):6386–6394, 1998. 13

[62] Max Born and Emil Wolf. *Principles of optics: electromagnetic theory of propagation, interference and diffraction of light*. Elsevier, 2013. 21

[63] Michael J Kidger. Fundamental optical design. SPIE Bellingham, 2001. 23

[64] Karuna Sindhu Malik and Bosanta R Boruah. Calculation of spot diagrams of different vector beams using geometrical ray tracing. In *Complex Light and Optical Forces XIV*, volume 11297, page 1129706. International Society for Optics and Photonics, 2020. 23

[65] Dennis Gabor. Holography, 1948-1971. *Science*, 177(4046):299–313, 1972. 33

[66] Parameswaran Hariharan and P Hariharan. *Optical Holography: Principles, techniques and applications*. Cambridge University Press, 1996. 34

[67] Parameswaran Hariharan. *Basics of holography*. Cambridge university press, 2002. 34

[68] Wai-Hon Lee. Binary computer-generated holograms. *Applied Optics*, 18(21):3661–3669, 1979. 35

[69] Ajoy Ghatak. *Contemporary optics*. Springer Science & Business Media, 2012. 36

[70] BR Boruah. Dynamic manipulation of a laser beam using a liquid crystal spatial light modulator. *American Journal of Physics*, 77(4):331–336, 2009. 37

[71] Mary L Boas. *Mathematical methods in the physical sciences*. John Wiley & Sons, 2006. 37

[72] Mark A A Neil, MJ Booth, and T Wilson. Dynamic wave-front generation for the characterization and testing of optical systems. *Optics letters*, 23(23):1849–1851, 1998. 38

[73] Robert J Noll. Zernike polynomials and atmospheric turbulence. *JOsA*, 66(3):207–211, 1976. 39

[74] Karuna Sindhu Malik, Nagendra Kumar, and Bosanta R. Boruah. Dynamic modulation of spatial intensity profile of a laser beam using a binary hologram. *Optics Communications*, 515:128201, 2022. 39

[75] Vincent Bagnoud and Jonathan D Zuegel. Independent phase and amplitude control of a laser beam by use of a single-phase-only spatial light modulator. *Optics letters*, 29(3):295–297, 2004. 40

[76] Jennifer E Curtis, Brian A Koss, and David G Grier. Dynamic holographic optical tweezers. *Optics communications*, 207(1-6):169–175, 2002. 43

[77] José A Rodrigo, Mercedes Angulo, and Tatiana Alieva. Dynamic morphing of 3d curved laser traps for all-optical manipulation of particles. *Optics express*, 26(14):18608–18620, 2018. 43

[78] José A Rodrigo, Mercedes Angulo, and Tatiana Alieva. All-optical motion control of metal nanoparticles powered by propulsion forces tailored in 3d trajectories. *Photonics Research*, 9(1):1–12, 2021. 43

[79] Glen R Kirkham, Emily Britchford, Thomas Upton, James Ware, Graham M Gibson, Yannick Devaud, Martin Ehrbar, Miles Padgett, Stephanie Allen, Lee D Buttery, et al. Precision assembly of complex cellular microenvironments using holographic optical tweezers. *Scientific reports*, 5(1):1–7, 2015. 43

[80] Miles Padgett and Roberto Di Leonardo. Holographic optical tweezers and their relevance to lab on chip devices. *Lab on a Chip*, 11(7):1196–1205, 2011. 43

[81] Karuna Sindhu Malik, Nagendra Kumar, Akanshu Chauhan, Nedup Sherpa, and Bosanta R Boruah. Asian journal of physics. *Asian Journal of Physics*, 28(10-12):1197–1204, 2019. 43

[82] Stefan W Hell. Far-field optical nanoscopy. *science*, 316(5828):1153–1158, 2007. 55

[83] Keir C Neuman and Steven M Block. Optical trapping. *Review of scientific instruments*, 75(9):2787–2809, 2004. 60

[84] Zan Gong, Zhong Wang, Yinmei Li, Liren Lou, and Shenghua Xu. Axial deviation of an optically trapped particle in trapping force calibration using the drag force method. *Optics communications*, 273(1):37–42, 2007. 61

[85] Jong-Ho Baek, Sun-Uk Hwang, and Yong-Gu Lee. Trap stiffness in optical tweezers. *Mirror*, 685:1100nm, 2007. 61

[86] Cx K Batchelor and GK Batchelor. *An introduction to fluid dynamics*. Cambridge university press, 2000. 61

[87] Harald Felgner, Otto Müller, and Manfred Schliwa. Calibration of light forces in optical tweezers. *Applied optics*, 34(6):977–982, 1995. 62

[88] Ann AM Bui, Alexander B Stilgoe, Nima Khatibzadeh, Timo A Nieminen, Michael W Berns, and Halina Rubinsztein-Dunlop. Escape forces and trajectories in optical tweezers and their effect on calibration. *Optics express*, 23(19):24317–24330, 2015. 62

[89] Karuna Sindhu Malik and Bosanta R Boruah. Optimal trap velocity in a dynamic holographic optical trap using a nematic liquid crystal spatial light modulator. *Journal of Optics*, 24(3):034004, 2022. 64

List of publications and scientific activities

Journals and proceedings

- Karuna Sindhu Malik, Nagendra Kumar, Akanshu Chauhan, Nedup Sherpa and Bosanta R Boruah, “Understanding dynamic beam shaping using liquid crystal spatial light modulator," Asian Journal of Physics, Vol.28 Nos 10-12, 2019, 1197-1204
- Karuna Sindhu Malik, S. S. Goutam Buddha, Ranjan Kalita and Bosanta R. Boruah, “ Estimation of maximum translation speed of a trapped particle in holographic optical tweezers ", Proc. SPIE, 11297, 112970Z (2020)
- Karuna Sindhu Malik and Bosanta R. Boruah, “ Calculation of spot diagrams of different vector beams using geometrical ray tracing ", Proc. SPIE, 11297, 1129706 (2020)
- Karuna Sindhu Malik and Bosanta R. Boruah, "Optimal trap velocity in a dynamic holographic optical trap using a nematic liquid crystal spatial light modulator ", Journal of Optics (IOP) : 24 (3), 034004 (2022)
- Karuna Sindhu Malik, Nagendra Kumar and Bosanta R. Boruah, "Dynamic modulation of spatial intensity profile of a laser beam using a binary hologram ", Optics Communications: 515, 128201 (2022)
- Karuna Sindhu Malik and Bosanta R. Boruah, “Optical force calculation in the ray-optics regime for beam with arbitrary complex amplitude profiles", (Under review)

Conference Presentations

- Karuna Sindhu MaliK and Bosanta R. Boruah, "Force calculation models for optical trapping", International conference on Advances in optics and photonics (ICAOP), November 2017.

- Karuna Sindhu MaliK and Bosanta R. Boruah, "Different types of Gaussian beams and their point spread functions", Research conclave IITG, March 2018.
- Karuna Sindhu MaliK and Bosanta R. Boruah, "Generation of Hermite-Gaussian and Laguerre-Gaussian beam using Computer Generated Holographic technique", NaSAEAST-2018 conducted on 5-6 October 2018 at Gauhati University.
- Karuna Sindhu MaliK and Bosanta R. Boruah, "Estimation of trapping force for different amplitude profile of the trapping beam", Photonics 2018 organized by IIT Delhi on December 12-15,2018.
- Karuna Sindhu MaliK and Bosanta R. Boruah, "Computation of Spot Diagrams for Vector Beams", Photonics 2018 organized by IIT Delhi on December 12-15, 2018.
- Karuna Sindhu Malik, S. S. Goutam Buddha, Ranjan Kalita and Bosanta R. Boruah, " Estimation of maximum translation speed of a trapped particle in holographic optical tweezers ", Proc. SPIE, 11297, 112970Z (2020)
- Karuna Sindhu Malik and Bosanta R. Boruah, " Calculation of spot diagrams of different vector beams using geometrical ray tracing ", Proc. SPIE, 11297, 1129706 (2020)

Conference/ School/ Workshop attended

- Participated in National Seminar on Advances in Electronics and Allied Science and Technology (NaSAEAST-2017)" held on 27th and 28th June 2017, organized by Electronic Scientists and Engineers Society (ESES) and Gauhati University, Guwahati, Assam.
- Presented research work in the Annual Physics Meet held on 28^{th} January, 2017 organized by the Research Scholar Forum of the Department of Physics, IIT Guwahati.
- Attended the "Simulation in Physics" workshop held on 27^{th} - 28^{th} of January, 2017 organized by the Research Scholars' Forum of the Dept. of Physics, IIT Guwahati.
- Participated in Research Conclave-2017, held on 16th-19th March 2017, organized by Student Affairs Board (SAB), IITG.
- Participated in "One Day Workshop on Vacuum Technology and Its application In Optical Science", held on 19th August 2017, organized by SPIE IIT Guwahati Student Chapter and Pfeier Vacuum Pvt. Ltd., in association with Department of Physics, IITG.

- Participated in Latex Workshop, held on September 9, 2017 organized by Research Scholar Forum, EEE IIT Guwahati.
- Participated in IEEE Workshop on Advanced MATLAB Applications to Robotics and Signal Processing (RASPMAT 2017)" held on 7^{th} and 8^{th} October 2017, organized by IEEE Student Branch, Indian Institute of Technology Guwahati.
- Participated in “Optics: Not an illusion- a Students’ Symposium organized by SPIE IIT Guwahati Student Chapter, held on 28^{th} October, 2017 at Nowgong College.
- Participated as a volunteer in the SERB School on the topic “Frontiers in Quantum Optics" organized by the Dept. of Physics, IIT Guwahati during 01-19 December, 2017.
- Participated in Patent writing workshop at Research conclave’18 organized by SAB, IITG.
- Participated in MATLAB Workshop at Research Conclave’18 organized by SAB, IIT Guwahati.
- Attended and completed the tutorial on "Introduction to Optical Microscopy: From basics to super-resolution” conducted on 19th September 2018 during the OSI-International Symposium on Optics at IIT Kanpur.

* * * * * *